

AWARD NUMBER: W81XWH-12-1-0328

TITLE: Hyperpolarized <sup>13</sup>C MR Markers of Renal Tumor Aggressiveness

PRINCIPAL INVESTIGATOR: Dr. Renuka Sriram

CONTRACTING ORGANIZATION: University of California, San Francisco  
San Francisco, CA 94103

REPORT DATE: December 2015

TYPE OF REPORT: Final

PREPARED FOR: U.S. Army Medical Research and Materiel Command  
Fort Detrick, Maryland 21702-5012

DISTRIBUTION STATEMENT: Approved for Public Release;  
Distribution Unlimited

The views, opinions and/or findings contained in this report are those of the author(s) and should not be construed as an official Department of the Army position, policy or decision unless so designated by other documentation.

REPORT DOCUMENTATION PAGE				Form Approved OMB No. 0704-0188	
Public reporting burden for this collection of information is estimated to average 1 hour per response, including the time for reviewing instructions, searching existing data sources, gathering and maintaining the data needed, and completing and reviewing this collection of information. Send comments regarding this burden estimate or any other aspect of this collection of information, including suggestions for reducing this burden to Department of Defense, Washington Headquarters Services, Directorate for Information Operations and Reports (0704-0188), 1215 Jefferson Davis Highway, Suite 1204, Arlington, VA 22202-4302. Respondents should be aware that notwithstanding any other provision of law, no person shall be subject to any penalty for failing to comply with a collection of information if it does not display a currently valid OMB control number. <b>PLEASE DO NOT RETURN YOUR FORM TO THE ABOVE ADDRESS.</b>					
1. REPORT DATE December 2015		2. REPORT TYPE Final		3. DATES COVERED 15 Sep 2012 - 14 Sep 2015	
4. TITLE AND SUBTITLE  Hyperpolarized <sup>13</sup> C MR Markers of Renal Tumor Aggressiveness				5a. CONTRACT NUMBER	
				5b. GRANT NUMBER W81XWH-12-1-0328	
				5c. PROGRAM ELEMENT NUMBER	
6. AUTHOR(S) Renuka Sriram  E-Mail: Renuka.Sriram@ucsf.edu				5d. PROJECT NUMBER	
				5e. TASK NUMBER	
				5f. WORK UNIT NUMBER	
7. PERFORMING ORGANIZATION NAME(S) AND ADDRESS(ES)  University of California, San Francisco, San Francisco, CA 94103				8. PERFORMING ORGANIZATION REPORT NUMBER	
9. SPONSORING / MONITORING AGENCY NAME(S) AND ADDRESS(ES)  U.S. Army Medical Research and Materiel Command Fort Detrick, Maryland 21702-5012				10. SPONSOR/MONITOR'S ACRONYM(S)	
				11. SPONSOR/MONITOR'S REPORT NUMBER(S)	
12. DISTRIBUTION / AVAILABILITY STATEMENT  Approved for Public Release; Distribution Unlimited					
13. SUPPLEMENTARY NOTES					
14. ABSTRACT RCCs have a wide range of aggressiveness, which is currently difficult to assess noninvasively. There is an unmet clinical need to reliably distinguish RCC from benign renal tumors for optimal triage of therapies. Hyperpolarized (HP) <sup>13</sup> C magnetic resonance (MR) is a new metabolic imaging approach that is capable of interrogating specific enzymatic pathways in real time. Our aim was to interrogate tumor metabolism in more clinically relevant RCC tumor models by employing patient-derived tumor tissues in conjunction with HP MR. We have shown that in addition to increased lactate production, the clear cell subtype of RCC (which makes for the majority of RCCs) has a distinct feature of increased lactate efflux which can be used to discern it from benign renal tumors in the ex vivo bioreactor set-up. Additionally we have shown that while patient derived renal tissue slices used in orthotopic mouse model can be established successfully, it is not feasible to conduct hyperpolarized MR experiments due to the limited tumor growth of only the high grade aggressive tumor tissues. Nonetheless in the process, we have used human immortalized RCC cells in the orthotopic mouse model and developed pulse sequences to interrogate increased lactate production as well as efflux using HP <sup>13</sup> C MR.					
15. SUBJECT TERMS Renal Cell Carcinoma, Hyperpolarized <sup>13</sup> C MR, Sub-renal capsule, patient derived tissue slice cultures, bioreactor					
16. SECURITY CLASSIFICATION OF:			17. LIMITATION OF ABSTRACT  Unclassified	18. NUMBER OF PAGES	19a. NAME OF RESPONSIBLE PERSON USAMRMC
a. REPORT  Unclassified	b. ABSTRACT  Unclassified	c. THIS PAGE  Unclassified			19b. TELEPHONE NUMBER (include area code)

## Table of Contents

	<u>Page</u>
<b>1. Introduction.....</b>	<b>1</b>
<b>2. Keywords.....</b>	<b>1</b>
<b>3. Key Research Accomplishments.....</b>	<b>1</b>
<b>4. Reportable Outcomes.....</b>	<b>10</b>
<b>5. Conclusion.....</b>	<b>12</b>
<b>6. References.....</b>	<b>12</b>
<b>7. Appendices.....</b>	<b>13</b>

## 1. INTRODUCTION:

The incidence of renal cell carcinomas (RCCs) has been steadily increasing, in part due to widespread use of cross-sectional imaging[1]. RCCs have a wide range of aggressiveness, which is currently difficult to assess noninvasively. This has resulted in overtreatment of indolent cancers, and possibly under-treatment of aggressive ones. Additionally, current imaging techniques cannot distinguish benign renal tumors from RCCs, resulting in unnecessary surgical resection of benign renal tumors. Therefore, there is an unmet clinical need to be able to reliably distinguish renal tumor aggressiveness for optimal triage of therapies. Hyperpolarized (HP)  $^{13}\text{C}$  magnetic resonance spectroscopic imaging (MRSI) is a new metabolic imaging approach that is capable of interrogating specific enzymatic pathways in real time. In this proposal, we aim to interrogate tumor metabolism in a clinically relevant renal tumor models by employing patient-derived tumor tissues in conjunction with HP MRSI. The patient-derived tumor models, including tissue slices maintained in a bioreactor and implanted orthotopically in mice, can better recapitulate the heterogeneous range of renal tumors (including benign renal tumors and RCCs), and facilitate identification of clinically relevant markers of tumor aggressiveness. Specifically,

**Aim 1: Identify HP  $^{13}\text{C}$  metabolic markers that discriminate benign renal tumors from RCCs, and low grade from high grade RCCs using human TSCs cultured in a bioreactor.**

**Aim 2: Identify HP  $^{13}\text{C}$  metabolic markers that discriminate *low* grade from high grade RCCs using human tumor tissues implanted under renal capsule of mice.**

There has been no change in the tasks specified in Aims 1 and 2 from those proposed in the original Statement of Work, and below I describe the research that has been accomplished for each aim.

## 2. KEY WORDS:

Renal Cell Carcinoma, Hyperpolarized  $^{13}\text{C}$  MR, Sub-renal capsule, patient derived tissue slice cultures, bioreactor

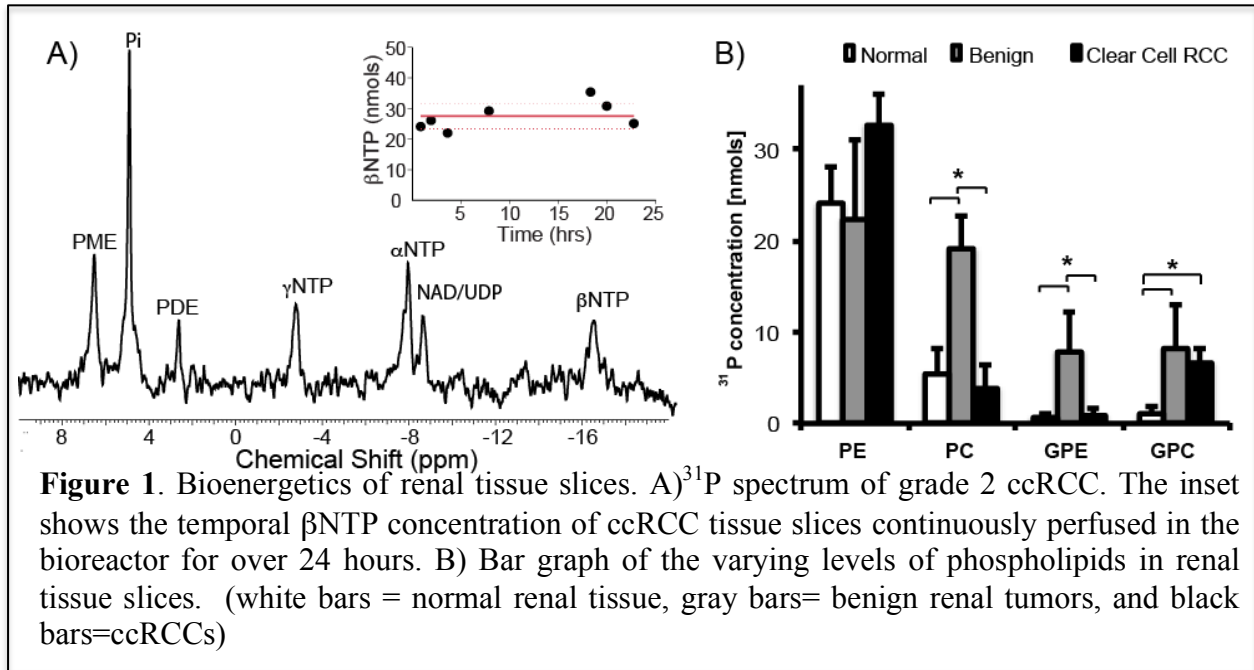
## 3. KEY RESEARCH ACCOMPLISHMENTS:

**Development of patient-derived renal tumor tissue slice cultures (TSC):** In collaboration with Dr. Peehl, we successfully implemented a protocol to acquire renal tumor tissues from nephrectomies and to culture the tissue slices as detailed in the first annual report (2013).

### **Aim 1: Ex vivo bioreactor experiments**

Summary: The key finding from the bioreactor experiments using patient-derived renal tumor tissues is that clear cell RCCs (the most common and usually more aggressive type of RCCs) have rapid lactate efflux into extracellular space when compared to benign renal tumors and normal renal tissues. Because extracellular lactate and acidic extracellular pH are implicated in tumor aggressiveness and metastatic potential, our findings suggest that lactate efflux, measured with hyperpolarized MR in conjunction with diffusion weighting currently being developed to quantify the relative amount of extracellular lactate, can serve as a potential biomarker to stratify renal tumor aggressiveness.

### ***Bioenergetics and viability of renal tissue slices in the 3D MR compatible bioreactor:***



Patient-derived renal slices were obtained from 10 ccRCC (predominantly of Furhman grade 2, with one case each for grade 1 and 3), 3 benign renal tumors (2 oncocytomas and one angiomyolipoma), and 12 normal renal parenchyma tissues not involved by tumors. These fresh tissue slices were studied in a 3D tissue bioreactor.

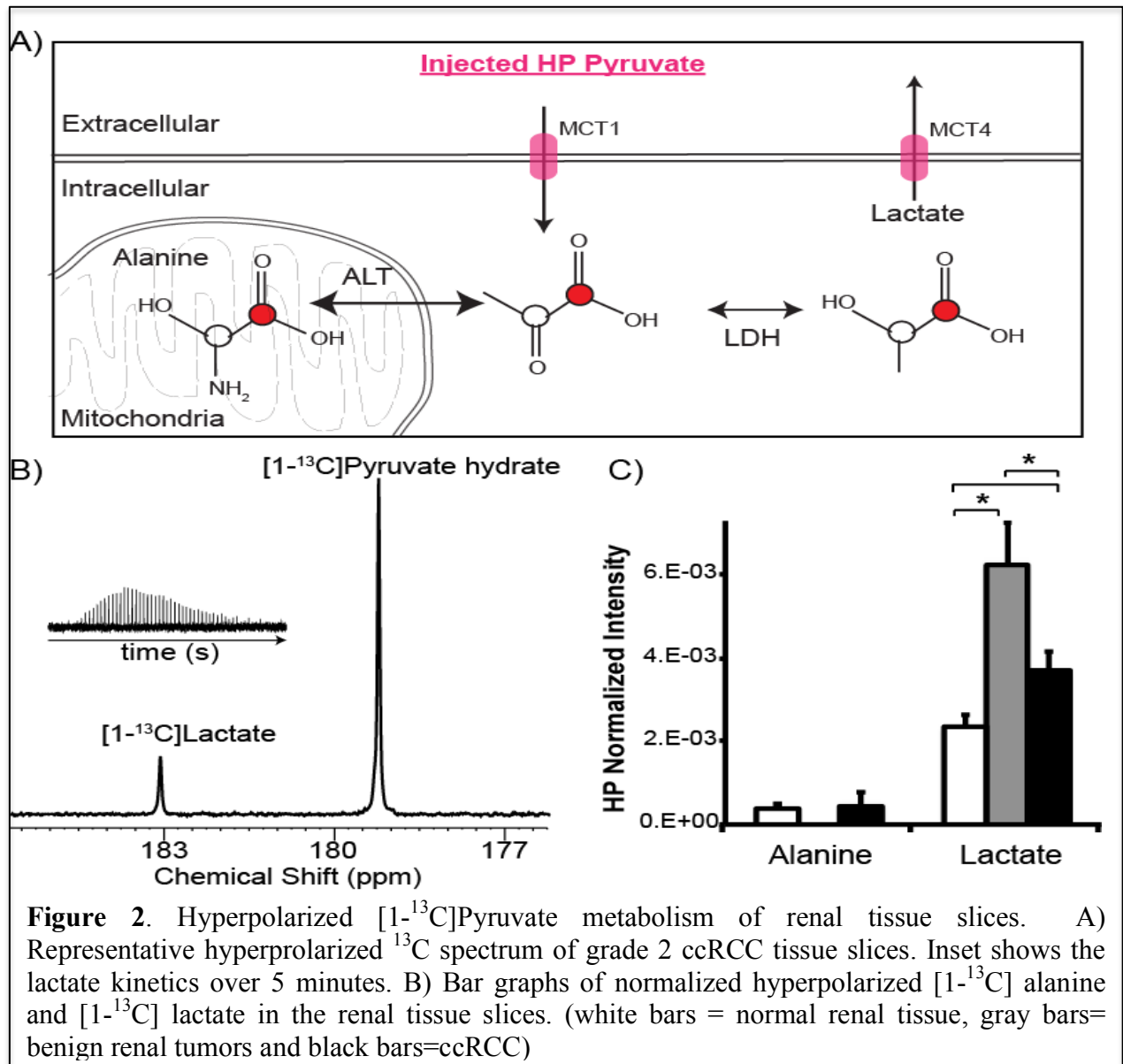
The micro-engineered 3D 5mm tube MR compatible bioreactor has been shown previously to allow maintenance of tissue viability and to provide reproducible HP MR data [2]. In this study, it allowed the metabolic evaluation of 60-90 mg of renal tissue and had excellent  $B_0$  field homogeneity (average water line width at half maximum was  $12.2 \pm 0.68$  Hz).  $^{31}\text{P}$  MR spectroscopy was employed to monitor changes in renal tissue bioenergetics during the bioreactor studies. Figure 1A shows a representative spectrum of a clear cell RCC (ccRCC). NMR signals for the nucleoside triphosphates (NTPs:  $\gamma\text{NTP}$ ,  $\alpha\text{NTP}$ , and  $\beta\text{NTP}$ ), phosphocholine (PC), inorganic phosphate ( $\text{P}_i$ ), and glycerol phosphocholine (GPC) were readily visible. The  $\beta\text{NTP}$  content was unchanged following the injection of HP  $^{13}\text{C}$  pyruvate, indicating maintenance of tissue bioenergetics and viability during the course of hyperpolarized experiments. Furthermore, we showed that tissue viability was maintained in the bioreactor with near constant  $\beta\text{NTP}$  for over 24 hours (inset of figure 1A).

Figure 1B shows the varying levels of phospholipids in the renal tissue slices. Interestingly the phosphocholine (PC) level in the benign renal tumors is significantly higher than both the normal renal parenchyma ( $p=0.019$ ) and ccRCC ( $p=0.008$ ) tissues. This finding is similar to that of prior  $^1\text{H}$  high-resolution study of renal tissue extracts [3], and indicates that while PC has been used as a biomarker of tumor proliferation and aggressiveness in other types of cancer [4], it has limited value for renal tumor characterization. PC is converted from choline by the enzyme choline kinase- $\alpha$  (CHKA) in the phosphatidylcholine synthesis (kennedy) pathway. A prior study reported that functional interaction between CHK- $\alpha$ , EGFR receptor and c-Src is required for

cell proliferation. Such functional interaction may explain the lack of direct correlation between PC level and renal tumor aggressiveness in our study. The glycerophosphocholine (GPC) is significantly higher in both benign renal tumors and ccRCCs compared to normal renal parenchyma tissue ( $p=0.027$  and  $0.003$  respectively). While GPC is an osmolyte in the renal medulla, it is also involved in cell membrane synthesis and breakdown. The higher level in both the benign renal tumors and the ccRCCs compared to normal renal parenchyma may be ascribed to tumor cell proliferation.

### ***Hyperpolarized $^{13}\text{C}$ pyruvate metabolism of renal tissue slices in the 3D MR compatible bioreactor:***

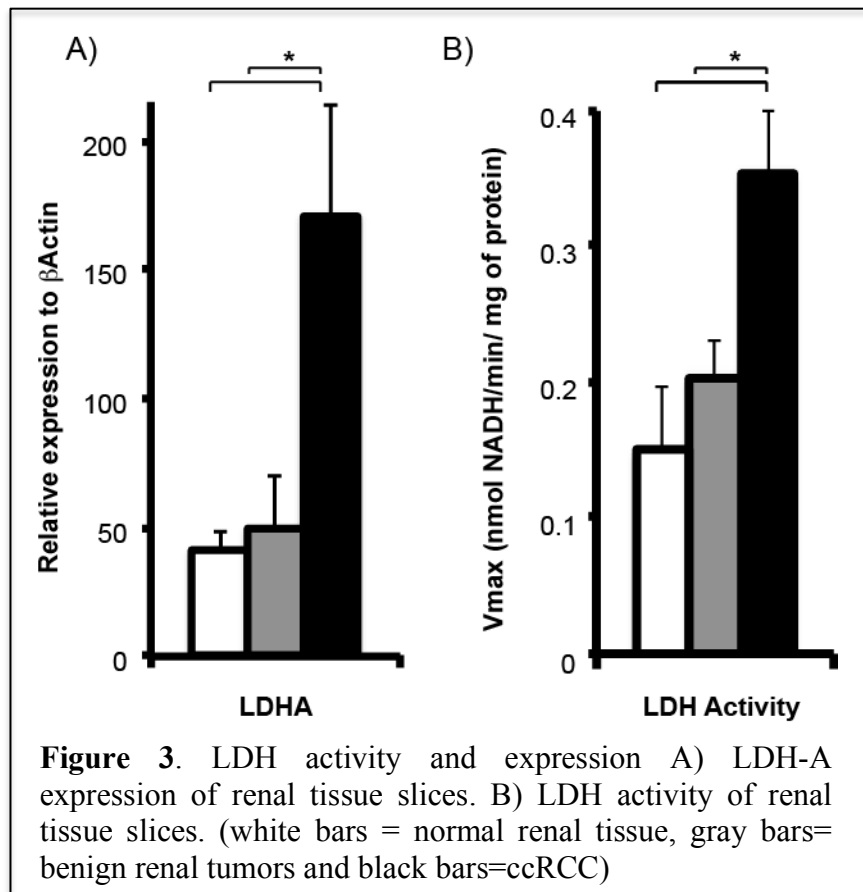
Figure 2A illustrates the scheme of  $^{13}\text{C}$  labeled carbon atom transitions used to detect  $[1-^{13}\text{C}]$  pyruvate metabolism during the HP MR experiment. After injection of hyperpolarized  $[1-^{13}\text{C}]$ pyruvate into the bioreactor, the pyruvate to lactate conversion in the renal tissue slices was assessed in real time. The  $^{13}\text{C}$  lactate spectrum had excellent SNR of  $15 \pm 2$  (**figure 2B**). Both

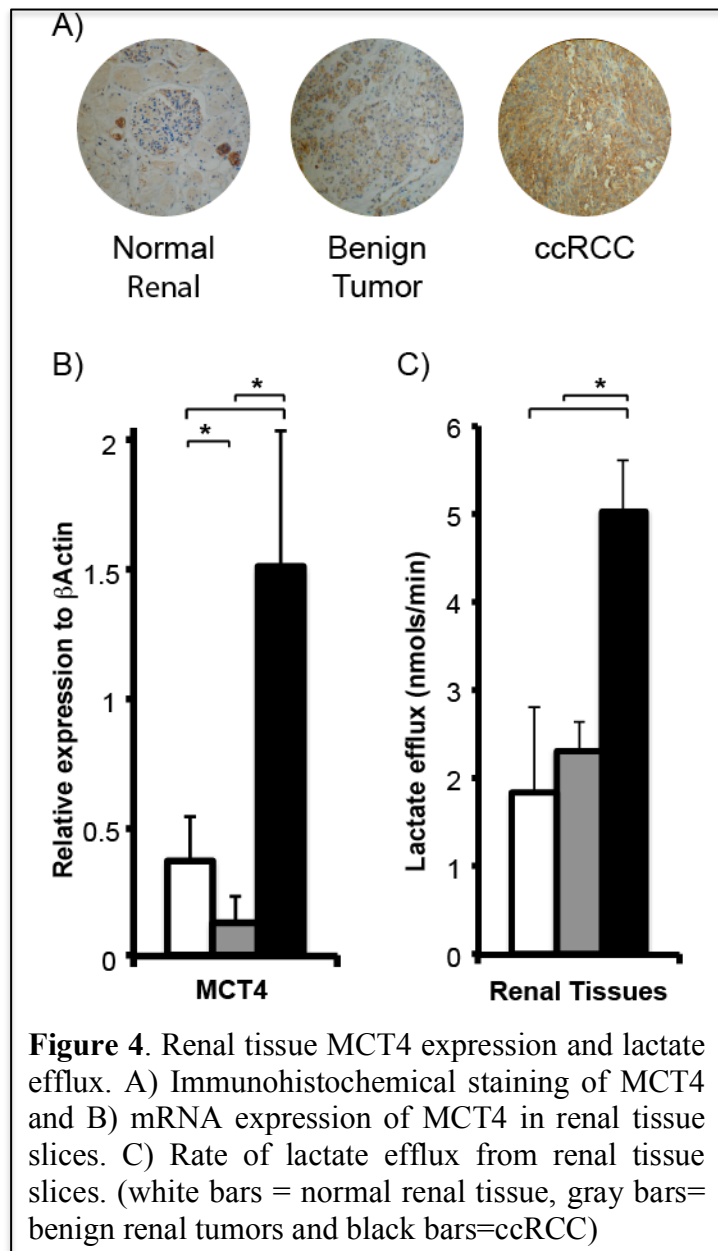


the benign renal tumors and ccRCCs showed higher pyruvate to lactate conversion, consistent with higher glycolysis, when compared to normal renal parenchymal tissues (both p-values < 0.05). However, the observed pyruvate to lactate conversion was lower in ccRCCs than benign renal tumors. Prior studies of RCC cells in a similar continuous perfusion system showed that rapidly exported  $^{13}\text{C}$  lactate quickly flows out of the MR sensitive volume without contributing to the measured hyperpolarized lactate signal (27). Therefore, we hypothesize that the apparent lower pyruvate to lactate conversion in ccRCC when compared to benign renal tumors may be a result of rapid lactate efflux in ccRCCs.

Hyperpolarized alanine was detectable only in the normal renal tissues with a SNR of at least 3. Alanine was not detectable in the benign renal tumor tissues, and it was occasionally observed (in 1/3 of the cases) at low levels in the ccRCC tissues. The low alanine level in the tumor tissues may be a result of the increased pyruvate to lactate conversion.

**Tissue analysis confirms that ccRCCs have higher lactate production and efflux than benign renal tumors:**





To test the hypothesis that ccRCCs have higher lactate production and efflux than benign renal tumors, we then assayed the mRNA expressions and enzyme activity of LDH, and the mRNA expression of MCT1 and MCT4 of the tissue slices. LDHA encodes the M subunits of LDH, which catalyzes the conversion between pyruvate and lactate. MCT1 mediates the pyruvate transport into the cells, and MCT4 mediates the efflux of the lactate out of the cells (ref). The LDH-A mRNA expression was significantly higher in ccRCCs compared to both normal renal tissues and benign tumors ( $p=0.001$  and  $p=0.016$  respectively) (**figure.3A**). Additionally the LDH activity was also significantly higher ( $p<0.05$ ) in ccRCC compared to the normal renal tissues and benign tumors by 2.4 and 1.7 times respectively (**figure.3B**). The MCT4 mRNA expression in the ccRCCs was four-fold higher ( $p=0.021$ ) than that normal renal tissues and almost 7 fold higher than that of benign tumors ( $p=0.045$ ). Corresponding immunohistochemical staining also showed progressively increased MCT4 staining from normal renal tissues to ccRCCs. To further verify that the higher MCT4 expression in ccRCCs resulted in

increased lactate efflux, we quantified

the rate of lactate efflux in the tissue slices in culture by thermal labeling with  $[3-^{13}\text{C}]$ pyruvate. The incubating media was sampled periodically for up to 8 hours and the  $[3-^{13}\text{C}]$ lactate was measured using high-resolution MR spectroscopy. The normal renal tissues and benign tumors had similar levels of lactate efflux rate, while ccRCCs had significantly higher efflux rate of  $5 \pm 0.57$  nmols/min ( $p=0.01$  and  $0.002$  respectively). Taken together, these observations support the notion that ccRCCs have the highest lactate production and efflux compared to benign renal tumors and normal renal tissues. The rapid lactate efflux likely accounted for the apparent lower HP lactate in ccRCCs than benign renal tumors



## **Aim 2: Orthotopic model of RCC using patient-derived tumor tissue slices**

**Summary:** We showed feasibility of establishing orthotopic model of RCC using patient-derived tumor tissue slices. However, since only the aggressive tumor tissues (i.e. Fuhrman grade 4 RCC) grew into tumors with size sufficient for in vivo imaging, we were unable to compare the metabolic differences between benign / indolent tumors and aggressive tumors.. In parallel, we investigated several imaging approaches to measure dynamic exchange and metabolism of hyperpolarized pyruvate to lactate that would be important for future in vivo imaging in the clinic. Specifically, based on the observations of increased lactate efflux in the ccRCC in the bioreactor, we developed diffusion weighted hyperpolarized  $^{13}\text{C}$  pulse sequences in order to interrogate the differential compartmentation of lactate. Such sequences were tested on an *in vivo* orthotopic animal model of immortalized human RCC cells (generated with other funding) of varying aggressiveness. This will demonstrate the clinical feasibility of such measures in order to distinguish between benign and RCC tumors in patients using the non-invasive rapid hyperpolarized  $^{13}\text{C}$  MRI.

### **Review of patient derived renal tissue slice orthotopic mouse model:**

We showed feasibility of engrafting human renal tumor tissues under the renal capsule of the Rag2-IL2g male mice in collaboration with Dr. Peehl at Stanford [5]. Figure 5 demonstrated the preserved human vasculature in one such tumor tissue graft in the mouse renal capsule. However, Only the Fuhrman grade 4 ccRCC developed tumors of sufficient size for in vivo HP imaging, and limited our ability to study the metabolic difference among tumors of different aggressiveness using this model.

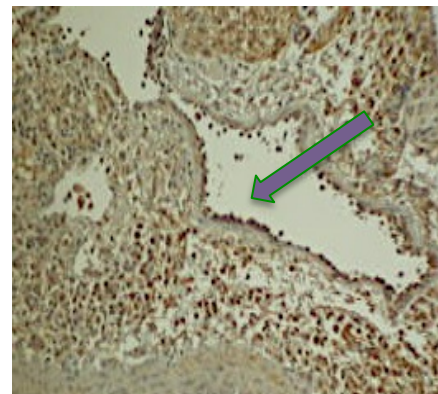


**Figure 5:** CD31 staining of the graft (arrow) indicates the preserved human vasculature.

Nevertheless, we developed an orthotopic murine model with a panel of immortalized RCC cells. We selected the cells based on their varied LDHA and MCT4 expression, two key factors in lactate production and export which are implicated in RCC aggressiveness. Preliminary data has been generated using the following cells- UOK262 (isolated from a metastatic lesion of papillary RCC), UMRC3 (derived from a primary ccRCC with metastatic lesions) and 786-O (primary ccRCC).

### **Development of dynamic hyperpolarized $^{13}\text{C}$ MRI sequences to measure increased lactate production as well as lactate efflux in tumor models established using RCC cells :**

a) *Enhanced contrast between normal mouse kidney and tumor:* We optimized the  $^{13}\text{C}$  dynamic imaging sequence using a spectrally and spatially selective pulse [6]-[8] to obtain simultaneously the lactate and pyruvate images over 45 seconds to minimize the background lactate signal from the normal kidney cells which filters the lactate (originating from the rest of the body) from the blood. Initial hyperpolarized imaging showed increased lactate signal in the normal contralateral kidney similar to that found in the tumor bearing kidney. This is due to the normal renal function of collecting the recirculating lactate generated from the rest of the body. Figure 6 shows the

feasibility of such imaging with a specialized acquisition scheme using variable flip schedule [9] to maximize signal to noise ratio in vivo in an orthotopic mice model containing human RCC cells. Furthermore preliminary assessment shows a good correlation between the measured HP lactate to pyruvate ratio and the LDH activity of the RCC cells. This indicates that the HP lactate/Pyruvate ratio can be used as a marker of RCC aggressiveness.

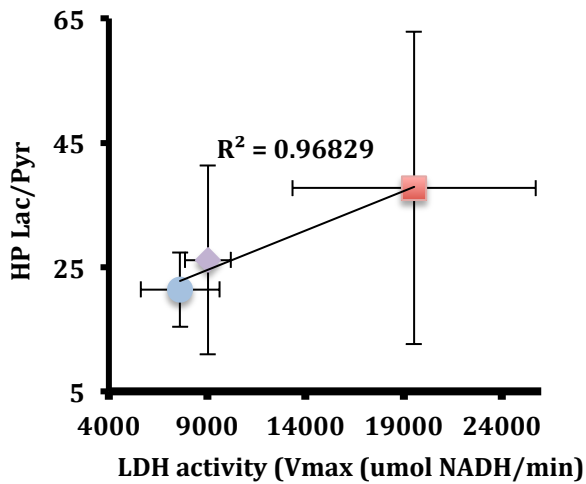
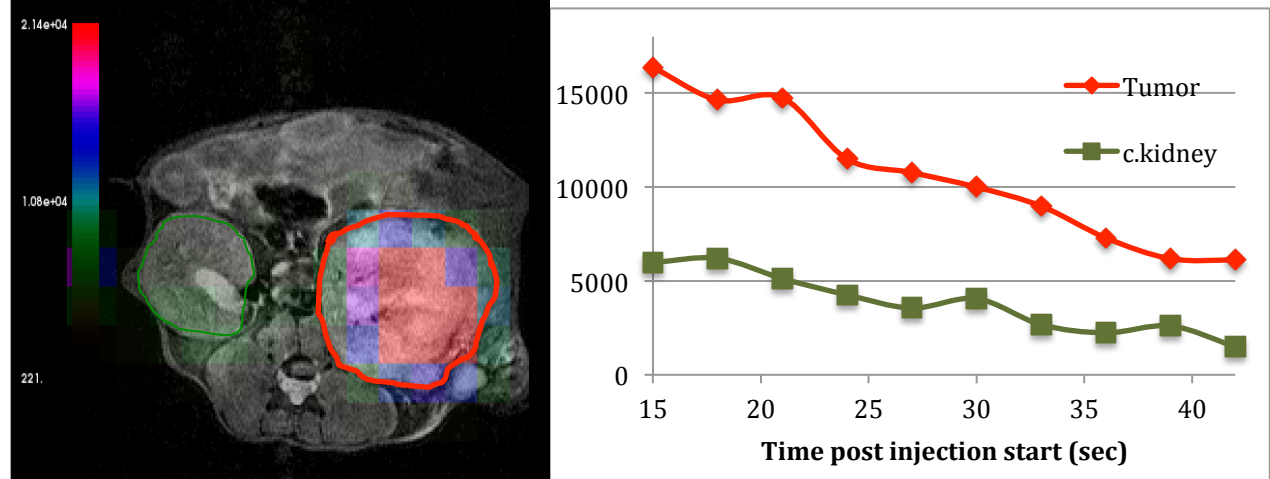


**Figure 6:** Hyperpolarized Lactate images overlaid on T2 weighted proton reference image. The images is an axial slice of a T2 weighted proton image of the mouse implanted with UOK62 cells in the renal capsule, with the red region outlining the tumor tissue and the green denoting the contralateral naïve kidney (c.kidney). The graph above shows that the temporal dynamics of hyperpolarized lactate signal that is produced after infusion of hyperpolarized pyruvate is higher in the tumor compared to the contralateral normal kidney. And preliminary data shows that the HP lactate /Pyruvate ratio correlates with LDH activity in the RCC cell orthotopic murine model.

*b) Simultaneous measurement of bi-directional exchange between pyruvate and lactate:* In collaboration with our colleagues at UCSF Christine et al [10] (manuscript attached in appendix), we implemented a technique to measure dynamically the rate of transfer of hyperpolarized pyruvate into other metabolites in a bi-directional manner. In short, such measurements were made to quantify the rate of conversion of pyruvate to lactate ( $k_{pl}$ ) and lactate to pyruvate ( $k_{lp}$ ) in an *ex vivo* set-up using the bioreactor in UOK262, an aggressive RCC cell. This same cell line was used in an orthotopic murine model and feasibility of  $k_{pl}$  and  $k_{lp}$  measurements were shown. This would be an important biomarker to differentiate between normal renal tissue and RCC which has a known elevated LDHA [11] resulting in higher  $k_{pl}$ .

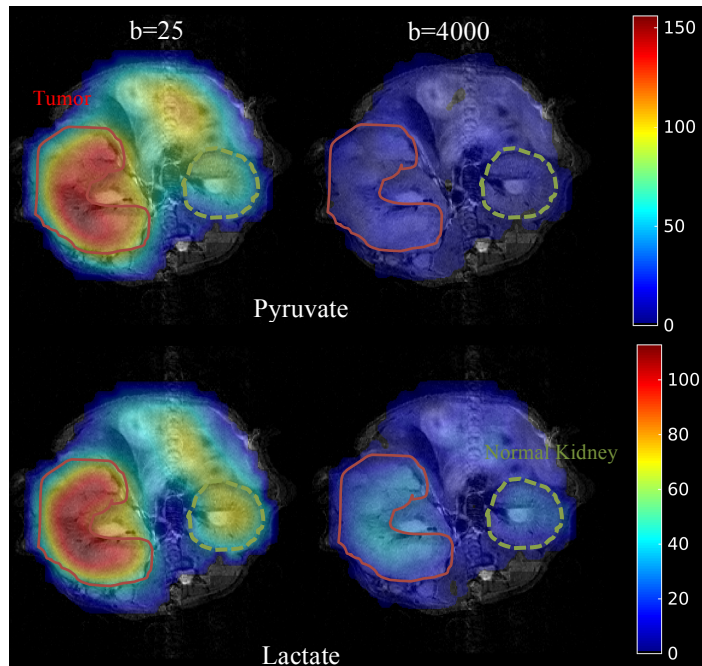


Figure 7. Diffusion weighted HP pyruvate (top row) and lactate (bottom row) images of a orthotopic UOK262 tumor. Left column:  $b=25$   $\text{s/mm}^2$ ; right column:  $b=4000$   $\text{s/mm}^2$  (right column). Red ROI denotes tumor and the green dashed line denotes the normal contralateral mouse kidney. Comparison of the change in HP lactate signal between low and high  $b$ -value images suggests a large extracellular lactate component in the tumor. The *in vivo* Lactate ADC of the tumor is  $0.7 \times 10^{-3} \text{ mm}^2/\text{s}$ .

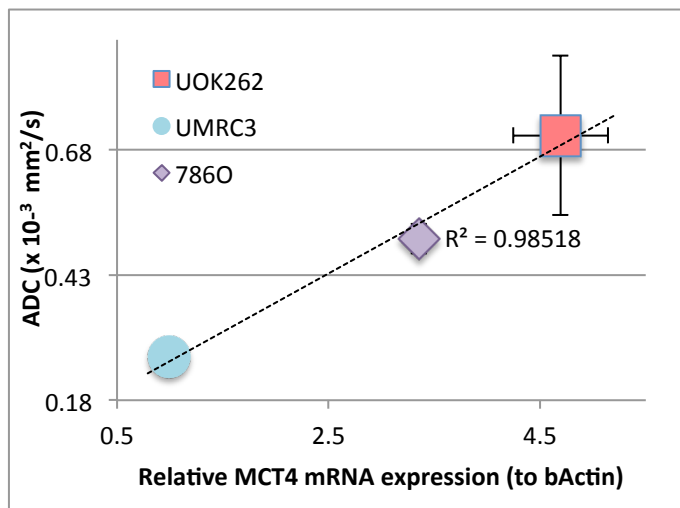


Figure 8: Preliminary data correlating MCT4 expression to hyperpolarized lactate ADC in murine orthotopic model of RCC cells.

*d) Diffusion weighted hyperpolarized  $^{13}\text{C}$  MRI to assess lactate efflux:* While the direct measurement of pyruvate and lactate signals informs on the apparent reaction rate of pyruvate-to-lactate, it does not distinguish between metabolism and transport. In particular, this approach cannot distinguish the intra- and extracellular pool of lactate to quantify transport, which is a key marker of ccRCC based on our findings from Aim I and that also correlates with disease aggressiveness in RCCs [12], [13]. We have previously shown in an *ex vivo* bioreactor system that rapid HP  $^{13}\text{C}$  lactate export is a characteristic feature of aggressive and metastatic RCC cells [14], and preliminary bioreactor data indicates a 5-fold difference between the intra- and extracellular lactate apparent diffusion coefficients (ADC) ( $0.19 \pm 0.03$  vs.  $1.04 \pm 0.08 \times 10^{-3} \text{ mm}^2/\text{s}$ ) [15] (manuscript in preparation, attached in appendix). However, the techniques used in the *ex vivo* study is not suitable for *in vivo* imaging. Indeed, no prior *in vivo* methods exist that can inform on cellular transport processes. Diffusion-

weighted (DW) MRI is sensitive to the motion of molecules, and can detect changes reflective of the tissue microenvironment [16]. Measuring the ADC of metabolites with DW MRI would provide valuable additional information about tissue metabolism and cellular transport because it could directly report on the metabolite microenvironment. We have recently developed an *in vivo* imaging sequence to rapidly generate diffusion-weighted images of HP  $^{13}\text{C}$  metabolites, which can provide localization of the molecules in the tissue microenvironment based on the ADC. Preliminary data from orthotopic model of RCC cells shows a

distinct correlation between the ADC of hyperpolarized lactate measured with that of MCT4 expression (figure 8).

### **FUTURE DIRECTIONS**

- a) We will further evaluate the *in vivo* HP pyruvate to lactate flux and lactate efflux using DW HP MRI in orthotopic tumors derived from RCC cells with different LDH and MCT4 expression.
- b) Apply the above techniques to the evaluation of treatment effect in these RCC models.

### **KEY RESEARCH ACCOMPLISHMENTS:**

- Validation of lactate efflux as a characteristic feature of ccRCC using patient-derived tumor tissues and demonstrates its absence in benign renal tumors and normal renal tissue
- Demonstration that hyperpolarized carbon-13 magnetic resonance technique could potentially serve to differentiate between benign tumors and RCCs based on lactate efflux.
- Develop alternate (to patient derived tissue *in vivo* model) animal models and show feasibility to do hyperpolarized imaging measurements.
- Development of high resolution fast carbon-13 imaging sequences to facilitate measurement of real time metabolism in orthotopically implanted RCC cells. Illustration of HP lactate signal as a biomarker of increased LDH activity in RCC cells *in vivo* using the fast dynamic sequences.
- Implement DW HP MR sequences and show proof of concept that hyperpolarized lactate measures correlates with MCT4 (transporter of lactate) expression in RCC cells.

### **Training and Development:**

As the principle recipient of the fellowship, I benefitted from direct training with world leaders in the field of hyperpolarized carbon-13 magnetic resonance imaging. Additionally in working directly with my mentor Dr. Wang, I gained critical knowledge on the clinical intricacies of both the disease and the imaging technology. This has enabled me to be at the forefront of this burgeoning field and push this technology even further to better serve the medical community. Professional development has also been possible due to this fellowship by attending conferences and workshops to disseminate the research. Furthermore, by attending courses for “scientific writing” has empowered me to better articulate the scientific findings. Overall, I believe that the training and professional development afforded to me via this fellowship has paved the way for me to obtain a professional researcher position at UCSF which will serve as a stepping stone to for a faculty rank.

### **REPORTABLE OUTCOMES :**

#### **I. MANUSCRIPTS (attached in appendices)**

1. Keshari KR, Sriram R, Koelsch BL, Van Criekinge M, Wilson DM, Kurhanewicz J, Wang ZJ. Hyperpolarized 13C-pyruvate magnetic resonance

- reveals rapid lactate export in metastatic renal cell carcinomas. *Cancer Research* 2013;73:529–538.
2. Sriram R, Kurhanewicz J, Vigneron DB. Hyperpolarized Carbon-13 MRI and MRS Studies. *eMagRes* 2014;3:311–324.
  3. Leon Swisher C, Koelsch B, Sukumar S, Sriram R, Santos RD, Wang ZJ, Kurhanewicz J, Vigneron D, Larson P. Dynamic UltraFast 2D EXchange Spectroscopy (UF-EXSY) of hyperpolarized substrates. *J Magn Reson* 2015;257:102–109.
  4. Sriram R, Van Criekinge M, Hansen A, Wang ZJ, Vigneron DB, Wilson DM, Keshari KR, Kurhanewicz J. Real-time measurement of hyperpolarized lactate production and efflux as a biomarker of tumor aggressiveness in an MR compatible 3D cell culture bioreactor. *NMR Biomed* 2015;28:1141–1149.
  5. Using patient-derived renal tumor tissues, we show that increased lactate efflux is a characteristic feature that can be used to differentiate benign tumors from RCCs. The manuscript titled “**Noninvasive differentiation of benign renal tumors from renal cell carcinomas using clinically translatable hyperpolarized <sup>13</sup>C pyruvate magnetic resonance**” is in preparation and is attached in Appendix.

## II. ABSTRACTS AND PRESENTATIONS

1. Oral Presentation: Renuka Sriram, Kayvan R Keshari, Mark Van Criekinge, John Kurhanewicz, David M Wilson, Donna M Peehl, and Zhen J Wang. “**Establishment of patient-derived models of renal cell carcinoma to study metabolism and develop relevant clinical biomarkers**” presented at International Society of Magnetic Resonance in Medicine annual meeting 2013, Salt Lake City, USA
2. Poster Presentation: Renuka Sriram, Kayvan R Keshari, Mark Van Criekinge, John Kurhanewicz, David M Wilson, Donna M Peehl, Robert Bok and Zhen J Wang. “***Patient-Derived Tissue Culture Model Systems of Renal Cell Carcinoma for development of Clinically Translatable Metabolic Biomarkers***” presented at the American Association for Cancer Research special conference titled ‘*The Translational Impact of Model Organisms in Cancer.*’ 2013, San Diego, USA
3. Poster Presentation: Renuka Sriram, Mark Van Criekinge, Ailin Hansen, Kayvan R Keshari, Justin Delos Santos, David M Wilson, Donna M Peehl, John Kurhanewicz and Zhen J Wang. “***Metabolic Dynamics of Patient-derived Renal Cell carcinoma Tissues Using Clinically Translatable Hyperpolarized <sup>13</sup>C Pyruvate***” presented at the World Molecular Imaging Congress (WMIC) 2014, Seoul, Korea.
4. Oral Presentation: Renuka Sriram, Mark Van Criekinge, Ailin Hansen, Zhen J Wang, David M Wilson, Kayvan R Keshari and John Kurhanewicz and. “***Real time measurement of hyperpolarized lactate production and efflux as a biomarker of tumor aggressiveness in a MR compatible 3D cell and tissue culture bioreactor***” to be presented at the ISMRM Workshop on *Magnetic Resonance in Cancer: Challenges & Unmet Needs* in Austin, TX, USA in November 2014.
5. Oral Presentation: Renuka Sriram, Mark Van Criekinge, Ailin Hansen, Bertram Koelsch, Jeremy Gordon, Celine Baligand, Robert Bok, Dan B. Vigneron, David M. Wilson, Peder Larson, Kayvan R. Keshari, Zhen J. Wang and John Kurhanewicz. “**Establishment of**

**patient-derived models of renal cell carcinoma to study metabolism and develop relevant clinical biomarkers”** presented at World Molecular Imaging Congress (WMIC) 2015, Honolulu, Hawaii, USA

### III. EMPLOYMENT

Based on the research experience afforded by this fellowship, I have been able to secure a Professional Researcher position at the University of California, San Francisco.

### CONCLUSION:

In summary, we have shown using hyperpolarized magnetic resonance, increased lactate production in renal tumors in general, and importantly, increased lactate efflux in clear cell renal cancers (the most common subtype of renal cancers) using patient derived tissue slice cultures and can be used to differentiate it from benign renal tumors. Additionally, we have developed an alternative to orthotopic tissue slice grafts in animals by using RCC human cells to capture a range of aggressive renal tumors. And have shown using such a model several approaches to non-invasively assess renal tumor aggressiveness based on lactate production and efflux that is correlated to LDH activity and MCT4 respectively. This is of great impact as these two factors, LDH and MCT4, are strongly linked to pathological grade of renal cancers in patients {Fisel:2013da, Fisel:2015cx, Gerlinger:2012eu}. Subsequently, we hope to implement the *in vivo* model system and use hyperpolarized carbon-13 technique to monitor therapeutic efficacy. Due to the easy clinical translation of the techniques developed herein, these findings are highly valuable and advance the knowledge of renal cancer metabolism.

### REFERENCES:

- [1] M. Sun, R. Thuret, F. Abdollah, G. Lughezzani, J. Schmitges, Z. Tian, S. F. Shariat, F. Montorsi, J. J. Patard, P. Perrotte, and P. I. Karakiewicz, “Age-adjusted incidence, mortality, and survival rates of stage-specific renal cell carcinoma in North America: a trend analysis,” *European Urology*, vol. 59, no. 1, pp. 135–141, Jan. 2011.
- [2] K. R. Keshari, R. Sriram, M. Van Criekinge, D. M. Wilson, Z. J. Wang, D. B. Vigneron, D. M. Peehl, and J. Kurhanewicz, “Metabolic reprogramming and validation of hyperpolarized <sup>13</sup>C lactate as a prostate cancer biomarker using a human prostate tissue slice culture bioreactor,” *Prostate*, vol. 73, no. 11, pp. 1171–1181, Aug. 2013.
- [3] V. Tugnoli, G. Bottura, G. Fini, A. Reggiani, A. Tinti, A. Trincherro, and M. R. Tosi, “<sup>1</sup>H-NMR and <sup>13</sup>C-NMR lipid profiles of human renal tissues,” *Biopolymers*, vol. 72, no. 2, pp. 86–95, 2003.
- [4] F. Podo, “Tumour phospholipid metabolism,” *NMR Biomed.*, vol. 12, no. 7, pp. 413–439, Nov. 1999.
- [5] A. E. Thong, H. Zhao, A. Ingels, M. P. Valta, R. Nolley, J. Santos, S. R. Young, and D. M. Peehl, “Tissue slice grafts of human renal cell carcinoma: an authentic preclinical model with high engraftment rate and metastatic potential,” *Urol. Oncol.*, vol. 32, no. 1, pp. 43.e23–30, Jan. 2014.
- [6] P. E. Larson, A. B. Kerr, A. P. Chen, M. S. Lustig, M. L. Zierhut, S. Hu, C. H. Cunningham, J. M. Pauly, J. Kurhanewicz, and D. B. Vigneron, “Multiband excitation pulses for hyperpolarized <sup>13</sup>C dynamic chemical-shift imaging,” *J Magn Reson*, vol. 194, no. 1, pp. 121–127, Sep. 2008.

- [7] A. Z. Lau, A. P. Chen, R. E. Hurd, and C. H. Cunningham, "Spectral-spatial excitation for rapid imaging of DNP compounds," *NMR Biomed.*, vol. 24, no. 8, pp. 988–996, Jul. 2011.
- [8] P. E. Larson, S. Hu, M. Lustig, A. B. Kerr, S. J. Nelson, J. Kurhanewicz, J. M. Pauly, and D. B. Vigneron, "Fast dynamic 3D MR spectroscopic imaging with compressed sensing and multiband excitation pulses for hyperpolarized  $^{13}\text{C}$  studies," *Magn Reson Med*, vol. 65, no. 3, pp. 610–619, Mar. 2011.
- [9] Y. Xing, G. D. Reed, J. M. Pauly, A. B. Kerr, and P. E. Z. Larson, "Optimal variable flip angle schemes for dynamic acquisition of exchanging hyperpolarized substrates," *Journal of Magnetic Resonance*, vol. 234, pp. 75–81, Sep. 2013.
- [10] C. L. Swisher, B. Koelsch, S. Sukumar, R. Sriram, R. D. Santos, Z. J. Wang, J. Kurhanewicz, D. Vigneron, and P. Larson, "Dynamic UltraFast 2D EXchange Spectroscopy (UF-EXSY) of Hyperpolarized Substrates," *Journal of Magnetic Resonance*, Jun. 2015.
- [11] P. Miao, S. Sheng, X. Sun, J. Liu, and G. Huang, "Lactate dehydrogenase a in cancer: A promising target for diagnosis and therapy," *IUBMB Life*, vol. 65, no. 11, pp. 904–910, Nov. 2013.
- [12] P. Fisel, V. Stühler, J. Bedke, S. Winter, S. Rausch, J. Hennenlotter, A. T. Nies, A. Stenzl, M. Scharpf, F. Fend, S. Kruck, M. Schwab, and E. Schaeffeler, "MCT4 surpasses the prognostic relevance of the ancillary protein CD147 in clear cell renal cell carcinoma," *Oncotarget*, vol. 6, no. 31, pp. 30615–30627, Oct. 2015.
- [13] M. Gerlinger, C. R. Santos, B. Spencer-Dene, P. Martinez, D. Endesfelder, R. A. Burrell, M. Vetter, M. Jiang, R. E. Saunders, G. Kelly, K. Dykema, N. Rioux-Leclercq, G. Stamp, J.-J. Patard, J. Larkin, M. Howell, and C. Swanton, "Genome-wide RNA interference analysis of renal carcinoma survival regulators identifies MCT4 as a Warburg effect metabolic target," *J. Pathol.*, vol. 227, no. 2, pp. 146–156, Apr. 2012.
- [14] K. R. Keshari, R. Sriram, B. L. Koelsch, M. Van Criekinge, D. M. Wilson, J. Kurhanewicz, and Z. J. Wang, "Hyperpolarized  $^{13}\text{C}$ -pyruvate magnetic resonance reveals rapid lactate export in metastatic renal cell carcinomas," *Cancer Research*, vol. 73, no. 2, pp. 529–538, Jan. 2013.
- [15] B. L. Koelsch, K. R. Keshari, T. H. Peeters, P. E. Z. Larson, D. M. Wilson, and J. Kurhanewicz, "Diffusion MR of hyperpolarized  $^{13}\text{C}$  molecules in solution," *Analyst*, vol. 138, no. 4, pp. 1011–1014, Feb. 2013.
- [16] D. Le Bihan, E. Breton, D.ALLEMAND, P. Grenier, E. Cabanis, and M. Laval-Jeantet, "MR imaging of intravoxel incoherent motions: application to diffusion and perfusion in neurologic disorders," *Radiology*, vol. 161, no. 2, pp. 401–407, Nov. 1986.
- [17] P. Fisel, S. Kruck, S. Winter, J. Bedke, J. Hennenlotter, A. T. Nies, M. Scharpf, F. Fend, A. Stenzl, M. Schwab, and E. Schaeffeler, "DNA Methylation of the SLC16A3 Promoter Regulates Expression of the Human Lactate Transporter MCT4 in Renal Cancer with Consequences for Clinical Outcome," *Clinical Cancer Research*, vol. 19, no. 18, pp. 5170–5181, Sep. 2013.



Appendix I



# Cancer Research

## Hyperpolarized $^{13}\text{C}$ -Pyruvate Magnetic Resonance Reveals Rapid Lactate Export in Metastatic Renal Cell Carcinomas

Kayvan R. Keshari, Renuka Sriram, Bertram L. Koelsch, et al.

*Cancer Res* Published OnlineFirst November 30, 2012.

<b>Updated version</b>	Access the most recent version of this article at: doi: <a href="https://doi.org/10.1158/0008-5472.CAN-12-3461">10.1158/0008-5472.CAN-12-3461</a>
<b>Supplementary Material</b>	Access the most recent supplemental material at: <a href="http://cancerres.aacrjournals.org/content/suppl/2012/11/30/0008-5472.CAN-12-3461.DC1.html">http://cancerres.aacrjournals.org/content/suppl/2012/11/30/0008-5472.CAN-12-3461.DC1.html</a>

<b>E-mail alerts</b>	<a href="#">Sign up to receive free email-alerts</a> related to this article or journal.
<b>Reprints and Subscriptions</b>	To order reprints of this article or to subscribe to the journal, contact the AACR Publications Department at <a href="mailto:pubs@aacr.org">pubs@aacr.org</a> .
<b>Permissions</b>	To request permission to re-use all or part of this article, contact the AACR Publications Department at <a href="mailto:permissions@aacr.org">permissions@aacr.org</a> .



# Hyperpolarized $^{13}\text{C}$ -Pyruvate Magnetic Resonance Reveals Rapid Lactate Export in Metastatic Renal Cell Carcinomas

Kayvan R. Keshari<sup>1</sup>, Renuka Sriram<sup>1</sup>, Bertram L. Koelsch<sup>2</sup>, Mark Van Criekinge<sup>1</sup>, David M. Wilson<sup>1</sup>, John Kurhanewicz<sup>1,2</sup>, and Zhen J. Wang<sup>1</sup>

## Abstract

Renal cell carcinomas (RCC) are a heterogeneous group of tumors with a wide range of aggressiveness. Noninvasive methods to confidently predict the tumor biologic behavior and select appropriate treatment are lacking. Here, we investigate the dynamic metabolic flux in living RCC cells using hyperpolarized  $^{13}\text{C}$ -pyruvate magnetic resonance spectroscopy (MRS) combined with a bioreactor platform and interrogated the biochemical basis of the MRS data with respect to cancer aggressiveness. RCC cells have significantly higher pyruvate-to-lactate flux than the normal renal tubule cells. Furthermore, a key feature distinguishing the localized from the metastatic RCC cells is the lactate efflux rate, mediated by the monocarboxylate transporter 4 (MCT4). The metastatic RCC cells have significantly higher MCT4 expression and corresponding higher lactate efflux, which is essential for maintaining a high rate of glycolysis. We show that such differential cellular transporter expression and associated metabolic phenotype can be noninvasively assessed via real-time monitoring of hyperpolarized  $^{13}\text{C}$ -pyruvate-to-lactate flux. *Cancer Res*; 73(2); 1–10. ©2012 AACR.

## Introduction

The incidence of renal tumors, both malignant renal cell carcinomas (RCC) and benign renal tumors, has increased significantly in the last 20 years (1). In the case of renal tumors, biopsies are not routinely done, due to the risk of hemorrhage and high likelihood of indeterminate histology (2, 3). Treatment selection is thus heavily reliant on noninvasive imaging assessment of tumor masses. However, there are significant limitations to the current imaging methods for renal tumor characterization. It is increasingly recognized that RCCs are a heterogeneous group of tumors with a wide range of biologic aggressiveness (4, 5). Emerging active surveillance data have shown that a significant percentage of small RCCs (<4 cm) are indolent with low metastatic risk, and patients may be over-treated if all such RCCs are surgically removed (5, 6). On the other hand, 20% to 40% of patients undergoing nephrectomies for clinically localized RCCs develop metastases with poor outcome (7). Unfortunately, current imaging methods cannot reliably predict the risks of progression from localized RCC to metastatic disease (8). Furthermore, certain benign renal tumors are difficult to distinguish from RCCs by imaging

(9). This diagnostic challenge has resulted in the unnecessary resection of many benign renal tumors, which constitute 20% of all renal tumors less than 4 cm, with the associated surgical risks and potential loss of renal function (10). Therefore, new imaging methods are needed to predict the biologic behavior of renal tumors and select appropriate treatment.

The unique metabolism of cancer cells is central to their malignant behavior. For example, a common property of cancers is altered glucose metabolism with elevated glycolysis and lactate production in the presence of oxygen (11, 12). Increased glycolysis facilitates the uptake and incorporation of nutrients and biomass needed for cell proliferation in cancers (13, 14) and acidifies the extracellular microenvironment-promoting invasion of neighboring tissue and metastasis (15). A number of genomics and proteomics studies have shown increased metabolism to lactate in RCCs (16–19). Specifically, proteomic analysis of RCC tissues and metabolic profiling of serum samples revealed increased levels of glycolytic enzymes in RCC tissues and higher lactate in the serum of patients with RCC (19). Metastatic RCCs have also shown a bioenergetic shift toward aerobic glycolysis and lactate production (18). These studies provide the rationale for metabolic imaging of glycolysis as a noninvasive means to characterize renal tumor aggressiveness.

Hyperpolarized  $^{13}\text{C}$  magnetic resonance is a new molecular imaging technique that allows rapid and noninvasive monitoring of dynamic pathway-specific metabolic and physiologic processes. Hyperpolarization, achieved through the dynamic nuclear polarization (DNP) technique (20), can provide dramatic gains in sensitivity (>10,000-fold increase) for imaging  $^{13}\text{C}$ -labeled biomolecules. The hyperpolarized  $^{13}\text{C}$ -probes can be injected into living systems, and their metabolism can be observed in real-time by chemical shift. The most commonly

**Authors' Affiliations:** <sup>1</sup>Department of Radiology and Biomedical Imaging, University of California, San Francisco; and <sup>2</sup>UCSF Graduate Program in Bioengineering, University of California, Berkeley, San Francisco, California

**Note:** Supplementary data for this article are available at Cancer Research Online (<http://cancerres.aacrjournals.org/>).

**Corresponding Author:** Kayvan R. Keshari, Department of Radiology and Biomedical Imaging, University of California, San Francisco, 1700 4th St., Byers Hall 203, San Francisco, CA 94158. Phone: 415-514-9717; Fax: 415-514-9711; E-mail: [kayvan.keshari@ucsf.edu](mailto:kayvan.keshari@ucsf.edu)

doi: 10.1158/0008-5472.CAN-12-3461

©2012 American Association for Cancer Research.

used hyperpolarized  $^{13}\text{C}$  probe is  $^{13}\text{C}$ -pyruvate, which is at the juncture of several important energy and biosynthetic pathways. For example, pyruvate may be converted to lactate in glycolysis, to acetyl-CoA to support the tricarboxylic acid (TCA) cycle, or to alanine via transamination for protein synthesis. Hyperpolarized  $^{13}\text{C}$ -pyruvate magnetic resonance has already been applied to the detection of the presence (21–25) and progression (26, 27) of a number of cancers. The metabolic changes seen in RCCs suggest that hyperpolarized  $^{13}\text{C}$ -pyruvate will also be an excellent probe to interrogate these tumors noninvasively.

In this work, we compared the pyruvate metabolism of immortalized cells derived from human renal proximal tubules (the origin of most human RCCs), a localized human RCC, and a metastatic human RCC, with the goal of identifying clinically translatable hyperpolarized biomarkers of renal tumor aggressiveness. After evaluating the steady-state metabolism of these cells, we assessed the dynamic hyperpolarized pyruvate-to-lactate flux using a magnetic resonance compatible bioreactor platform that provides a controlled and physiologic setting for the cells (28). By monitoring the real-time metabolic flux using hyperpolarized magnetic resonance, we showed that RCC cells have significantly higher pyruvate-to-lactate flux than the normal renal proximal tubule cells. Furthermore, we showed that cells derived from the metastatic RCC have more rapid export of lactate to the extracellular space compared with the cells derived from the localized RCC, and that these differences are likely mediated by the differential expression of monocarboxylate transporter 4 (MCT4). These results suggest that using hyperpolarized  $^{13}\text{C}$ -pyruvate to assess lactate production and export has the potential to improve the noninvasive characterization of renal tumors.

## Materials and Methods

### Cell lines

HK-2 is an immortalized proximal tubule epithelial cell line from normal adult human kidney (29) and was obtained from American Type Culture Collection [ATCC; obtained June, 2010; authentication conducted at ATCC was via short tandem repeat (STR) profiling]. UMRC6 cells are representative of localized human clear cell RCC (30), and were a gift from Dr. Bart Grossman (MD Anderson Cancer Center, Houston, TX; obtained January, 2010; authenticated using STR profiling, October 2012). UOK262 cells are derived from a metastasis of the highly aggressive hereditary leiomyomatosis RCC (HLRCC), which is characterized by mutation of the TCA cycle enzyme fumarate hydratase (31). UOK262 cells were a gift from Dr. W. Marston Linehan (National Cancer Institute, Bethesda, MD; obtained May, 2010; authenticated using STR profiling, October 2012). All cells were grown in Dulbecco's Modified Eagle's Medium (DMEM) with 4.5 g/L glucose. The cells were passaged serially and were used for assays and magnetic resonance experiments between passages 2 to 10 and at 60% to 80% confluency.

### $^1\text{H}$ NMR experiments

Cells were plated on 150-cm<sup>2</sup>-coated Petri dishes (Fisher Scientific) and incubated for 24-hours in DMEM media supplemented with [1- $^{13}\text{C}$ ] glucose, or for 2-hours in DMEM media

supplemented with [3- $^{13}\text{C}$ ] pyruvate (Cambridge Isotope Laboratories). At the end of incubation, an aliquot of medium was collected, and cells were extracted in ice-cold methanol (32). The cell extracts were reconstituted in D<sub>2</sub>O with known amounts of trimethyl silyl pentanoate (TSP) for internal reference. The extracts were measured on Bruker Advance III 800 MHz equipped with a cryo-cooled triple-resonance probe. High-resolution water-suppressed proton spectra were obtained with a repetition time of 12 seconds and 64 averages. The metabolite peak areas were quantified against the known TSP peak area.

### Hyperpolarized [1- $^{13}\text{C}$ ] pyruvate magnetic resonance bioreactor experiment

Cells were electrostatically encapsulated into 2.5% w/v alginate microspheres as previously described (28, 33), and then loaded into a magnetic resonance-compatible bioreactor. Approximately 800  $\mu\text{L}$  of microspheres were perfused in the bioreactor with DMEM H-21 media at a flow rate of 2.5 mL/min. For the flow rate modulation bioreactor experiments, the flow rate was changed to either 1.3 or 3.8 mL/min for the duration of the hyperpolarized scans. The media was kept at 37°C with water-jacketed perfusion lines and was maintained at 95% air/5% CO<sub>2</sub> via gas exchanger. All bioreactor studies were conducted on a 500 MHz Varian Inova (Agilent Technologies) with a 10 mm, triple-tune, direct-detect, broadband probe at 37°C. For the hyperpolarized  $^{13}\text{C}$ -pyruvate studies, 2.5  $\mu\text{L}$  of 14.2 mol/L  $^{13}\text{C}$ -pyruvate mixed with 15 mmol/L of the trityl radical (GE Healthcare) was polarized on a Hypersense polarizer (Oxford Instruments). This was followed by dissolution in 5 mL of 50 mmol/L phosphate buffer. One milliliter of the resulting 7.5 mmol/L hyperpolarized pyruvate solution was injected into the bioreactor containing the microspheres. Hyperpolarized  $^{13}\text{C}$  magnetic resonance data were acquired dynamically with a 10° flip-angle, pulse repetition time of 3 seconds and for a duration of 300 seconds.  $^{31}\text{P}$  spectra (repetition time 3 seconds, 1,024 averages, 90° flip-angle) were acquired before and after each hyperpolarized study to assess cell viability.

### Cell number determination for bioreactor experiments

Moles of ATP per cell for each cell line were measured using CellTiter-Glo luminescent cell viability assay and Veritas Luminometer (Promega). Moles of ATP corresponding to the  $\beta$ -nucleoside triphosphates ( $\beta$ -NTP) peak area on  $^{31}\text{P}$  spectra were determined using a  $^{31}\text{P}$  calibration curve. The number of cells in each bioreactor experiment was then calculated by dividing the moles of ATP approximated from  $\beta$ -NTP peak by the moles of ATP per cell as measured by the luminescent assay.

### mRNA expression and enzyme activity assay

Total RNA was purified from cells using RNeasy procedure kit (Qiagen), and reverse transcribed using iScript cDNA Synthesis kit (BioRad Laboratories). PCR was conducted in triplicate for the lactate dehydrogenase- $\alpha$  (LDH- $\alpha$ ) and the monocarboxylate transporters 1 and 4 (Hs00161826\_m1, Hs00358829\_m1) on the ABI 7900HT (Applied Biosystems).

Cyclophilin and  $\beta$ -actin (Applied Biosystems) were used as control, and the relative fold difference was calculated for each primer/probe combination.

LDH activity of cell lysates was measured spectrophotometrically by quantifying the linear decrease in NADH absorbance at varying pyruvate concentrations at 339 nm using a microplate reader (Tecan Group Ltd.). The maximum velocity ( $V_{\max}$ ) and the Michaelis–Menten constant ( $K_m$ ) were estimated using the Lineweaver–Burke plot.

### Data analysis

The hyperpolarized pyruvate-to-lactate flux was calculated using a previously published model (28). The pyruvate-to-lactate flux was normalized by the number of cells in each bioreactor study and the injected amount of hyperpolarized pyruvate.  $^{31}\text{P}$  metabolite peaks were integrated and normalized by the number of cells to determine the concentration of phosphocholine (PC), glycerophosphocholine (GPC) and  $\beta$ -NTP. Resonances were corrected for their respective  $^{31}\text{P}$   $T_1$  relaxation times (Supplementary Table S2). One-way ANOVA was used to assess the difference between the 3 groups with Tukey–Kramer method *post hoc* tests using statistical software package JMP (SAS Institute). All values are reported as mean  $\pm$  SE.

## Results

### $^1\text{H}$ MRS shows steady-state metabolite concentrations that reflect increased glycolysis and truncated TCA cycle in metastatic UOK262 cells

We first used  $^1\text{H}$  magnetic resonance spectroscopy (MRS) to interrogate the steady-state metabolite concentrations in HK2, UMRC6, and UOK262 cells. HK2 cells are derived from human renal proximal tubule cells (doubling time = 72–96 hours; ref. 29). UMRC6 cells (doubling time = 43 hours) originate from a localized human clear cell RCC (30). Finally, UOK262 cells were isolated from a metastasis of HLRCC (doubling time = 23 hours; ref. 31). HLRCC is an aggressive RCC characterized by mutation of the TCA cycle enzyme fumarate hydratase. UOK262 cells therefore have markedly reduced oxidative phosphorylation and are highly glycolytic (31). Figure 1A illustrates the biochemical scheme of glycolysis and TCA cycle. Figure 1B shows the major steady-state intracellular metabolite concentrations, as measured by  $^1\text{H}$  MRS, in the 3 cell lines. We found that the steady-state lactate concentration was significantly higher in the UOK262 cells compared with the UMRC6 or HK2 cells (both  $P < 0.05$ ). The increased steady-state lactate in the UOK262 cells is consistent with the fumarate hydratase mutation, which sharply attenuates the mitochondrial TCA cycle and concomitantly drives glycolysis for energy production (31).

The alanine concentration was lower in the 2 RCC cell lines compared with the HK2 cells, likely due to increased flux of pyruvate to lactate. We also found significantly increased glutamate and decreased aspartate concentration in the UOK262 cells compared with the other 2 cell lines. Glutamate is reversibly formed from  $\alpha$ -ketoglutarate, a TCA cycle intermediate proximal to fumarate. Aspartate is formed reversibly from oxaloacetate, a TCA intermediate distal to fumarate. In

the UOK262 cells, the increased steady-state glutamate and reduced aspartate are consistent with truncation of TCA cycle metabolism beyond fumarate, due to the fumarate hydratase mutation. The concentration of GPC, an abundant renal osmolyte (34), was similar among the 3 cell lines. Interestingly, we found that phosphocholine was significantly higher in the UMRC6 cells than the UOK262 cells. While phosphocholine has been used as a biomarker of tumor proliferation and aggressiveness in other types of cancers (35, 36), the levels of phosphocholine did not correlate with aggressiveness in the RCC cell lines in our study. Phosphocholine is converted from choline by the enzyme choline kinase- $\alpha$  (CHKA) in the phosphatidylcholine synthesis (Kennedy) pathway. A recent study reported that CHKA forms a complex with EGF receptor (EGFR) in a c-Src–dependent manner, and functions cooperatively with EGFR and c-Src in regulating pathways critical to cell proliferation (37). Such required functional interaction among the 3 enzymes for cancer cell proliferation may in part explain the lack of direct correlation between the phosphocholine levels and proliferation rates/aggressiveness of the 2 RCC cell lines in our study.

### Twenty-four-hour labeling of cells with $[1-^{13}\text{C}]$ glucose or $[3-^{13}\text{C}]$ pyruvate in 2D cell cultures shows increased flux to lactate in the metastatic UOK262 cells

To further characterize glycolysis and lactate production in the RCC cells, we investigated the flux from labeled  $[1-^{13}\text{C}]$  glucose to lactate in 2-dimensional (2D) cell cultures following 24-hour incubation. Figure 2A shows the scheme of  $^{13}\text{C}$ -labeled carbon atom transitions used to detect glucose metabolism to lactate. Glucose, the primary fuel for energy in cells, is taken up primarily via the glucose transporter 1 (GLUT1) and is converted to pyruvate and then lactate during glycolysis. Lactate is preferentially exported out of the cells via the MCT4 (38). Figure 2B and C show representative MRS of metabolites in the culture medium and intracellular compartment, respectively, of UOK262 cells following 24-hour labeling with  $[1-^{13}\text{C}]$  glucose. Figure 2D and E show the concentrations of  $^{13}\text{C}$ -labeled lactate in the medium and the intracellular compartment, respectively, of the 3 cell lines following incubation with  $[1-^{13}\text{C}]$  glucose. After 24 hour of incubation with  $[1-^{13}\text{C}]$  glucose, 99% of lactate was found in the extracellular medium. The concentration of  $^{13}\text{C}$  lactate in the medium increased progressively from HK2 to UMRC6 to UOK262 cells, with the lactate concentration being nearly 3-fold higher in the medium of UOK262 cells compared with that of the HK2 cells. The fractional enrichment of lactate was defined as the  $^{13}\text{C}$ -labeled lactate/ $(^{13}\text{C}$ -labeled lactate + unlabeled lactate). The fractional enrichment of lactate in the medium was  $76\% \pm 1\%$ ,  $65\% \pm 2\%$ , and  $84\% \pm 1\%$  in the HK2, UMRC6, and UOK262 cells, respectively. This implies that the predominant source of lactate in these cells is glucose although there is a contribution from other carbon sources as well. The intracellular concentration of  $^{13}\text{C}$  lactate was also significantly higher in the UOK262 cells compared with the UMRC6 or the HK2 cells ( $P < 0.05$ ). The intracellular fractional enrichment of lactate was  $62.5\% \pm 3.1\%$ ,  $61.8\% \pm 1.5\%$ , and  $78.6\% \pm 0.4\%$  in the HK2, UMRC6, and UOK262 cells, respectively. The differential lactate

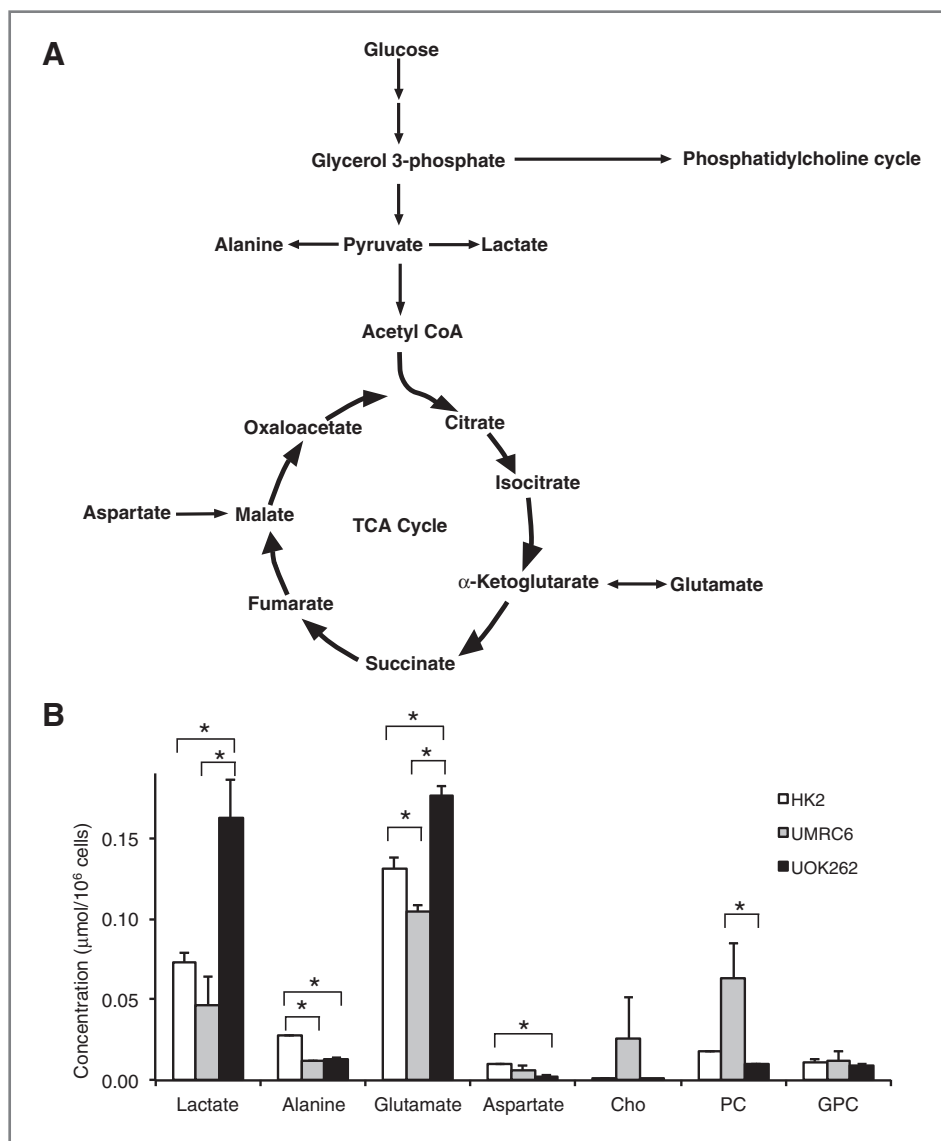


Figure 1. Steady-state major metabolites in the 3 cell lines. A, biochemical scheme of glycolysis and TCA cycle. B, steady-state concentrations of major metabolites, as measured by <sup>1</sup>H MRS, in the 3 cell lines (*N* = 5 each). All values are reported as mean ± SE. \*, significant difference (*P* < 0.05).

fractional enrichment in the intracellular compartment and the medium might be related to lactate compartmentalization in the cells. Such compartmentalization has been reported to exist in the brain and myocardium (39, 40). It is possible that one compartment of intracellular lactate originates predominantly from <sup>13</sup>C-labeled glucose, and the subsequently labeled lactate is preferentially exported into the medium. Another compartment of lactate may derive from other sources such as from glutamine via glutaminolysis (41), and this compartment of lactate may not be as readily exported into the medium as that from glucose. The presence of lactate compartmentalization may also in part explain the higher fractional enrichment of intracellular lactate in the UOK262 cells compared with the other cells. Because UOK262 have fumarate hydratase mutation with reduced TCA cycle metabolism, they are more likely to produce lactate from glycolysis than from other pathways such as glutaminolysis that contains parts of the TCA cycle. This may explain the higher fractional enrichment

of the intracellular lactate from labeled glucose in the UOK262 cells. Taken together, the earlier findings confirmed that UOK262 cells are highly glycolytic with increased production of lactate. Interestingly, the <sup>13</sup>C lactate concentration was lower in the UMRC6 RCC cells relative to both HK2 and UOK262 cells. This was in agreement with the steady-state intracellular lactate concentration data, which also showed a decreased lactate pool in UMRC6 cells compared with the other 2 cell lines (Fig. 1B).

#### Hyperpolarized <sup>13</sup>C MRS shows higher real-time pyruvate-to-lactate flux in RCC cells compared with normal HK2 cells but lower pyruvate-to-lactate flux in the metastatic UOK262 cells than the localized UMRC6 cells

Given the dynamic nature of cellular metabolism, we then investigated the real-time pyruvate metabolism in the 3 cell lines using hyperpolarized <sup>13</sup>C magnetic resonance. We carried



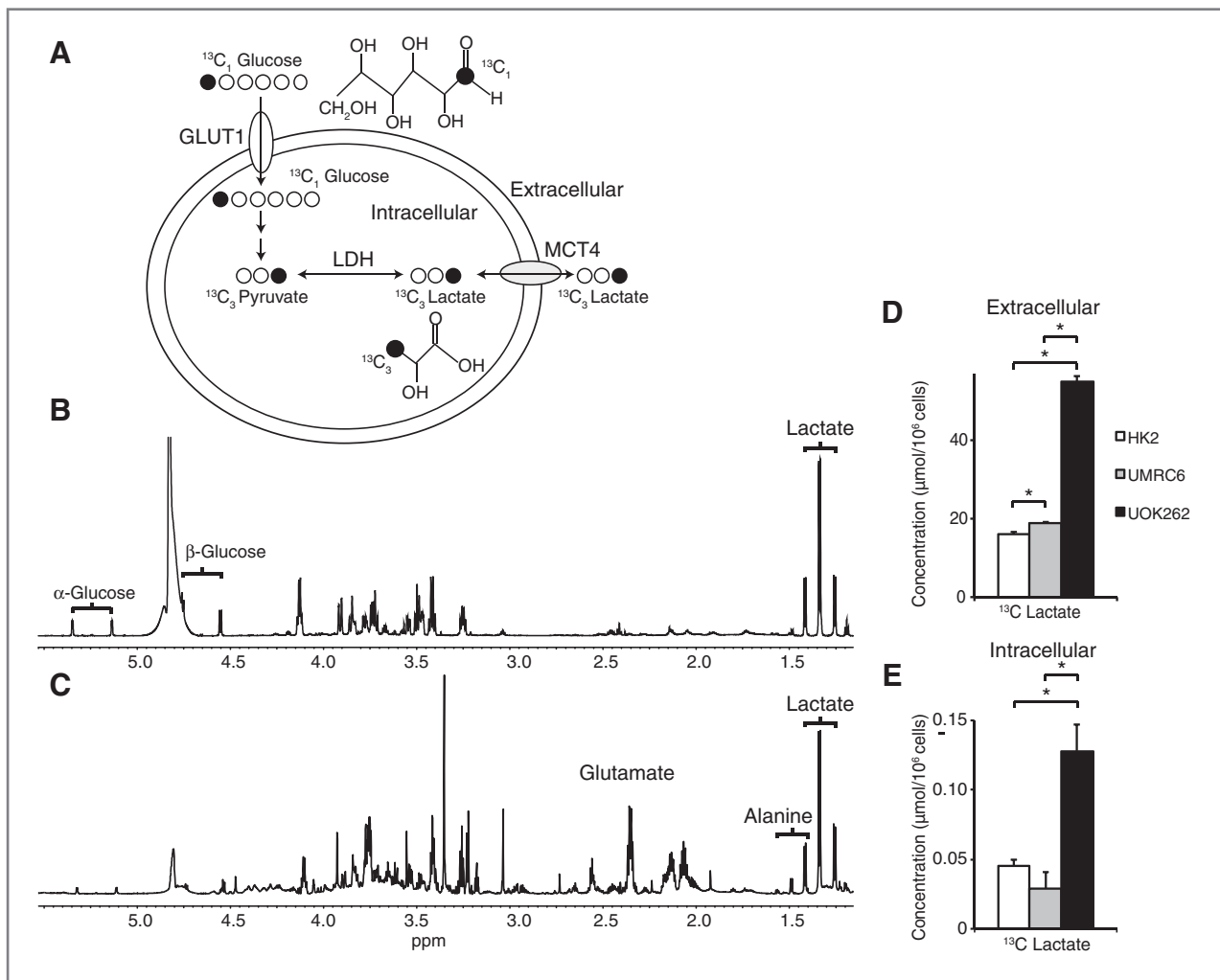


**Figure 2.**  $^{13}\text{C}$ -labeled lactate in the media and intracellular compartment of the 3 cell lines following 24-hour incubation with  $[1-^{13}\text{C}]$  glucose. A, biochemical scheme illustrating  $^{13}\text{C}$ -labeled carbon atom transitions used to detect glucose metabolism to lactate. Representative  $^1\text{H}$  MRS of metabolites in the medium (B) and intracellular compartments (C) of UOK262 following 24-hour labeling with  $[1-^{13}\text{C}]$  glucose. The brackets indicate the  $^{13}\text{C}$  satellites of each metabolite. Concentrations of  $^{13}\text{C}$ -labeled lactate in the media (D) and intracellular compartment (E) of the 3 cell lines following incubation with  $[1-^{13}\text{C}]$  glucose ( $N = 5$  each). All values are reported as mean  $\pm$  SE. \*, significant difference ( $P < 0.05$ ).

out our hyperpolarized  $^{13}\text{C}$  magnetic resonance experiments using a bioreactor, a continuously perfused 3-dimensional (3D) cell culture system that provides a controlled and physiologic setting for the cells. This system has been shown to produce highly reproducible hyperpolarized magnetic resonance data (28), and facilitates the characterization of hyperpolarized substrate to metabolite conversion.  $^{31}\text{P}$  MRS was used to monitor changes in cell bioenergetics during the bioreactor studies. Representative  $^{31}\text{P}$  spectra of the cells are shown in Supplementary Fig. S1. Nuclear magnetic resonance (NMR) signals for the NTPs ( $\gamma$ -NTP,  $\alpha$ -NTP, and  $\beta$ -NTP), phosphocholine, inorganic phosphate ( $\text{P}_i$ ), and GPC were readily visible. The total NTP content was unchanged following the injection of hyperpolarized  $^{13}\text{C}$ -pyruvate, indicating maintenance of cell viability during the course of the hyperpolarized experiments. Figure 3 shows the PC/GPC ratios and PC+GPC concentration in the 3 cell lines. We found significantly higher

PC+GPC concentration in the UMRC6 cells compared with the UOK262 cells ( $P < 0.05$ ), which was in agreement with the steady-state  $^1\text{H}$  data from 2D cell culture. In addition to monitoring cell energetics,  $^{31}\text{P}$  spectroscopy also enables quantitative hyperpolarized data analysis by normalizing the hyperpolarized magnetic resonance data with respect to the number of viable cells, through concomitant measurements of  $\beta$ -NTP concentration via  $^{31}\text{P}$  MRS.

Figure 4A illustrates the scheme of  $^{13}\text{C}$ -labeled carbon atom transitions used to detect  $^{13}\text{C}$ -pyruvate metabolism during the hyperpolarized magnetic resonance experiment. After the injection of hyperpolarized  $^{13}\text{C}$ -pyruvate into the bioreactor, the real-time pyruvate-to-lactate flux was assessed for all 3 cell lines. The data were fit to a 2-state model of interconversion of pyruvate to lactate and the metabolic fluxes were calculated (28). Figure 4B shows fitted pyruvate-to-lactate flux and representative spectra of  $^{13}\text{C}$ -pyruvate and lactate. The average

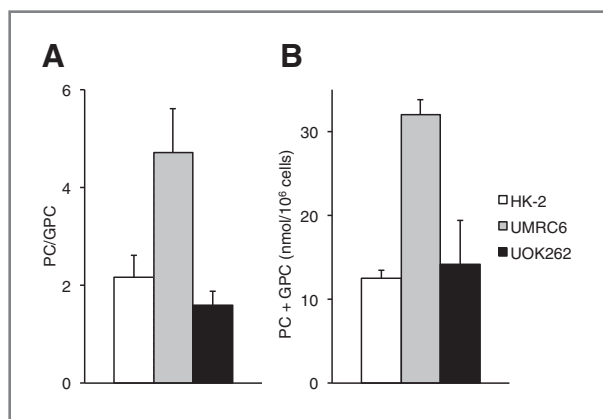


**Figure 3.** Phosphocholine metabolites in the 3 cell lines. PC/GPC ratios (A) and PC+GPC concentration (B) of cells encapsulated and perfused in a bioreactor ( $N = 5$  each). All values are reported as mean  $\pm$  SE.

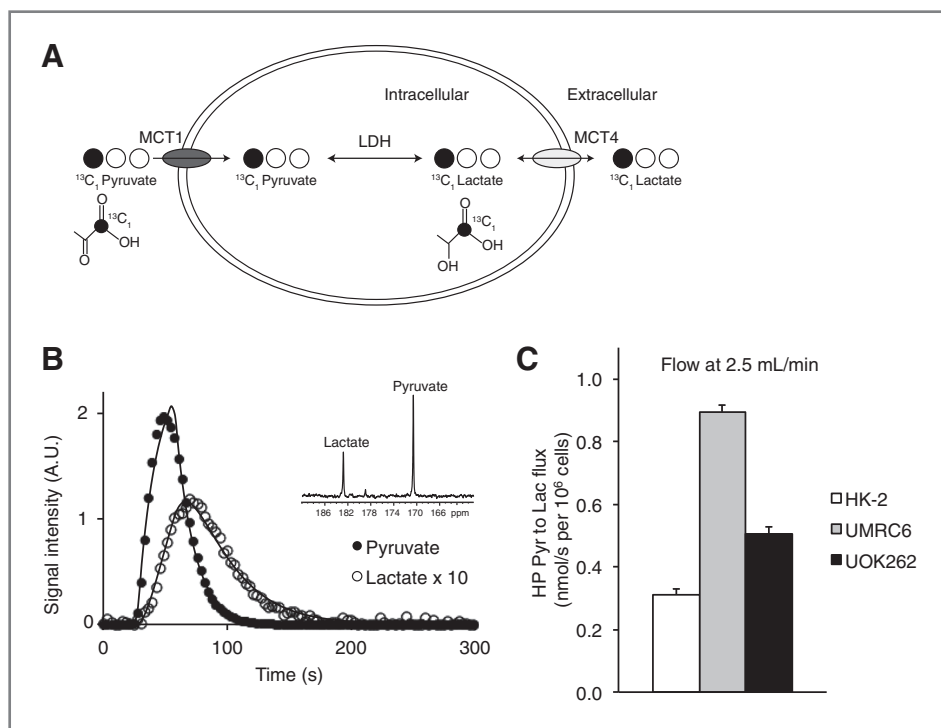
fluxes, at a flow rate of 2.5 mL/min in the bioreactor, for each of these cell lines are shown in Fig. 4C. The observed flux rate was significantly higher in the 2 RCC cell lines (UMRC6 and UOK262) as compared with the renal tubule cell line HK2 (UMRC6 vs. HK2,  $P < 0.0001$ ; UOK262 vs. HK2,  $P = 0.003$ ). Unexpectedly, the observed real-time hyperpolarized pyruvate-to-lactate flux for UOK262 cells (representative of metastatic RCC) was lower than that of the UMRC6 cells (representative of localized RCC). Similar to the flux data, the area under of the curve for the  $^{13}\text{C}$  lactate was higher in the RCC cells than the normal renal tubule cells but was lower in the UOK262 RCC cells than the UMRC6 RCC cells (Supplementary

Table S1). Additional analysis of hyperpolarized  $^{13}\text{C}$  dynamics of the cells perfused in the bioreactors was summarized in Supplementary Table S1.

#### mRNA expression analysis shows increased MCT4 in the metastatic UOK262 cells

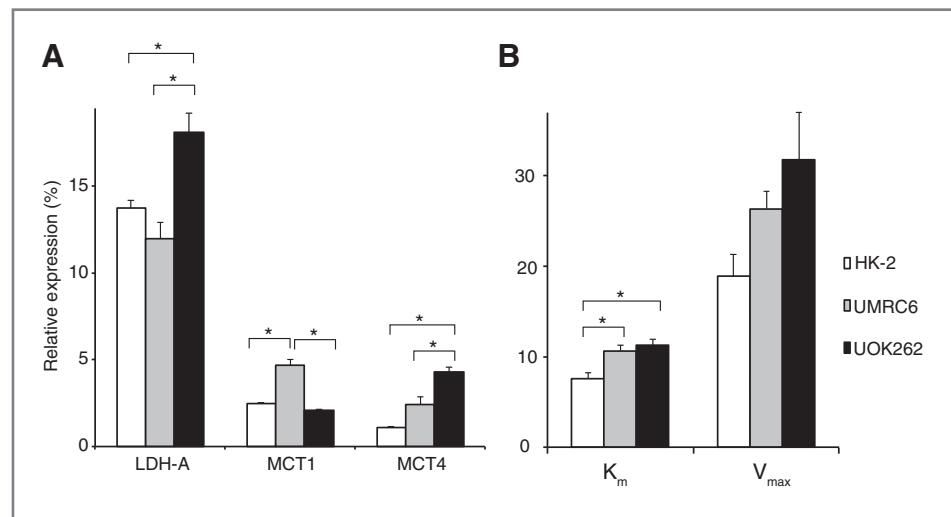
To better understand the cellular processes underlying the hyperpolarized pyruvate flux results, we then assayed the mRNA expression and enzyme activity level of LDHA, and the mRNA expression of MCT1 and MCT4 in the 3 cell lines. LDHA encodes the predominantly M isoform of LDH, which catalyzes the conversion between pyruvate and lactate. MCT1 mediates the pyruvate transport into the cells, and MCT4 mediates the efflux of the lactate out of the cells (42). We found that the mRNA expression of LDHA was significantly higher in the UOK262 cells than the other 2 cell lines (Fig. 5). For the LDH activity,  $K_m$  of the 2 RCC cell lines was significantly higher than that of the HK2 cells ( $P < 0.03$ ) but not significantly different between the UMRC6 and UOK262 RCC cells. The  $V_{max}$  of UOK262 cells was significantly higher than that of HK2 cells ( $P < 0.05$ ). The mRNA expression of MCT1 was significantly higher in the UMRC6 cells (UMRC6 vs. HK2,  $P = 0.0004$ ; UMRC6 vs. UOK262,  $P = 0.0002$ ), whereas the MCT4 expression was significantly elevated in the UOK262 cells (UOK262 vs. HK2,  $P = 0.001$ ; UOK262 vs. UMRC6,  $P = 0.02$ ).

The higher hyperpolarized pyruvate-to-lactate flux in UMRC6 cells, as compared with UOK262, was likely due, in part, to the higher MCT1 expression rather than the lactate pool size in the UMRC6 cells, as both the steady-state and 24-hour labeling data showed lower lactate pool size in the UMRC6 cells (Figs. 1B and 2E). Importantly, the differential



**Figure 4.** Dynamic hyperpolarized pyruvate-to-lactate flux in the 3 cell lines. A, scheme of  $^{13}\text{C}$ -labeled carbon atom transitions used to detect  $\text{C}_1$ -labeled pyruvate metabolism during the hyperpolarized experiment. B, fitted pyruvate-to-lactate flux and representative spectra (inset) of  $^{13}\text{C}$ -pyruvate and lactate in the UMRC6 cells. C, comparison of observed real-time hyperpolarized pyruvate-to-lactate flux in the 3 cell lines at a flow rate of 2.5 mL/min in the bioreactor ( $N = 5$  each). All values are reported as mean  $\pm$  SE.

**Figure 5.** Analysis of relevant enzyme expression/activity and transporter expression in the 3 cell lines. A, mRNA expression of LDHA and monocarboxylate transporters 1 and 4 (MCT1 and MCT4), relative to internal  $\beta$ -actin expression, in the 3 cell lines ( $N = 6$  each). B, LDH activity as measured by  $K_m$  ( $\mu\text{mol pyruvate}/10^6$  cells) and  $V_{\text{max}}$  ( $\mu\text{mol NADH/s}/10^6$  cells) in the 3 cell lines ( $N = 6$  each). All values are reported as mean  $\pm$  SE. \*, significant difference ( $P < 0.05$ ).



expression of MCT4 may explain the apparent discrepancy between the real-time hyperpolarized pyruvate-to-lactate flux and the 24-hours labeling of lactate in the UOK262 cells compared with the UMRC6 cells. The UOK262 cells have an almost 2-fold higher MCT4 expression compared with the UMRC6 cells, suggesting that they likely have more rapid MCT4-mediated export of lactate out of the cells. Rapid lactate efflux is essential for maintaining a neutral intracellular pH, and a high rate of glycolysis and lactate production over time. In contrast, UMRC6 cells have lower MCT4 expression, and likely slower rate of lactate export. Although UMRC6 cells have higher MCT1, these cells would be less able to maintain a high rate of lactate production over time due to buildup of intracellular lactate. Therefore, while the real-time flux of pyruvate to lactate during the timeframe of the hyperpolarized experiment was lower in the UOK262 cells than the UMRC6 cells, the higher MCT4 expression in the UOK262 cells likely resulted in more rapid lactate efflux and accounted for the significantly higher  $^{13}\text{C}$ -labeled lactate accumulated in the medium in the 24-hour labeling experiment. Over time, the large amount of labeled lactate accumulated in the medium of UOK262 cells likely diffused back into the cells down a gradient, and may explain the higher intracellular-labeled lactate in the UOK262 cells compared with the UMRC6 cells. We postulate that, while such diffusion of lactate back into the cells may reduce further generation of labeled lactate, this process occurs after a large amount of lactate has already accumulated in the medium of the UOK262 cells. This accumulation of medium lactate and diffusion back into the UOK262 cells were likely accentuated in the 2D cell cultures in which the extracellular lactate was not removed, in contrast to the bioreactor in which the medium was continuously exchanged.

It is also important to note that while MCT1 may affect the hyperpolarized lactate signal (both the intracellular and extracellular hyperpolarized lactate) if it were the rate-limiting step in the pyruvate-to-lactate flux, the relative proportion of the intracellular versus extracellular hyperpolarized lactate would be determined by MCT4, which modulates the lactate efflux. In addition, lactate efflux in general is not expected to be signif-

icantly affected by MCT1, as most of the lactate produced in the cells is derived from glucose (transported via GLUT1) rather than pyruvate (transported via MCT1) uptake into the cells.

#### Hyperpolarized $^{13}\text{C}$ -pyruvate magnetic resonance combined with flow rate modulation in the bioreactor show rapid efflux of lactate in the metastatic UOK262 cells

We then conducted a second set of hyperpolarized magnetic resonance experiments using different flow rates in the bioreactor to investigate the real-time lactate efflux rate in the 2 RCC cell lines. At high flow rates, the extracellular lactate will more likely flow out of the NMR coil's sensitive volume and will not contribute to the magnetic resonance signal, thereby decreasing the observed pyruvate-to-lactate flux (Fig. 6A). It follows that the relative amount of extracellular lactate (lactate in the medium) of the 2 RCC cell lines, which reflects the lactate efflux rate, can be inferred from the observed hyperpolarized pyruvate-to-lactate flux at different flow rates. Figure 6B shows the pyruvate-to-lactate flux at different flow rates for the 2 RCC cells. For the UMRC6 cells, the mean observed hyperpolarized pyruvate-to-lactate flux was 0.92 nmol/s per  $10^6$  cells at 1.3 mL/min, 0.90 nmol/s per  $10^6$  cells at 2.5 mL/min, and 0.94 nmol/s per  $10^6$  cells at 3.8 mL/min, all of which were not statistically different from one another. For the UOK262 cells, the mean observed hyperpolarized pyruvate-to-lactate flux was 0.56 nmol/s per  $10^6$  cells at 1.3 mL/min, 0.51 nmol/s per  $10^6$  cells at 2.5 mL/min, and 0.41 nmol/s per  $10^6$  cells at 3.8 mL/min. These observed hyperpolarized pyruvate-to-lactate flux for the UOK262 cells progressively decreased at higher flow rate, with a significant 20% decrease in the flux between the 2.5 and 3.8 mL/min flow rate ( $P = 0.01$ ). At the high flow rate of 3.8 mL/min, the decreased pyruvate-to-lactate flux in the UOK262 cells indicated that these cells had more rapid lactate efflux and higher amount of extracellular lactate, which was readily removed from the NMR-sensitive region at high flow rate. The high flow rate should not have significantly limited the MCT1-mediated pyruvate uptake into the

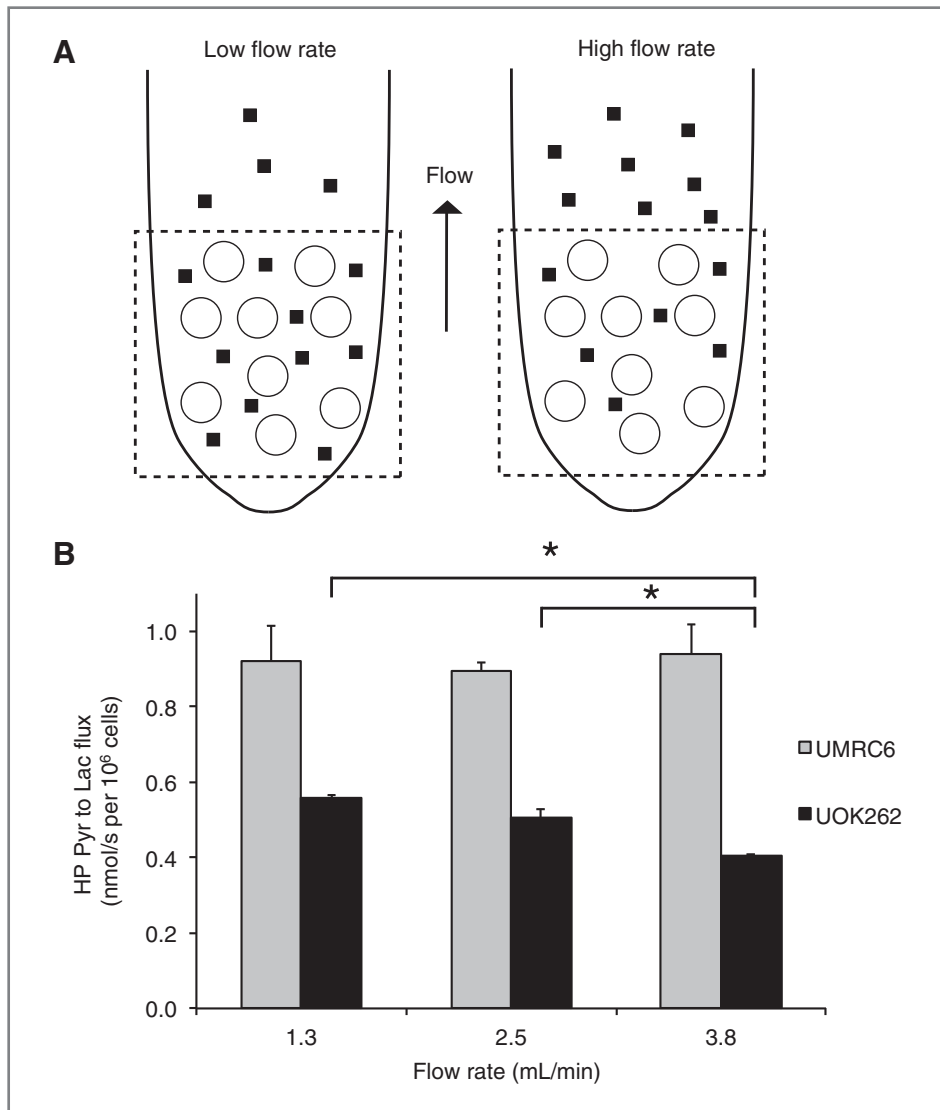


**Figure 6.** Dynamic hyperpolarized pyruvate-to-lactate flux in the RCC cells following flow rate modulation in the bioreactor. **A**, schematic illustrating the relationship between flow rates and observed hyperpolarized pyruvate-to-lactate flux in the bioreactor. At high flow rates, the extracellular lactate will more likely flow out of the NMR coil's sensitive volume and will not contribute to the magnetic resonance signal, thereby decreasing the observed pyruvate-to-lactate flux. The dotted square represents NMR sensitive region. ○, encapsulated microspheres containing cells. ■, extracellular lactate. **B**, hyperpolarized pyruvate-to-lactate flux of UOK262 and UMRC6 cells at 3 different flow rate ( $N = 5$  each). There is a decreasing trend in observed pyruvate-to-lactate flux with increasing flow rate for UOK262 cells. All values are reported as mean  $\pm$  SE. \*, significance ( $P < 0.05$ ).

cells. This is because the injected hyperpolarized pyruvate substrate available to the cells was expected to be in excess compared with MCT1, even at the high flow rate of 3.8 mL/min. Indeed, the UMRC6 cells, with 2-fold higher expression of MCT1 compared with the UOK262 cells, showed similar hyperpolarized pyruvate-to-lactate flux at all 3 flow rates, indicating that the flow rates did not limit pyruvate uptake. The flow rate should also not have affected the enzymatic conversion of pyruvate to lactate in the cells. Taken together, the hyperpolarized flux data at different flow rates strongly support the notion that the UOK262 cells have increased MCT4-mediated lactate efflux out of the cells.

In addition, we incubated the UMRC6 and UOK262 cells for 2 hours in medium containing  $[3-^{13}\text{C}]$  pyruvate, and observed  $0.47 \pm 0.05$  versus  $2.32 \pm 0.27$   $\mu\text{mol}/10^6$  cells of  $^{13}\text{C}$ -labeled lactate in the medium of UMRC6 versus UOK262 cells. This more than 5-fold increase in the extracellular lactate of the UOK262 cells further verifies that lactate derived from labeled pyruvate is produced and transported out of the cells at a

higher rate in the UOK262 cells compared with the UMRC6 cells.

## Discussion

There is increasing evidence that RCCs are among those tumors strongly linked to abnormal metabolism, a feature that may be exploited therapeutically. In this work, we investigated the pyruvate metabolism in perfused human RCC cells using a clinically translatable hyperpolarized  $^{13}\text{C}$  magnetic resonance probe, and interrogated both the biochemical basis of the observed hyperpolarized magnetic resonance data and its relationship to cancer aggressiveness. We found higher pyruvate-to-lactate flux, consistent with increased glycolysis, in RCC cells compared with normal renal proximal tubule cells. We further noted that a key feature distinguishing the localized UMRC6 from the metastatic UOK262 RCC cells is the lactate efflux rate, and that, importantly, this feature can be noninvasively depicted via real-time monitoring of hyperpolarized  $^{13}\text{C}$ -pyruvate-to-lactate flux.



Lactate efflux is predominantly mediated by MCT4, which is a proton-coupled lactate transporter (42), exporting lactate and  $H^+$  in the same direction out of the cells. Rapid lactate efflux serves to maintain high levels of glycolysis in cancer cells and concurrently acidifies the extracellular environment (11). Low extracellular pH supports invasion and metastasis, perhaps due to pH-dependent activation of cathepsins and metalloproteinases that degrade extracellular matrix and basement membranes (43). In this study, we found that the metastatic UOK262 cells have significantly higher MCT4 expression compared with the localized UMRC6 cells, and also have more rapid export of lactate out of the cells. UOK262 cells have mutations in the TCA enzyme fumarate hydratase, which leads to an uncommon and highly aggressive hereditary RCC. However, recent studies have shown that fumarate hydratase mRNA and protein expression are reduced in clear cell RCC, the most common histologic variant of kidney cancer, promoting tumor migration and invasion (44). The reduced fumarate hydratase leads to accumulation of hypoxia inducible factor-2 alpha (HIF-2 $\alpha$ ; ref. 45), a transcription factor known to promote renal carcinogenesis in part by upregulating glycolysis (17). Thus, the metabolic changes observed in the UOK262 cells are likely not unique to this particular RCC type, and the MCT4-mediated lactate efflux may be an important determinant of RCC aggressiveness in general. Supporting this hypothesis, a recent study showed that MCT4 protein expression in primary clear cell RCCs was associated with poorer relapse-free survival, and correlated with Fuhrman nuclear grade (46). In addition, MCT4 knockdown RCC cell lines had reduced intracellular pH, impaired proliferation, and increased apoptosis (46). These studies indicate that MCT4 targeting may also be an important strategy for the treatment of RCCs.

We showed that the MCT4-mediated lactate efflux in living cells can be explored noninvasively using hyperpolarized  $^{13}C$  magnetic resonance. This was accomplished by monitoring the real-time cellular pyruvate-to-lactate fluxes under different flow rates in the bioreactor. While our study used an *ex vivo* system, interrogation of lactate export using hyperpolarized  $^{13}C$  magnetic resonance can be achieved *in vivo*. For example, it is possible to measure the tumoral extracellular or interstitial pH, which in part reflects the amount of exported lactate, using hyperpolarized  $^{13}C$  bicarbonate magnetic resonance (47, 48). Moreover, it is possible to discriminate the local environment of hyperpolarized metabolites using diffusion weighting *in vivo* (49, 50). Future

studies will develop diffusion-weighted hyperpolarized magnetic resonance that can directly quantify the relative amount of intracellular versus extracellular lactate.

While total lactate levels can also be monitored using  $^1H$  MRS, this approach has limited use in the metabolic evaluation of renal tumors, particularly in the *in vivo* setting. Lactate and lipid peaks usually overlap such that the assessment of lactate is challenging even when methods for lipid suppression are applied. More importantly, the real-time metabolic fluxes, influenced by enzymatic and transporter expression, cannot be captured using  $^1H$  MRS.

In conclusion, we have shown that hyperpolarized  $^{13}C$ -pyruvate MRS enables real-time observation of differential lactate efflux, mediated by MCT4, in living RCC cells of varying aggressiveness. Importantly, as MCT4 and lactate efflux are implicated in the pathogenesis of many types of cancers, hyperpolarized  $^{13}C$  MRS has the potential to noninvasively interrogate tumor aggressiveness and treatment efficacy in a broad range of cancers.

### Disclosure of Potential Conflicts of Interest

No potential conflicts of interest were disclosed.

### Authors' Contributions

**Conception and design:** K.R. Keshari, R. Sriram, B.L. Koelsch, D.M. Wilson, J. Kurhanewicz, Z.J. Wang

**Development of methodology:** K.R. Keshari, R. Sriram, B.L. Koelsch, M. Van Criekinge, J. Kurhanewicz

**Acquisition of data (provided animals, acquired and managed patients, provided facilities, etc.):** K.R. Keshari, R. Sriram, B.L. Koelsch, M. Van Criekinge, J. Kurhanewicz, Z.J. Wang

**Analysis and interpretation of data (e.g., statistical analysis, biostatistics, computational analysis):** K.R. Keshari, R. Sriram, B.L. Koelsch, M. Van Criekinge, D.M. Wilson, J. Kurhanewicz, Z.J. Wang

**Writing, review, and/or revision of the manuscript:** K.R. Keshari, R. Sriram, B.L. Koelsch, D.M. Wilson, J. Kurhanewicz, Z.J. Wang

**Administrative, technical, or material support (i.e., reporting or organizing data, constructing databases):** K.R. Keshari, B.L. Koelsch, M. Van Criekinge, J. Kurhanewicz

**Study supervision:** K.R. Keshari, J. Kurhanewicz, Z.J. Wang

### Grant Support

This work was supported by NIH P41EB013598 (J. Kurhanewicz), R01CA166766 (D.M. Wilson), and K99EB014328 (K.R. Keshari), Department of Defense Peer Reviewed Cancer Research Concept Award (Z.J. Wang), and Radiological Society of North America Scholar grant (Z.J. Wang).

The costs of publication of this article were defrayed in part by the payment of page charges. This article must therefore be hereby marked *advertisement* in accordance with 18 U.S.C. Section 1734 solely to indicate this fact.

Received August 30, 2012; revised November 16, 2012; accepted November 26, 2012; published OnlineFirst November 30, 2012.

### References

- Patard JJ. Incidental renal tumours. *Curr Opin Urol* 2009;19:454–8.
- Volpe A, Mattar K, Finelli A, Kachura JR, Evans AJ, Geddie WR, et al. Contemporary results of percutaneous biopsy of 100 small renal masses: a single center experience. *J Urol* 2008;180:2333–7.
- Shannon BA, Cohen RJ, de Bruto H, Davies RJ. The value of preoperative needle core biopsy for diagnosing benign lesions among small, incidentally detected renal masses. *J Urol* 2008;180:1257–61.
- Eggner SE, Yossepowitch O, Pettus JA, Snyder ME, Motzer RJ, Russo P. Renal cell carcinoma recurrence after nephrectomy for localized disease: predicting survival from time of recurrence. *J Clin Oncol* 2006;24:3101–6.
- Jewett MA, Mattar K, Basiuk J, Morash CG, Pautler SE, Siemens DR, et al. Active surveillance of small renal masses: progression patterns of early stage kidney cancer. *Eur Urol* 2011;60:39–44.
- Crispen PL, Viterbo R, Boorjian SA, Greenberg RE, Chen DY, Uzzo RG. Natural history, growth kinetics, and outcomes of untreated clinically localized renal tumors under active surveillance. *Cancer* 2009;115:2844–52.
- Lam JS, Shvarts O, Leppert JT, Figlin RA, Beldegrun AS. Renal cell carcinoma 2005: new frontiers in staging, prognostication and targeted molecular therapy. *J Urol* 2005;173:1853–62.

8. Sun M, Shariat SF, Cheng C, Ficarra V, Murai M, Oudard S, et al. Prognostic factors and predictive models in renal cell carcinoma: a contemporary review. *Eur Urol* 2011;60:644–61.
9. Millet I, Doyon FC, Hoa D, Thuret R, Merigeaud S, Serre I, et al. Characterization of small solid renal lesions: can benign and malignant tumors be differentiated with CT? *AJR Am J Roentgenol* 2011;197:887–96.
10. Cooperberg MR, Mallin K, Ritchey J, Villalta JD, Carroll PR, Kane CJ. Decreasing size at diagnosis of stage 1 renal cell carcinoma: analysis from the National Cancer Data Base, 1993 to 2004. *J Urol* 2008;179:2131–5.
11. Gatenby RA, Gillies RJ. Why do cancers have high aerobic glycolysis? *Nat Rev Cancer* 2004;4:891–9.
12. Warburg O. On the origin of cancer cells. *Science* 1956;123:309–14.
13. Vander Heiden MG, Cantley LC, Thompson CB. Understanding the Warburg effect: the metabolic requirements of cell proliferation. *Science* 2009;324:1029–33.
14. Costello LC, Franklin RB. 'Why do tumour cells glycolyse?': from glycolysis through citrate to lipogenesis. *Mol Cell Biochem* 2005;280:1–8.
15. Gatenby RA, Gawlinski ET, Gmitro AF, Kaylor B, Gillies RJ. Acid-mediated tumor invasion: a multidisciplinary study. *Cancer Res* 2006;66:5216–23.
16. Unwin RD, Craven RA, Harnden P, Hanrahan S, Totty N, Knowles M, et al. Proteomic changes in renal cancer and co-ordinate demonstration of both the glycolytic and mitochondrial aspects of the Warburg effect. *Proteomics* 2003;3:1620–32.
17. Semenza GL. HIF-1 mediates the Warburg effect in clear cell renal carcinoma. *J Bioenerg Biomembr* 2007;39:231–4.
18. Langbein S, Frederiks WM, zur Hausen A, Popa J, Lehmann J, Weiss C, et al. Metastasis is promoted by a bioenergetic switch: new targets for progressive renal cell cancer. *Int J Cancer* 2008;122:2422–8.
19. Gao H, Dong B, Liu X, Xuan H, Huang Y, Lin D. Metabonomic profiling of renal cell carcinoma: high-resolution proton nuclear magnetic resonance spectroscopy of human serum with multivariate data analysis. *Anal Chim Acta* 2008;624:269–77.
20. Ardenkjaer-Larsen JH, Fridlund B, Gram A, Hansson G, Hansson L, Lerche MH, et al. Increase in signal-to-noise ratio of >10,000 times in liquid-state NMR. *Proc Natl Acad Sci U S A* 2003;100:10158–63.
21. Chen AP, Albers MJ, Cunningham CH, Kohler SJ, Yen YF, Hurd RE, et al. Hyperpolarized C-13 spectroscopic imaging of the TRAMP mouse at 3T-initial experience. *Magn Reson Med* 2007;58:1099–106.
22. Cunningham CH, Chen AP, Albers MJ, Kurhanewicz J, Hurd RE, Yen YF, et al. Double spin-echo sequence for rapid spectroscopic imaging of hyperpolarized (13)C. *J Magn Reson* 2007;187:357–62.
23. Hu S, Lustig M, Chen AP, Crane J, Kerr A, Kelley DA, et al. Compressed sensing for resolution enhancement of hyperpolarized (13)C flyback 3D-MRSI. *J Magn Reson* 2008;192:258–64.
24. Kurhanewicz J, Bok R, Nelson SJ, Vigneron DB. Current and potential applications of clinical 13C MR spectroscopy. *J Nucl Med* 2008;49:341–4.
25. Golman K, Petersson JS. Metabolic imaging and other applications of hyperpolarized 13C1. *Acad Radiol* 2006;13:932–42.
26. Albers MJ, Bok R, Chen AP, Cunningham CH, Zierhut ML, Zhang VY, et al. Hyperpolarized 13C lactate, pyruvate, and alanine: noninvasive biomarkers for prostate cancer detection and grading. *Cancer Res* 2008;68:8607–15.
27. Zierhut ML, Yen Y, Chen AP, Bok R, Albers MJ, Zhang V, et al. Kinetic modeling of hyperpolarized 13C1-pyruvate metabolism in normal rats and TRAMP mice. *J Magn Reson* 2010;202:85–92.
28. Keshari KR, Kurhanewicz J, Jeffries RE, Wilson DM, Dewar BJ, Van Crielinge M, et al. Hyperpolarized (13)C spectroscopy and an NMR-compatible bioreactor system for the investigation of real-time cellular metabolism. *Magn Reson Med* 2010;63:322–9.
29. Ryan MJ, Johnson G, Kirk J, Fuerstenberg SM, Zager RA, Torok-Storb B. HK-2: an immortalized proximal tubule epithelial cell line from normal adult human kidney. *Kidney Int* 1994;45:48–57.
30. Grossman HB, Wedemeyer G, Ren LQ. Human renal carcinoma: characterization of five new cell lines. *J Surg Oncol* 1985;28:237–44.
31. Yang Y, Valera VA, Padilla-Nash HM, Sourbier C, Vocke CD, Vira MA, et al. UOK 262 cell line, fumarate hydratase deficient (FH–/FH–) hereditary leiomyomatosis renal cell carcinoma: *in vitro* and *in vivo* model of an aberrant energy metabolic pathway in human cancer. *Cancer Genet Cytogenet* 2010;196:45–55.
32. Beckonert O, Keun HC, Ebbels TM, Bundy J, Holmes E, Lindon JC, et al. Metabolic profiling, metabolomic and metabonomic procedures for NMR spectroscopy of urine, plasma, serum and tissue extracts. *Nat Protoc* 2007;2:2692–703.
33. Chandrasekaran P, Seagle C, Rice L, Macdonald J, Gerber DA. Functional analysis of encapsulated hepatic progenitor cells. *Tissue Eng* 2006;12:2001–8.
34. Nakanishi T, Burg MB. Osmoregulation of glycerophosphorylcholine content of mammalian renal cells. *Am J Physiol* 1989;257(4 Pt 1):C795–801.
35. Shah T, Wildes F, Penet MF, Winnard PT Jr, Glunde K, Artemov D, et al. Choline kinase overexpression increases invasiveness and drug resistance of human breast cancer cells. *NMR Biomed* 2010;23:633–42.
36. Eliyahu G, Kreizman T, Degani H. Phosphocholine as a biomarker of breast cancer: molecular and biochemical studies. *Int J Cancer* 2007;120:1721–30.
37. Miyake T, Parsons SJ. Functional interactions between choline kinase alpha, epidermal growth factor receptor and c-Src in breast cancer cell proliferation. *Oncogene* 2012;31:1431–41.
38. Dimmer KS, Friedrich B, Lang F, Deitmer JW, Broer S. The low-affinity monocarboxylate transporter MCT4 is adapted to the export of lactate in highly glycolytic cells. *Biochem J* 2000;350(Pt 1):219–27.
39. Sickmann HM, Schousboe A, Fosgerau K, Waagepetersen HS. Compartmentation of lactate originating from glycogen and glucose in cultured astrocytes. *Neurochem Res* 2005;30:1295–304.
40. Chatham JC, Forder JR. Metabolic compartmentation of lactate in the glucose-perfused rat heart. *Am J Physiol* 1996;270(1 Pt 2):H224–9.
41. Wise DR, Thompson CB. Glutamine addiction: a new therapeutic target in cancer. *Trends Biochem Sci* 2010;35:427–33.
42. Kroemer G, Pouyssegur J. Tumor cell metabolism: cancer's Achilles' heel. *Cancer Cell* 2008;13:472–82.
43. Swietach P, Vaughan-Jones RD, Harris AL. Regulation of tumor pH and the role of carbonic anhydrase 9. *Cancer Metastasis Rev* 2007;26:299–310.
44. Sudarshan S, Shanmugasundaram K, Naylor SL, Lin S, Livi CB, O'Neill CF, et al. Reduced expression of fumarate hydratase in clear cell renal cancer mediates HIF-2alpha accumulation and promotes migration and invasion. *PLoS ONE* 2011;6:e21037.
45. Pollard PJ, Briere JJ, Alam NA, Barwell J, Barclay E, Wortham NC, et al. Accumulation of Krebs cycle intermediates and over-expression of HIF1alpha in tumours which result from germline FH and SDH mutations. *Hum Mol Genet* 2005;14:2231–9.
46. Gerlinger M, Santos CR, Spencer-Dene B, Martinez P, Endesfelder D, Burrell RA, et al. Genome-wide RNA interference analysis of renal carcinoma survival regulators identifies MCT4 as a Warburg effect metabolic target. *J Pathol* 2012;227:146–56.
47. Gallagher FA, Kettunen MI, Day SE, Hu DE, Ardenkjaer-Larsen JH, Zandt R, et al. Magnetic resonance imaging of pH *in vivo* using hyperpolarized 13C-labelled bicarbonate. *Nature* 2008;453:940–3.
48. Wilson DM, Keshari KR, Larson PE, Chen AP, Hu S, Van Crielinge M, et al. Multi-compound polarization by DNP allows simultaneous assessment of multiple enzymatic activities *in vivo*. *J Magn Reson* 2010;205:141–7.
49. Larson PE, Kerr AB, Reed GD, Hurd RE, Kurhanewicz J, Pauly JM, et al. Generating super stimulated-echoes in MRI and their application to hyperpolarized C-13 diffusion metabolic imaging. *IEEE Trans Med Imaging* 2012;31:265–75.
50. Chen AP, Hurd RE, Cunningham CH. Spin tagging for hyperpolarized (1)(3)C metabolic studies. *J Magn Reson* 2012;214:319–23.



## Appendix II



### Hyperpolarized Carbon-13 MRI and MRS Studies

Renuka Sriram, John Kurhanewicz & Daniel B. Vigneron

University of California, San Francisco, CA, USA

Imaging of hyperpolarized nuclei provides significant new insights into previously inaccessible aspects of disease biology. Many of the biomolecules crucial for understanding and monitoring metabolism are present in low concentration and are often beyond the detection threshold of traditional magnetic resonance spectroscopy and imaging. A solution is to improve sensitivity by a factor of 10 000 or more by temporarily redistributing the populations of nuclear spins in a magnetic field, a process termed *hyperpolarization*. Nuclei such as  $^{13}\text{C}$  in metabolically active biomolecules can be hyperpolarized, providing unprecedented gains in sensitivity for imaging biologic compounds. Although the first US National Cancer Institute-sponsored white paper describing the potential of this new molecular imaging technique was published only 3 years ago, over 60 biomolecules have been hyperpolarized and tested in preclinical studies. Moreover, a phase 1 clinical trial of hyperpolarized  $[1-^{13}\text{C}]$ pyruvate in prostate cancer patients has demonstrated that this powerful technology can be translated to the clinic. This review is focused on the dissolution dynamic nuclear polarization (DNP)-based hyperpolarization technique and summarizes the acquisition techniques used for hyperpolarized  $^{13}\text{C}$  imaging, in vivo applications of some of the most promising hyperpolarized  $^{13}\text{C}$  labeled biomolecules, and its clinical translation.

**Keywords:** hyperpolarized dissolution dynamic nuclear polarization (DNP), carbon-13 magnetic resonance imaging (MRI),  $^{13}\text{C}$  magnetic resonance spectroscopic imaging (MRSI), pyruvate, lactate, metabolic imaging, molecular imaging

#### How to cite this article:

*eMagRes*, 2014, Vol 3: 1–14. DOI 10.1002/9780470034590.emrstm1253

### Introduction

In vivo hyperpolarized (HP)  $^{13}\text{C}$  MRI is an extraordinary metabolic imaging technique that can provide valuable, new information on previously inaccessible aspects of biological processes in a wide range of disorders including cancer, cardiac disease, diabetes, and liver disease. Hyperpolarized  $^{13}\text{C}$  MR provides a  $>10\,000$ -fold signal enhancement for detecting endogenous, nontoxic  $^{13}\text{C}$ -labeled probes, such as pyruvate, that can monitor enzymatic conversions through key biochemical pathways. This novel technique lifts the prior constraint on MR metabolic imaging, namely poor sensitivity, and owing to its rapid  $<1$  min acquisition time can be integrated into a clinical MR examination. The detection of flux through individual enzyme-catalyzed reactions offers a fundamentally new approach to imaging and understanding disease biology, and this approach is clinically translatable. Another important feature of HP  $^{13}\text{C}$  MR is that it encodes chemical as well as spatial information, thereby providing the potential for using multiple HP MR probes to detect several metabolic and/or physiologic processes simultaneously after the injection of a single bolus.<sup>1–3</sup> A number of  $^{13}\text{C}$  labeled biomolecules other than pyruvate have been suitably HP and preclinical studies have shown the potential for several of these  $^{13}\text{C}$  labeled probes to provide information about metabolism, perfusion, pH, and cellular redox status.<sup>4</sup> Moreover, methods for copolarizing multiple probes have been developed, and such probes have been successfully polarized and injected in preclinical models.<sup>5,6</sup>

For these reasons, HP MR imaging has generated great interest in the imaging community and is the subject of many recent invited review articles,<sup>4,7–24</sup> numerous workshops, a National Cancer Institute (NCI)-sponsored white paper,<sup>25</sup> and a phase 1 clinical trial in prostate cancer patients.<sup>26</sup> Although there are multiple ways to achieve polarization<sup>27–29</sup> in this article, we have focused on the dissolution DNP method of preparing carbon-13 enriched endogenous substrates for both preclinical and clinical in vivo studies.

### Dissolution Dynamic Nuclear Polarization (dDNP)

Hyperpolarized  $^{13}\text{C}$  MRI using the dDNP technique is a powerful in vivo metabolic imaging technique that was originally developed by Ardenkjaer-Larsen *et al.* in 2003.<sup>30</sup> The methods and instrumentation are now being further developed to enable new preclinical and even human studies using sterile, HP metabolites. As HP  $^{13}\text{C}$  MR spectroscopic imaging (MRSI) encodes chemical as well as spatial information, this new molecular imaging technique allows the simultaneous detection of multiple biologic compounds and metabolic products. DNP methodology is based on polarizing nuclear spins in the solid state through coupling of the nuclear spins with unpaired electrons that are added to the sample via an organic free radical.<sup>3,31</sup> In the amorphous solid state, the high-electron spin polarization is in part transferred to the nuclear spins by microwave



irradiation. Critical for in vivo use of this method is the ability to dissolve the polarized, cold solid sample, creating a warm solution while preserving its nuclear polarization. This process was accomplished by scientists from Amersham Biosciences, which is currently part of GE Healthcare. They demonstrated that polarizations of 37% for  $^{13}\text{C}$  can be obtained after dissolution of the polarized solid, with a corresponding signal enhancement of 44 400.<sup>26,30</sup> This HP liquid sample can then be used as a probe for in vivo imaging or spectroscopy, and it has been demonstrated that  $^{13}\text{C}$  angiography with an S/N of  $\approx 275$  can be acquired in  $\approx 0.25$  s after an injection of HP aqueous  $^{13}\text{C}$  urea solution in rat models.<sup>1</sup> A further advantage of using  $^{13}\text{C}$  NMR is that unlabeled tissues are virtually invisible so that signals from the HP substrate and subsequent metabolic products provide the dominant contribution to the NMR acquisition. A long longitudinal relaxation time ( $T_1$ ) is required to maintain the polarization until the time of in vivo imaging. The  $T_1$  values of  $^{13}\text{C}$  in small molecules are significantly longer ( $> 10$  s) than those of protons, particularly when the  $^{13}\text{C}$  is a carbonyl carbon with no adjacent protons. In fact the C-1 carbonyl of pyruvate has a  $T_1$  of  $\approx 70$  s in solution, and sodium pyruvate is well tolerated by animals. These considerations and its well-documented safety profile have led to  $[1-^{13}\text{C}]\text{pyruvate}$  being used as one of the first in vivo HP substrates for metabolic studies.

The DNP polarizer instrumentation approach originally described by Ardenkjaer-Larsen *et al.*<sup>30</sup> has been widely used in the university setting and commercialized by Oxford Instruments in their HyperSense product. This basic hardware was then modified for sterile HP pyruvate generation in a clean room under clinical pharmacy regulation and oversight for the first phase 1 clinical trial.<sup>26</sup> Since recent past, a new DNP instrumentation technology has been developed to polarize simultaneously and dissolve up to four HP  $[1-^{13}\text{C}]\text{pyruvate}$  samples in succession using plastic fluid paths and a novel magnet cryostat which attains  $< 1$  K temperatures with minimal helium usage.<sup>32</sup> For clinical use, compounding and filling take place in a sterile environment, with the vial and fluid path delivered as a preassembled package to be loaded into the polarizer. This new DNP polarizer also enables new preclinical research experiments that benefit from its ability to dissolve in rapid succession, multiple HP samples to study the temporal response of pharmaceutical interventions over a time range of just a few minutes.<sup>33</sup>

## Acquisition Techniques for Hyperpolarized $^{13}\text{C}$ Imaging

The acquisition of HP  $^{13}\text{C}$  data requires specialized MR scanner hardware, pulse sequences, reconstruction methods, and analysis techniques. A major temporal challenge arises from the typically subminute  $T_1$  relaxation times of the carbon-13 nucleus in the parent molecule and its metabolic products that cause the HP signal to decay back to its thermal equilibrium. The detectable  $^{13}\text{C}$  signal for MRI is a function of the degree of polarization, the  $T_1$  relaxation time, the concentration of the metabolite, and the specific metabolic processes that the  $^{13}\text{C}$  labeled molecule undergoes. The available time for imaging with an initial signal enhancement of 10 000 is

approximately five times the  $T_1$  relaxation time. Also each RF excitation, being repeatedly applied during data acquisition, typically causes a substantial loss of HP signal. Therefore acquisition methods that minimize the number of RF pulses can greatly improve the resulting signal-to-noise ratio (SNR) of the HP MR data. For single time-point acquisitions, the choice of time-window is dictated by the delivery and uptake rate of the injected HP compound and the rate of conversion to its downstream metabolic products in the tissue/tumor region of interest.

Owing to the nonrenewable nature of the magnetization and fast decay, signal-sampling schemes need to minimize the acquisition time and the number of excitation pulses, and maximize the retention of polarized signal. A wide variety of acquisition strategies have been developed to maximize the SNR and resolution, while minimizing the number of excitations.<sup>34,35</sup> For slice- or coil-only localized spectroscopy, commonly a short repetition time (TR, as compared with  $T_1$ ) and a small flip-angle pulse and acquire sequence have been employed.<sup>2,36</sup>

MRI, MR spectroscopy (MRS), and hybrid approaches have all been used for the acquisition of HP  $^{13}\text{C}$  MR data. In some studies just a single resonance is excited and then imaged using a rapid spatial encoding scheme.<sup>7</sup> In others, spectroscopic imaging provides distributions of multiple resonances simultaneously. To address the reduction in signal caused by  $T_1$  decay, many studies have made use of small-tip-angle pulse sequences.<sup>1,2,30,37–40</sup> Variable flip-angle approaches have been utilized as well: these approaches are designed to maximize sampling of the available polarization while providing approximately constant signal following each data acquisition,<sup>41</sup> rather than the progressively declining signal that occurs with a constant flip-angle excitation scheme. To optimize this approach, the approximate  $T_1$  relaxation time(s) in vivo must be known and the flip-angle needs to be accurately calibrated.

For HP  $^{13}\text{C}$  MRSI, it is important to consider that optimal detection of biomedical information requires optimal sampling not only in the spectral domain but also in the spatial and temporal domains. This necessitates spectral encoding with sufficient spectral resolution and bandwidth, along with spatial imaging encoding with the required spatial resolution. Several fast spectroscopic imaging approaches have been developed and applied to provide spatial and spectral information on the uptake and metabolism of HP probes.<sup>3,41,42</sup> Single-slice two-dimensional spectroscopic imaging with elliptical central k-space sampling has provided both spatial and spectral information in a rapid acquisition for preclinical cardiac measurements.<sup>42</sup> A three-dimensional volume sampling approach employing phase encoding in two spatial dimensions and an echo-planar readout gradient in the third dimension have been widely used for 15-s  $^{13}\text{C}$  spectroscopic imaging, both preclinically<sup>3,41</sup> and in patients.<sup>26</sup> However, the latter approach provides just one set of spatial distribution data with limited coverage, and averages the metabolic changes occurring over that time period. Recent acquisition developments have focused on greatly accelerating data acquisition using fast echo-planar spectroscopic imaging (EPSI) and spiral

readouts as well as compressed sensing and parallel imaging. These methods also benefit the detection of dynamic HP signal changes. By combining EPSI and compressed sensing in spatial and temporal dimensions, serial volumetric HP  $^{13}\text{C}$  data can be acquired with a 2 s time resolution, and with a 34-fold acceleration compared to conventional MRSI encoding.<sup>43</sup> Another important method for accelerating HP MR acquisitions is parallel signal reception, similar to that used widely for clinical parallel imaging with phased array coils. Specialized eight-channel coils tuned to the carbon-13 frequency have been developed and tested to provide highly accelerated HP 3-D MR data in preclinical animal studies prior to their future application in human studies.<sup>44</sup>

Specialized multiband RF pulses have been developed to reduce the RF excitation of the initially polarized substrate, thus leaving significantly more polarization available for detection of the metabolic products.<sup>45,46</sup> These pulses apply a smaller tip-angle to the frequency of the substrate and a larger tip-angle to the resonances of the products. This approach has improved the SNR of the products by preserving the polarization of the substrate, and allowed serial spectroscopic imaging with a time resolution of 2 s to monitor the temporal dynamics of  $[1-^{13}\text{C}]$ pyruvate uptake and metabolism.<sup>46</sup>

While numerous preclinical studies and the aforementioned clinical trial have shown that the pyruvate  $T_1$  is more than long enough to obtain valuable biomedical data, other groups are developing agents with longer  $T_1$  values, utilizing long-lived single states.<sup>47,48</sup> These advances could significantly broaden the applicability of HP  $^{13}\text{C}$  to detect biological process on a longer time scale.

## In Vivo Applications of Hyperpolarized $^{13}\text{C}$ MRI

As previously mentioned, a challenge facing HP MR is the relatively short duration of the polarization, and the impact of specific metabolic processes on the  $T_1$  of the HP probe. This means that to study metabolism, the HP substrate must be rapidly transported via the bloodstream to the tissue of interest, be quickly taken up by the cell, and be promptly metabolized in a manner that does not overly restrict the rotational freedom (correlation time) of the HP probe. Furthermore (unlike PET tracers), the amount of substrate that must be injected is in the physiologic range and in cases involving supraphysiologic boluses, could alter metabolic processes. If the HP substrate is to be used in the clinic then it must also be nontoxic at these relatively high concentrations. Approximately 60 biomolecules have been polarized and tested in preclinical studies to date. Even if only a small percentage of these substrates make it to the clinic, it is already clear that these could provide unique and important information on disease severity, prognosis, and treatment response. In discussing the potential of HP substrates for imaging cellular metabolism in cancer and other diseases, perhaps the best approach is to discuss the substrates or probes that have been successfully HP and to describe how they have been used in preclinical models and the information they provide.

## Metabolism of Hyperpolarized Pyruvate

$[1-^{13}\text{C}]$ Pyruvic acid has been the prototype HP substrate due to its ease of polarization, water solubility, long  $T_1$ , central role in cell metabolism, and its rapid uptake and metabolism in cells<sup>8</sup>. Pyruvate is the end product of glycolysis. It is reduced by the enzyme lactate dehydrogenase (LDH) with the cofactor nicotinamide adenine dinucleotide (NADH) to generate lactate, which has been the most well-studied reaction by HP MR. At steady state, the kinetics of LDH can be characterized as an ordered bireactant scheme, specifically a Theorell–Chance mechanism. First the enzyme binds the reduced dinucleotide cofactor (NADH) and then it binds the substrate pyruvate and catalyzes its reduction to the product lactate via a hydride transfer. At high concentrations of pyruvate, LDH has been shown to be substrate-inhibited, and the concentration of pyruvate in the cell is tightly regulated in glycolysis.<sup>8</sup> Pyruvate is rapidly transported into the cell by members of the monocarboxylate transporter (MCT) family, predominantly MCT1, and the magnitude of conversion to labeled lactate can be, but is not always, limited by the specific activity of MCT. For example, it has been shown that pyruvate transport into the cell is the limiting factor for the formation of lactate in certain cells such as breast and renal cell carcinoma and not in prostate cells such as PC3.<sup>49,50</sup> Once in the cell, the high availability of NADH and LDH allows for near instantaneous conversion to lactate, and it is important to note that if the lifetime of the pyruvate–LDH complex was long during the conversion to lactate, the HP signal would decrease more rapidly because of an increased molecular correlation time.<sup>8</sup> In addition, several published studies have demonstrated that the majority of the HP signal arises from  $^{13}\text{C}$  label exchange between pyruvate and lactate pools, which depend on the equilibrium pool sizes rather than net synthesis.<sup>4,51–53</sup> Once reduced, the HP lactate is incorporated into the intracellular lactate pool. However, HP lactate can also be transported out of the cell within the time frame of the HP study, predominantly through MCT4, which has also been shown to be upregulated in cancer cells.<sup>50</sup>

Alternatively, pyruvate undergoes transamination with glutamate to form alanine, in the reaction catalyzed by alanine transaminase (ALT). This reaction is readily reversible in the cell and therefore the polarized  $^{13}\text{C}$  label introduced in  $[1-^{13}\text{C}]$ pyruvate can effectively exchange with preexisting pools of alanine.<sup>52</sup> A third reaction involves the irreversible decarboxylation of  $[1-^{13}\text{C}]$ pyruvate to HP  $^{13}\text{C}$ -labeled carbon dioxide in the reaction catalyzed by the mitochondrial enzyme pyruvate dehydrogenase (PDH). The carbon dioxide released is subsequently interconverted with bicarbonate through both carbonic anhydrase and acid–base chemistry, providing a measure of intracellular pH.

As described later, the reactions catalyzed by LDH and ALT have been observed to be altered in cancer<sup>23</sup> as is the expression of the MCT which mediates pyruvate uptake and lactate export.<sup>54</sup> Production of  $^{13}\text{CO}_2$ , and in turn  $^{13}\text{C}$  bicarbonate, has been linked to changes in cardiac status<sup>17</sup> as well as response to chemotherapeutics.

It is important to emphasize that, as a consequence of the inherent chemical information in the  $^{13}\text{C}$  NMR spectrum, it is possible to detect the metabolic fate of HP  $[1-^{13}\text{C}]$ pyruvate

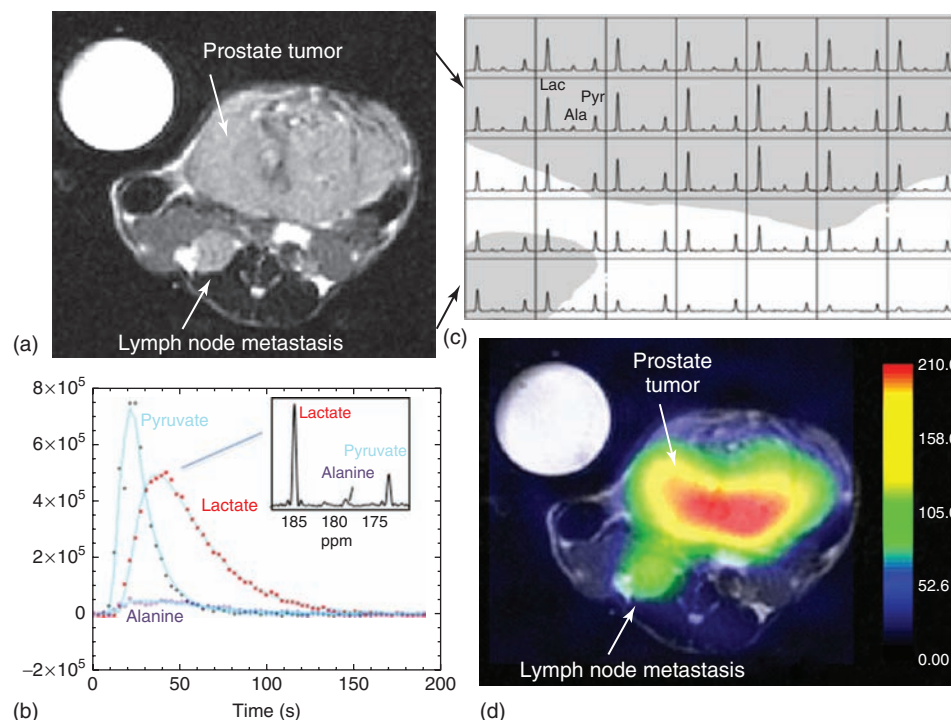


**Figure 1.** Spectral and spatially resolved dynamic hyperpolarized imaging on TRAMP mice. (a)  $T_2$  weighted proton image of a high-grade TRAMP tumor with arrows pointing to the primary tumor as well as the lymph node metastasis. (b) Hyperpolarized  $^{13}\text{C}$  spectral peak height plots showing the time courses for the signals of hyperpolarized  $[1-^{13}\text{C}]$ pyruvate and its metabolic products following the injection of  $350\ \mu\text{l}$  of hyperpolarized pyruvate. The pyruvate was injected at a constant rate from 0 to 12 s. The MR spectra were acquired every 3 s using a  $5^\circ$  flip angle and a 10 mm thick slice. The peak height plot was corrected for the amount of magnetization used to record the previous  $n$  spectra by dividing each peak height by  $\cos^n(5^\circ)$ . The hyperpolarized pyruvate quickly reached a maximum at 24 s before being converted to lactate and alanine. (c) The 3-D MRSI  $^{13}\text{C}$  data was recorded between 35 and 49 s (based on the dynamic plot in b), a time when the hyperpolarized lactate signal was roughly constant. The hyperpolarized  $^{13}\text{C}$  spectra represented were normalized to correct for differences in polarization and receiver sensitivity. A double spin-echo pulse sequence with a small variable flip-angle excitation pulse, adiabatic refocusing pulses, and a flyback echo-planar readout trajectory was used to acquire the 3-D MRSI data with a nominal resolution of  $0.14\ \text{cm}^3$  and zero filled to a resolution of  $0.017\ \text{cm}^3$ . (d) Hyperpolarized  $[1-^{13}\text{C}]$ lactate intensity map (ratio to noise) overlaid on  $T_2$  weighted proton image

simultaneously through multiple enzyme-catalyzed reactions in vivo (Figure 1). As described in section titled 'Acquisition Techniques for Hyperpolarized  $^{13}\text{C}$  Imaging,' both fast dynamic  $^{13}\text{C}$  MR as well as high-spatial resolution localized spectroscopic imaging data have been acquired at a single time point using specialized pulse sequences. Figure 1 shows both 1-D slab dynamic HP  $^{13}\text{C}$  MR data and one slice of a 3-D spectroscopic imaging data set from a transgenic murine prostate (TRAMP) cancer model. The HP  $^{13}\text{C}$  MR data was acquired with a double spin-echo pulse sequence using small variable flip-angle excitation pulses, adiabatic refocusing pulses, and a flyback echo-planar readout trajectory.<sup>55</sup> The metabolic data can be overlaid on the corresponding anatomic images as shown for the lactate intensity map in Figure 1(d). The overlaid lactate image shows increased HP lactate production in the primary tumor and an adjacent lymph node metastasis.

Absolute quantification of the HP pyruvate and its metabolites is difficult owing to several factors, including differences in polarization, and simultaneous signal loss due to  $T_1$ , metabolic conversion, and RF sampling. For this reason, ratiometric analyses of pyruvate and lactate signal intensities, as is shown for lactate/noise ratio for prostate cancer in Figure 1(d), has been

the simplest and most commonly used method to distinguish normal from diseased tissues. Another common ratio used is the lactate/pyruvate ratio, which is critically dependent on the delivery of the substrate and the timing of the acquisition, as shown in Figure 1(b). For example, although the single time-point imaging data in Figure 1 was acquired at a time when HP lactate was relatively constant (39–45 s), the HP pyruvate signal was dropping dramatically. This leads to dramatically different lactate/pyruvate ratios depending on the time of the acquisition as well as potential variability in HP pyruvate delivery. The practicality of acquiring localized kinetic data opens the possibility of measuring metabolic fluxes by fitting the dynamic data to kinetic models.<sup>56–58</sup> However, the modeling of metabolic fluxes from HP  $^{13}\text{C}$  MR data is still in its infancy and current approaches suffer from a number factors, including assumed/estimated  $T_1$ 's, unknown pool sizes, unknown metabolite compartmentalization, and the assumptions underlying the specific models used. A simple approach has been to look at the ratio of the area under the dynamic metabolite curves of the precursor and product. Hill *et al.*<sup>59</sup> and Bastiaansen *et al.*<sup>60</sup> have shown that this approach provides similar information to the metabolic fluxes obtained from a two-site exchange analysis.



**[1-<sup>13</sup>C]Pyruvate: Applications to Cancer.** Increased flux of HP pyruvate to lactate, mediated by LDH, has been correlated with an increased pathologic grade in the TRAMP model<sup>55</sup> of prostate cancer. The ability to noninvasively determine prostate cancer grade addresses a critically important question for men diagnosed with prostate cancer: does the patient have an aggressive cancer that needs to be treated aggressively, or indolent disease where treatment can be delayed? Although a large number of men, 233 000 in 2014, are diagnosed with prostate cancer in the United States, only approximately 10% will develop lethal disease and die of metastatic prostate cancer. This has led to significant overtreatment of this common disease, emphasizing a need to be able to image aggressive disease. The fast spectroscopic imaging techniques described earlier can also provide spatially resolved dynamic data of HP pyruvate metabolism and spatially variable uptake of HP pyruvate and HP lactate production in the TRAMP model. This metabolic heterogeneity was shown to correlate with tumor cellularity and necrosis,<sup>43</sup> and could be used to monitor the variable response of these tumors to therapy. Another report has demonstrated significantly higher HP lactate production in two human glioblastoma xenograft models where the blood–brain barrier (BBB) was disrupted relative to normal brain, suggesting that HP MR metabolic imaging may be valuable for assessing prognosis and monitoring response to therapy for patients with brain tumors.<sup>61</sup>

Decreased HP lactate production from pyruvate has correlated with effective treatment for several different cancers and types of therapy.<sup>23</sup> Clinically this provides an invaluable tool, allowing the oncologist to assess the efficacy of a drug at the metabolic level, well before any appreciable change in tumor volume occurs. The decrease in the amount of HP lactate observed after therapy has been attributed to a number of factors, including decreased LDH expression and activity, and/or decreases in tumor cellularity, and/or a loss of the coenzyme NAD(H), depending on the therapy and cancer being investigated.<sup>62</sup> Decreased HP lactate/pyruvate ratio was also observed at 96 h postradiation therapy in a subcutaneous animal model of breast cancer.<sup>63</sup> Zhang<sup>64</sup> has extensively discussed the potential of HP <sup>13</sup>C to assess a number of signaling pathways important to cancers. These findings highlight the value of this technique as a method to confirm drug delivery and drug-target modulation prior to, or in the absence of, apoptosis and a reduction in tumor size. As positron emission tomography (PET) using <sup>18</sup>F-fluorodeoxyglucose (FDG) can provide similar metabolic information as HP pyruvate, it is important to compare these techniques in the setting of monitoring therapy. In one study<sup>65</sup> FDG uptake measured by PET was found to provide an earlier (at 16 h) measure of treatment response than HP [1-<sup>13</sup>C]pyruvate, although at 24 h the two techniques provided similar information. However, HP [1-<sup>13</sup>C]pyruvate may have advantages over FDG PET for certain cancers, such as prostate and brain cancer. In both these cases, the normal tissue has significant glucose or FDG uptake<sup>66,67</sup> and the presence and aggressiveness of the cancer can be better monitored by the metabolic fate of the [1-<sup>13</sup>C]pyruvate taken up.

**[1-<sup>13</sup>C]Pyruvate: Other Applications.** In preclinical studies HP [1-<sup>13</sup>C]pyruvate has demonstrated significant potential for

studying both normal tissues and human diseases other than cancer. For example, HP cardiac [1-<sup>13</sup>C]pyruvate metabolism has been measured both in vivo<sup>68</sup> and in the isolated perfused rat heart.<sup>69,70</sup> Metabolites identified include HP [1-<sup>13</sup>C]lactate, [1-<sup>13</sup>C]alanine, and <sup>13</sup>CO<sub>2</sub>. Fasted animals showed a reduction in HP <sup>13</sup>CO<sub>2</sub> production compared to fed controls and a similar reduction was observed following the induction of type 1 diabetes, where the decrease in <sup>13</sup>CO<sub>2</sub> production correlated with disease severity. Total global ischemia in isolated perfused rat hearts resulted in the production of [1-<sup>13</sup>C]lactate and [1-<sup>13</sup>C]alanine but not H<sup>13</sup>CO<sub>3</sub><sup>−</sup> or <sup>13</sup>CO<sub>2</sub>.

Detection of HP pyruvate and its metabolic products has also been demonstrated in rat liver, with significant differences in metabolism observed for the fed and fasted states. Hyperpolarized pyruvate has also been used to measure ALDH-2 (aldehyde dehydrogenase) activity in ethanol treated rat liver.<sup>71</sup> Increased lactate formation was observed in the rat liver because of an increased availability of NADH formed from catalyzing ethanol to acetate conversion via the alcohol dehydrogenase and aldehyde dehydrogenase pathway. In a recent study<sup>56</sup> the hepatic gluconeogenic pathway was monitored using HP pyruvate in mice with high-fat diet-induced type 2 diabetes. Intermediates of pyruvate anaplerosis, including oxaloacetate (OAA), malate, and aspartate were monitored dynamically. Increased pyruvate carboxylase activity resulted in an increased pool of OAA and a subsequent increase in aspartate compared to control mice. An increase in malate was also observed because of an increase in malate dehydrogenase activity in fatty livers of these mice. Increased HP [1-<sup>13</sup>C]alanine in this model has been observed to be a biomarker of diabetes-induced liver dysfunction as it correlates with the ex vivo ALT activity. This finding is valuable because serum ALT activity is the current clinical ‘gold standard’ to assess hepatotoxicity and this standard suffers from lack of organ specificity in the absence of correlative histomorphological alteration in the liver.<sup>72</sup> Furthermore, this above-mentioned study demonstrated the sensitivity of HP <sup>13</sup>C MR for detecting changes in liver metabolism induced by glucagon administration (increased OAA, aspartate, and bicarbonate) and metformin therapy (decreased OAA, aspartate, and bicarbonate).

While the kidney has been a major organ of interest to study perfusion kinetics with HP pyruvate and urea,<sup>73</sup> a recent study investigated the renal metabolic changes due to diabetes in a streptozotocin rat model.<sup>74</sup> In this type I diabetes animal model, the early metabolic changes associated with the hyperglycemic state were detected via an increased LDH activity in the kidneys resulting in a 1.5-fold increase in the lactate/pyruvate ratio.<sup>74</sup>

The impact of radiation treatment on normal tissues such as the thorax, lung, and heart have been detected using HP [1-<sup>13</sup>C]pyruvate. Specifically, radiation-induced hypoxia led to an increase in anaerobic glycolysis, as measured by a doubling of the lactate/pyruvate ratio of these organs in radiated rats as compared to control animals.<sup>75</sup>

There has been some debate as to whether pyruvate crosses the BBB of the healthy brain rapidly enough to allow metabolism and imaging within the T<sub>1</sub> of HP [1-<sup>13</sup>C]pyruvate. However, a recent study<sup>76</sup> demonstrated detectable cerebral

HP [1-<sup>13</sup>C]pyruvate metabolism when either [1-<sup>13</sup>C]pyruvate, ethyl pyruvate, or the lipophilic ethyl ester of [1-<sup>13</sup>C]pyruvate, were used, although the ethyl pyruvate was taken up and metabolized to a much higher degree. The problem with using ethyl pyruvate is that an equivalent of ethanol is generated in the brain for every [1-<sup>13</sup>C]pyruvate generated. That study demonstrated that either high doses of HP [1-<sup>13</sup>C]pyruvate or ethyl pyruvate may be viable agents for brain imaging even in diseases that do not substantially impact the BBB, for example, infiltrating gliomas, Alzheimer's disease, nonenhancing multiple sclerosis, and acute stroke.

**[2-<sup>13</sup>C]Pyruvate.** When [2-<sup>13</sup>C]pyruvate, is used instead of [1-<sup>13</sup>C]pyruvate,<sup>77</sup> the <sup>13</sup>C-label is incorporated into tricarboxylic acid (TCA) cycle intermediates rather than being released as <sup>13</sup>CO<sub>2</sub>. This makes [2-<sup>13</sup>C]pyruvate an attractive substrate to assess the intermediate oxidative phosphorylation metabolites despite the shorter  $T_1$  ( $\approx 44$  s) of the C-2 of pyruvate compared to the 56 s  $T_1$  of C-1 (at 3 T) and broader line width (30–40%) presumably due to stronger <sup>13</sup>C–<sup>1</sup>H coupling.<sup>78</sup> In the perfused rat heart,<sup>77</sup> the conversion of HP pyruvate to [2-<sup>13</sup>C]lactate, [1-<sup>13</sup>C]acetyl-carnitine, [1-<sup>13</sup>C]citrate, and [5-<sup>13</sup>C]glutamate was observed. However, the very short  $T_1$  (6 s) of [2-<sup>13</sup>C]lactate (and its multiplicity due to <sup>1</sup>H–<sup>13</sup>C spin coupling at the C-2 position) greatly reduces the sensitivity of [2-<sup>13</sup>C]pyruvate for detecting lactate flux. The detection of HP citrate and glutamate allows a measurement of flux through the citric acid cycle, and following cardiac ischemia, the TCA cycle intermediates, [1-<sup>13</sup>C]citrate and [5-<sup>13</sup>C]glutamate, decreased and [2-<sup>13</sup>C]lactate increased.<sup>77</sup>

In the rat brain, increasing the HP pyruvate injection concentration to 125 mM led to the observation of multiple TCA cycle intermediate metabolites including [5-<sup>13</sup>C]glutamate and [1-<sup>13</sup>C]citrate<sup>79</sup> indicating that pyruvate was getting across the BBB in sufficient time for metabolism to occur. By increasing PDH activity through dichloroacetate (DCA) stimulation, detection of HP [1-<sup>13</sup>C]acetyl carnitine signal along with a 40% increase in HP [5-<sup>13</sup>C]glutamate was observed.

**[1,2-<sup>13</sup>C]Pyruvate.** The use of [1,2-<sup>13</sup>C]pyruvate enables an assessment of simultaneous fluxes through both LDH/ALT as well as the TCA cycle with equal sensitivity. However, lower SNR due to <sup>13</sup>C–<sup>13</sup>C coupling of the doubly labeled compound and the overlap of the coupled resonances of C-1 pyruvate–hydrate with [1-<sup>13</sup>C]citrate somewhat reduces the utility of [1,2-<sup>13</sup>C]pyruvate. These limitations can be overcome by increasing the polarization or concentration of [1,2-<sup>13</sup>C]pyruvate and optimizing the detection strategy. [1,2-<sup>13</sup>C]Pyruvate was used to show that it is feasible to detect multiple pathways simultaneously along with intracellular pH in a pig heart, as shown in Figure 2. The dynamic production of [1-<sup>13</sup>C]lactate via glycolysis, and H<sup>13</sup>CO<sub>3</sub><sup>−</sup>, <sup>13</sup>CO<sub>2</sub>, and [5-<sup>13</sup>C]glutamate via the TCA cycle, is shown in Figure 2(b). One of the challenges in measuring intracellular pH from the equilibrium of H<sup>13</sup>CO<sub>3</sub><sup>−</sup> and <sup>13</sup>CO<sub>2</sub> using a modified Henderson–Hasselbalch approach (as described later) is that at physiologic pH, the <sup>13</sup>CO<sub>2</sub> is 10-fold lower in SNR than the H<sup>13</sup>CO<sub>3</sub><sup>−</sup>. To overcome this SNR issue, Chen *et al.* applied

two signal-averaging approaches for increasing the sensitivity of HP CO<sub>2</sub> detection in dynamic trace in Figure 2(c).

### <sup>13</sup>C Bicarbonate

H<sup>13</sup>CO<sub>3</sub><sup>−</sup> polarizes well, has a relatively long  $T_1$  (48.7 s at 11.7 T), and when injected provides a measurement of extracellular rather than intracellular pH. The injected HP H<sup>13</sup>CO<sub>3</sub><sup>−</sup> readily diffuses from the vasculature into extracellular spaces and is quickly interconverted with <sup>13</sup>CO<sub>2</sub> through both carbonic anhydrase and acid–base chemistry, thereby providing a measure of extracellular pH. The pH is calculated using the ratio of H<sup>13</sup>CO<sub>3</sub><sup>−</sup>/<sup>13</sup>CO<sub>2</sub> based on a modification of the Henderson–Hasselbalch equation ( $\text{pH} = \text{pK}_a + \log_{10}([\text{H}^{13}\text{CO}_3^-]/[\text{CO}_2])$ ). As this technique is ratiometric, it does not require a measurement of the HP probe concentration to get an absolute pH measurement, and the ratio changes by a factor of 10 in the physiological pH range. The very rapid interconversion of H<sup>13</sup>CO<sub>3</sub> and <sup>13</sup>CO<sub>2</sub>, catalyzed by carbonic anhydrase, ensures that the  $T_1$ 's of H<sup>13</sup>CO<sub>3</sub> and <sup>13</sup>CO<sub>2</sub> are similar and therefore there is no need to correct for differential polarization decay. pH images can be obtained by measuring the H<sup>13</sup>CO<sub>3</sub>/<sup>13</sup>CO<sub>2</sub> ratio acquired by adopting fast spectroscopic imaging approaches, and studies have shown that the extracellular pH in both lymphoma and prostate cancer was more acidic than that in the surrounding benign tissues.<sup>5,11</sup> This approach could have a large clinical impact given the wide range of pathological states that are associated with an acidic extracellular environment. Bicarbonate is abundant in tissue ( $\sim 25$  mM) and is already infused into patients at the concentrations that would be needed for HP <sup>13</sup>C imaging measurement of tissue pH.

### [1,4-<sup>13</sup>C<sub>2</sub>]Fumarate

Following intravenous injection of HP [1,4-<sup>13</sup>C<sub>2</sub>]fumarate, its metabolism to HP [1,4-<sup>13</sup>C<sub>2</sub>]malate by the enzyme fumarase has been demonstrated in tumors<sup>80</sup> and in skeletal muscle.<sup>81</sup> The signal from HP malate increased significantly in skeletal muscle following ischemia and reperfusion, suggesting that it may be used as a positive contrast agent for identifying ischemic injury. The accumulation of malate in ischemic muscle was suggested to be due to a block in the TCA cycle. However, studies in drug-treated tumors and renal tubular necrosis have demonstrated that the accumulation of malate is due to cellular necrosis.<sup>82</sup> In viable cells the transport rate of fumarate into the mitochondria is too slow to enable the observation of labeled malate within the lifetime of the polarization. However, if this permeability barrier is removed, as it is in necrotic cells, then fumarate conversion to malate can be observed. Therefore fumarate could be a useful agent for detecting treatment response and processes such as acute tubular necrosis before the onset of clinical and histological changes.<sup>83</sup>

### [1-<sup>13</sup>C]Lactate

[1-<sup>13</sup>C]Lactate has been HP and investigated as an in vivo metabolic imaging agent.<sup>84</sup> Following intravenous injection in the TRAMP model, only low levels of HP [1-<sup>13</sup>C]pyruvate were



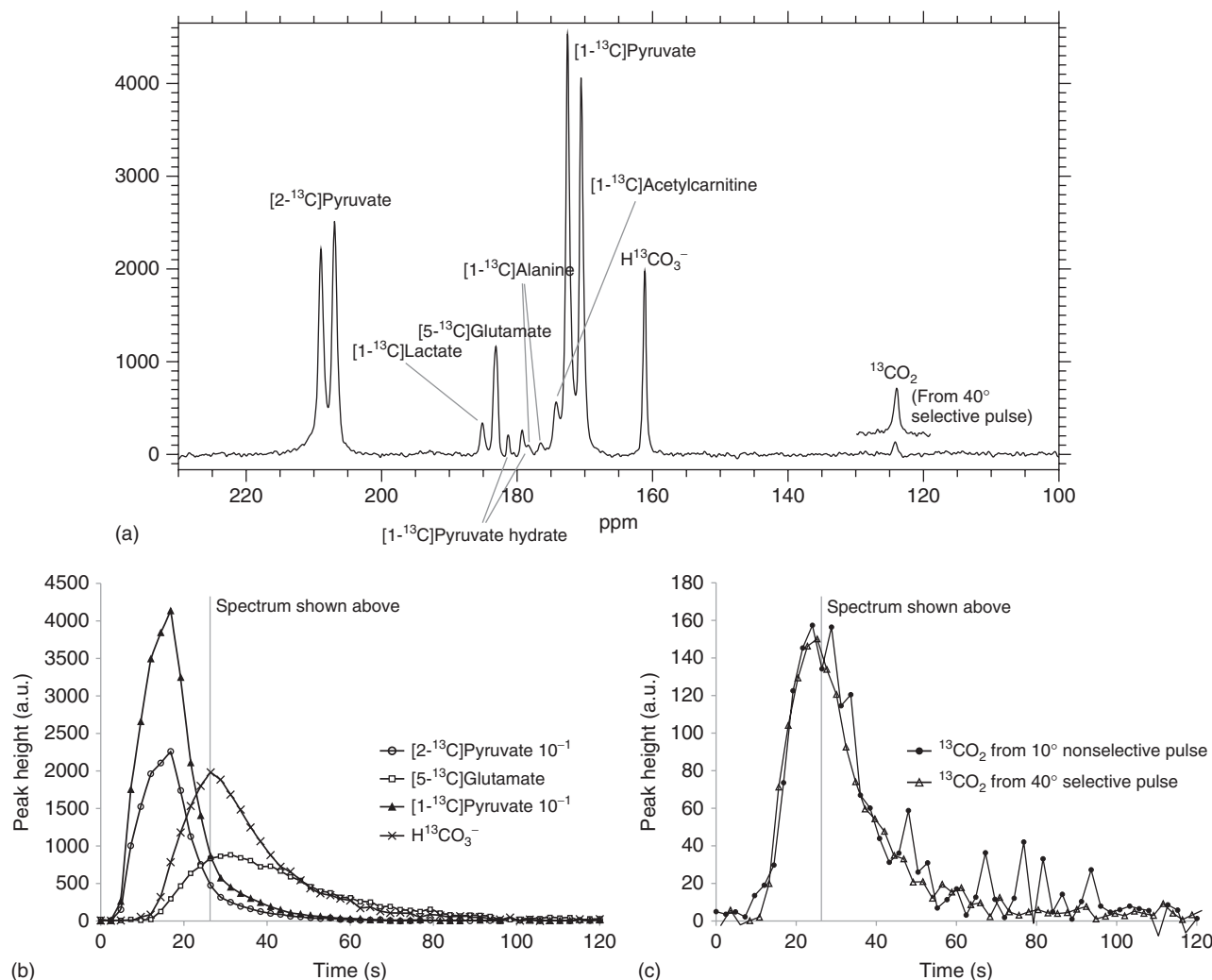


**Figure 2.** In vivo porcine cardiac MRS data after injection of hyperpolarized  $[1,2-^{13}\text{C}_2]$  pyruvate. (a) The  $^{13}\text{C}$  spectrum from one of the dynamic time points; (b, c) the time courses of the substrate and its metabolites are plotted. The  $^{13}\text{CO}_2$  signal amplitudes (corrected for flip angle and echo time) and the time courses from the two interleaved ( $40^\circ$  selective and  $10^\circ$  non-selective pulses) were observed to have good agreement (c). (Adapted with permission from Ref. 78. © John Wiley & Sons, Ltd, 2012)

detected and this presumably reflects exchange of label into a relatively small pool of tissue pyruvate. The HP  $^{13}\text{C}$  label was also diluted by flux into other metabolites, including  $[1-^{13}\text{C}]$ alanine and  $\text{H}^{13}\text{CO}_3^-$ . An important advantage of using lactate to introduce the HP  $^{13}\text{C}$  label is that the concentration of HP lactate in the blood after injection is similar to that seen in an exercising animal; this differentiates it from HP pyruvate which is injected at a concentration which is much higher than is found endogenously.  $[1-^{13}\text{C}]$ Lactate could be a particularly interesting probe for studying cardiac metabolism as it is an important cardiac energy source and the LDH enzyme isoform found in the heart preferentially converts lactate to pyruvate, resulting in more HP  $[1-^{13}\text{C}]$ pyruvate than would be observed in a tumor. It has been shown to mimic the changes observed with pyruvate and hence has been proposed as a safer and more suitable probe for cardiac metabolic studies.<sup>85</sup> Since recent past, lactate has been successfully employed to study carbohydrate

metabolism in skeletal muscle.<sup>86</sup> The altered PDH flux between fed and fasted animals was clearly measured as an alteration in the levels of HP alanine and bicarbonate.

### **[5- $^{13}\text{C}$ ]Glutamine**

Glutamine is important for tumor growth; in many cell lines its utilization is positively correlated with cellular proliferation and its depletion results in cell death. Several cancers increase glutamine consumption through induction of glutamine transporters, as well as an enhanced expression of enzymes that metabolize glutamine, namely glutaminases and glutamate OAA transaminases. Enhanced glutamine metabolism is believed to be a compensatory mechanism related to the flow of citrate out of the TCA cycle, needed to provide acetyl-CoA for fatty acid biosynthesis in proliferating cells. Glutamine, converted to  $\alpha$ -ketoglutarate, provides an essential

carbon source for the TCA cycle in the tumor metabolic phenotype. This altered metabolism may be driven by c-MYC, a transcription factor whose deregulation is common in cancer. MYC has been shown to induce both the expression of glutamine transporters and upregulation of glutaminases.<sup>87</sup> Imaging glutamine metabolism could, therefore, be a marker of tumor growth and division, and glutamine is already safely administered to humans in the clinic. The conversion of HP [5-<sup>13</sup>C]glutamine to [5-<sup>13</sup>C]glutamate, catalyzed by intramitochondrial glutaminase, has been demonstrated in cells in vitro.<sup>88–90</sup> The label in the C-5 position shows a larger chemical shift following conversion to glutamate compared to the C-1 position, which aids in the detection of the metabolite although the  $T_1$  is slightly shorter (25 s versus 16 s at 9.4 T). Owing to the relatively low polarization and slow cellular uptake of [5-<sup>13</sup>C]glutamine there has been only one successful study demonstrating in vivo conversion to glutamate.<sup>90</sup> However, with improved polarization and detection techniques it may be possible to use this substrate to assess the effects of tumor treatment with cytostatic drugs.

### [1-<sup>13</sup>C]Acetate

Acetate is a precursor to acetyl-CoA (acetyl coenzyme A) a central metabolite in fatty acid metabolism as well as the TCA cycle. Acetate, which is readily taken up by skeletal muscle, heart, and liver is converted to acetyl-CoA via acetyl-CoA synthetase (ACS) and further metabolized by carnitine acetyltransferase (CAT) to acetylcarnitine. Following injection of HP [1-<sup>13</sup>C]acetate into mice, both [1-<sup>13</sup>C]acetyl CoA and [1-<sup>13</sup>C]acetyl carnitine were observed in liver and heart, although the acetyl carnitine signal from the heart was higher than in liver, indicating an organ-variation in the distribution of acetate metabolism.<sup>81</sup> Ischemia in skeletal muscle was shown to result in a reduction in acetylcarnitine formation. [1-<sup>13</sup>C]Acetate has been shown to provide an assessment of ACS activity.<sup>60</sup> Carnitine can also modulate fatty acid and carbohydrate metabolism by modifying the intramitochondrial acetyl-CoA/CoA ratio.

### [2-<sup>13</sup>C]-Fructose

As previously discussed, a majority of HP probes involve <sup>13</sup>C labeling of carbonyl carbons due to their lack of directly attached protons and longer  $T_1$  relaxation rates. However, the use of HP probes such as pyruvate cannot investigate upstream glycolytic processes, which are abnormal both in cancer metabolism and other metabolic abnormalities, such as fatty liver disease and diabetes. The carbons of glucose have very short  $T_1$ s (<2 s) due to spin–spin coupling to both directly attached protons as well as with protons on adjacent carbons. The pentose analog of glucose and fructose enters glycolysis through its phosphorylation by hexokinase and yields complementary information to glucose. The C-2 of fructose is a hemiketal that has a relatively longer relaxation time (~16 s at 37 °C) and high solution-state polarization (~12%).<sup>91</sup> Injection of HP [2-<sup>13</sup>C]-fructose into the TRAMP model demonstrated increased uptake and metabolism in regions of prostate cancer relative to surrounding benign abdominal tissues.<sup>91</sup>

### [U-<sup>13</sup>C<sub>6</sub>, <sup>2</sup>H<sub>7</sub>]Glucose

Deuteration of glucose overcomes the handicap of short  $T_1$ s of glucose carbons, extending the  $T_1$ s from <2 s to as long as 15 s, which makes feasible the use of glucose as a substrate for HP DNP. Initial publications by Allouche-Arnon *et al.*<sup>92</sup> showed that in vivo imaging of HP [U-<sup>13</sup>C<sub>6</sub>, <sup>2</sup>H<sub>7</sub>]glucose was feasible, but they did not observe any metabolism. More recently, Rodrigues *et al.*<sup>93</sup> were able to observe the formation of HP [2-<sup>13</sup>C]dihydroxyacetone phosphate and [1-<sup>13</sup>C]6-phosphogluconate along with [1-<sup>13</sup>C]lactate and [<sup>13</sup>C]bicarbonate in untreated lymphoma tumors in a murine model after the injection of [U-<sup>13</sup>C<sub>6</sub>, <sup>2</sup>H<sub>7</sub>]glucose.

### [1-<sup>13</sup>C]Succinate

Succinic acid has been HP using para-hydrogen induced polarization (PHIP).<sup>94</sup> However, to date, no real-time metabolism of the molecule has been demonstrated in vivo due to extremely slow transport into the cell. Furthermore, succinate can induce hypertension in animals when administered intravenously<sup>95</sup>; it is unclear whether this effect occurs in humans and if it does, it may limit clinical applications. However, diethyl succinate is capable of crossing the cell membrane and can also be polarized using the PHIP method. Zacharias *et al.*<sup>96</sup> showed up to three enzymatic conversions of [1-<sup>13</sup>C, 2,3-<sup>2</sup>H]diethyl succinate, namely to succinate, fumarate, and malate in addition to aspartate occurred in vivo. Diethyl succinate is converted to succinate via endogenous esterases before being converted to fumarate (via succinate dehydrogenase) and further into malate (by fumarase). Very recently, [1,4-<sup>13</sup>C]-diethylsuccinate<sup>97</sup> was successfully polarized using dissolution DNP, but in contradiction to the findings of Zacharias *et al.*, no TCA cycle metabolites were observed. This work brought to light the various hurdles of using dialkyl ester analogs as precursors for HP imaging.

### [1-<sup>13</sup>C]-α-Ketoisocaproate

[1-<sup>13</sup>C]-α-ketoisocaproate (KIC) is metabolized to [1-<sup>13</sup>C]leucine by the enzyme branched chain amino acid transferase (BCAT), which is found to be upregulated in some tumors. BCAT is a putative marker for metastasis and a target for the proto-oncogene c-myc. Injection of HP [1-<sup>13</sup>C]KIC into animal models (rodent mammary adenocarcinoma and murine lymphoma xenografts) has shown ample conversion to leucine.<sup>98</sup> In this preclinical study, SNR and contrast were compared between HP [1-<sup>13</sup>C]pyruvate and [1-<sup>13</sup>C]-KIC. [1-<sup>13</sup>C]KIC showed a 2.5 times lower SNR compared to [1-<sup>13</sup>C]pyruvate, whereas the contrast (between tumor and normal tissue) was 20% higher. Very different fluxes through the BCAT catalyzed reaction can be detected in murine lymphoma (EL4) and rat mammary adenocarcinoma (R3230AC) tumors in vivo.<sup>98</sup> KIC is suitable for profiling tumors at the single gene level and as a novel imaging modality for tumors with high BCAT activity. It has also been shown that the biodistribution of KIC metabolism in the brain, especially in the hippocampus and the cortex, can be measured reliably. This work suggests that KIC could be a promising substrate to evaluate BCAT activity in neurodegenerative diseases as it

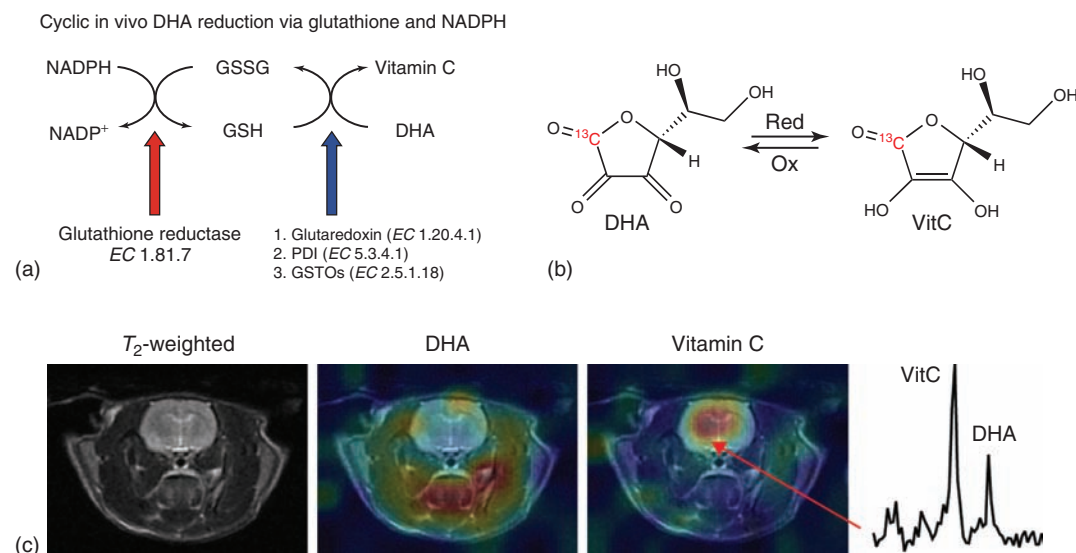


**Figure 3.** Biochemical mechanism, hyperpolarization, and reduction of [1-<sup>13</sup>C]DHA. (a) Relationship between the redox pairs NADPH/NADP, GSSG/GSH, and vitamin C/DHA with associated enzymes. (b) Reversible reduction of labeled DHA to vitamin C (VitC), demonstrating the position of the hyperpolarized carbon. (c) Axial T<sub>2</sub>-weighted images and corresponding color overlays of hyperpolarized DHA and vitamin C signal in a normal rat brain. (Adapted with permission from K. R. Keshari, J. Kurhanewicz, R. Bok, P. E. Z. Larson, D. B. Vigneron, and D. M. Wilson, *Proceedings of the National Academy of Sciences*, 2011, 108, 18606–18611)

is tightly coupled to the glutamate–glutamine shuttle between neurons and astrocytes.<sup>99</sup>

### [1-<sup>13</sup>C]Dehydroascorbic acid (DHA)

Dehydroascorbic acid (DHA) is the reduced form of vitamin C (ascorbic acid, AA) (Figure 3b) and is rapidly transported into cells by the glucose transporter (Glut1). Inside the cells, DHA is converted to AA directly by glutathione (GSH) or glutathione disulfide (GSSH)/NADPH-mediated enzymes<sup>100</sup> (Figure 3a). GSH is responsible for the maintenance and regulation of the redox status of the cell and is implicated in a plethora of diseases including cancer, inflammation, neurodegeneration, aging, and so on.<sup>101</sup> A combination of characteristics of HP [1-<sup>13</sup>C]DHA makes it a particularly viable probe for in vivo studies. These features include its rapid uptake, the relatively large pool size of vitamin C in most cells, the relatively large chemical shift difference between the oxidized and reduced forms (4 ppm), and its relatively long T<sub>1</sub> (≈57 s at 3 T). This probe has been successfully applied to image the redox capacity of both normal organs and tumors in murine models.<sup>102,103</sup>

Keshari *et al.*<sup>103</sup> showed, consistent with prior publications, that the redox capacity as measured by the AA/DHA ratio was highest in the normal brain followed by the liver and then the kidney. Moreover, they showed that there was a significant reduction of [1-<sup>13</sup>C]DHA to [1-<sup>13</sup>C]vitamin C in vivo in TRAMP tumors compared to normal mouse prostates, indicating a higher reducing capacity in tumors. Intracellular redox status is often characterized by the ratio of reduced-to-oxidized GSH/GSSG, and it has been shown that the vitamin C/DHA ratio correlated with the GSH/GSSG ratio in prostate cancer.<sup>103</sup> Figure 3(c) shows the HP AA image overlaid on a T<sub>2</sub>-weighted image of a mouse brain, demonstrating the ability of

DHA to cross the BBB and the very large vitamin C pool size in the normal brain. Two hurdles that must be overcome for this probe to be clinically translatable are (i) potential physiological complications and (ii) inhibition of cellular uptake due to competitive glucose transport.

### <sup>13</sup>C-Choline and <sup>15</sup>N-Choline

Malignant transformation of cells is characterized by increased phosphocholine concentrations, and both <sup>1</sup>H- and <sup>31</sup>P-MRS studies have demonstrated elevated levels of this metabolite in many different forms of tumor compared to normal tissue.<sup>104</sup> <sup>13</sup>C-labeled choline can be polarized but the <sup>13</sup>C T<sub>1</sub>'s are relatively short (4–5 s for the C-2 and C-3) because of dipolar interactions with directly bonded hydrogen atoms. Partial deuteration of the directly attached protons yields a seven- to eightfold increase in T<sub>1</sub> (≈33 s).<sup>105</sup> <sup>15</sup>N-labeled choline can be HP, and because it has a long T<sub>1</sub> (≈4 min) it could make an excellent HP imaging probe.<sup>106</sup> However, the small chemical shift difference between the <sup>15</sup>N resonances of choline and phosphocholine (≈0.2 ppm) makes it difficult to differentiate in vivo at clinical magnetic field strengths. This problem has been addressed by transferring polarization to spin-coupled protons.<sup>107</sup> However there is no evidence that the choline kinase-catalyzed phosphorylation of choline is sufficiently rapid, either in cells in vitro or tumors in vivo, to produce detectable levels of labeled phosphocholine within the lifetime of the polarization.

### Perfusion Measurements Using Hyperpolarized Agents

Mansson *et al.*<sup>21</sup> have reviewed the perfusion and catheter tracking applications of HP <sup>13</sup>C agents, mainly using the Phip technique. The main advantage of using HP <sup>13</sup>C substrates



for perfusion imaging over dynamic susceptibility-based MRI contrast methods is the direct relationship between the signals observed and the agent used. A major hurdle to using HP DNP agents for vascular imaging has been the relatively low spatial resolution of the images relative to other angiographic techniques. Secondly, most of the HP agents did not penetrate the BBB and hence were considered inadequate for measuring cerebral perfusion. However using HP bis-1,1-(hydroxymethyl)-1- $^{13}\text{C}$ -cyclopropane- $\text{D}_8$ , also known as HP001 ( $T_1 = 38\text{ s}$  in vivo at 2.4 T), a rat angiogram<sup>108</sup> and cerebral perfusion measurements were made<sup>109</sup> using a true fast imaging and steady-state precession (trueFISP) pulse sequence that exploits the long  $T_2$  (18 s) of HP001. Nevertheless, HP001 is not an endogenous substance and its safety profile is not completely known.

On the other hand, [ $^{13}\text{C}$ ]urea is an endogenous metabolite and a promising perfusion agent owing to its high achievable polarization, relatively long  $T_1$  (47 s at 3 T), lack of metabolism in most tissues, and excellent safety profile. High-temporal and spatial resolution imaging of HP [ $^{13}\text{C}$ ]urea has been demonstrated using a balanced steady-state free precession (bSSFP) sequence. This approach was used to demonstrate differential perfusion of solid liver tumors (19% reduced core versus 26% increased peripheral tumor perfusion) in a murine model.<sup>73</sup> More recently, von Morze *et al.*<sup>6</sup> used a similar bSSFP approach with a spectral-spatial selective readout to simultaneously image multiple HP perfusion agents with varying structures, permeability, and transport, namely [ $^{13}\text{C}$ ]t-butanol, HP001, and [ $^{13}\text{C}$ ]urea. The goal of that study was to estimate differences in perfusion and permeability in both cancer and normal tissues. They demonstrated that prostate cancer was more permeable to [ $^{13}\text{C}$ ]urea and HP001 than the normal brain or liver, while only [ $^{13}\text{C}$ ]t-butanol rapidly crossed the BBB. Reed *et al.*<sup>110</sup> demonstrated that by replacing the  $^{14}\text{N}$  with  $^{15}\text{N}$  the  $T_2$  of the  $^{13}\text{C}$  labeled carbon of urea could be extended from approximately 0.25 to 11 s.<sup>110</sup> The longer  $T_2$  of [ $^{13}\text{C}$ ,  $^{15}\text{N}$ ]urea was exploited using a bSSFP sequence to acquire high-spatial resolution perfusion images (1 mm in plane) and  $T_2$  maps of the rat kidney. Figure 4 shows the well-resolved renal morphology obtainable using [ $^{13}\text{C}$ ,  $^{15}\text{N}_2$ ]urea and bSSFP fast imaging technique in a rat kidney during diuresis.

## Translation to the Clinic

A decade after the first demonstration of dissolution-DNP by Ardenkjaer-Larsen *et al.*,<sup>26</sup> metabolic imaging using HP [ $1\text{-}^{13}\text{C}$ ]pyruvate was accomplished in prostate cancer patients. Translation of this technology into humans required the development and optimization of the proof-of-concept clinical DNP polarizer in a clean room adjacent to the MR scanner, the implementation of multinuclear MR capabilities on the scanner, the construction of specialized RF coils to detect  $^{13}\text{C}$  nuclei, and developing new MR pulse sequences to efficiently capture the signal. In addition, studies involving preclinical prostate cancer models played an important role in establishing the potential clinical value of HP [ $1\text{-}^{13}\text{C}$ ]pyruvate in prostate cancer. This was critical to obtaining the US Food

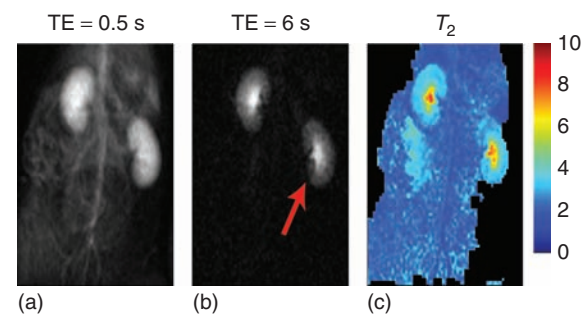


**Figure 4.** Early (a) and late (b) echo coronal projection  $^{13}\text{C}$  images of [ $^{13}\text{C}$ ,  $^{15}\text{N}_2$ ]urea in rats with induced antidiuresis.  $T_2$  map (c). The effects of antidiuresis on the urea image are most evident at the later echo time ( $\text{TR} = 6\text{ s}$ , red arrow), after the short  $T_2$  vascular signal has died away.  $T_2$  mapping provided a quantification of this effect, and clearly resolved the cortical, medullary, and pelvic regions of the kidney

and Drug Administration (FDA) Investigational New Drug (IND) approval for the first human trial.

On the basis of the findings from preclinical studies and pyruvate dose escalation studies in healthy volunteers, an FDA dose escalation phase 1/2a safety and imaging feasibility study was designed. In this trial, a total of 31 patients received an injection of 250 mM HP [ $1\text{-}^{13}\text{C}$ ]pyruvate, followed by  $^{13}\text{C}$  dynamic and fast  $^{13}\text{C}$  MRSI at 3 T. Spatially localized dynamic  $^{13}\text{C}$  spectroscopic imaging monitored delivery, transport, and metabolism of HP [ $1\text{-}^{13}\text{C}$ ]pyruvate. Single time-point 2-D or 3-D acquisitions were used to obtain arrays of  $^{13}\text{C}$  spectra from the prostate and surrounding tissues in 8–12 s. The initial sequence parameters were chosen on the basis of results from preclinical studies in murine and canine models,<sup>26</sup> but were further refined as the study progressed in terms of the start times for acquiring MR data and the flip angle schemes used.

Most important, this first-in-human study showed that injection of HP [ $1\text{-}^{13}\text{C}$ ]pyruvate was safe. This was critical especially given the difference in pharmacologic dose between  $^{13}\text{C}$  HP MR and other metabolic imaging technologies such as PET (the difference between HP [ $1\text{-}^{13}\text{C}$ ]pyruvate and FDG doses is on the order of  $10^7$ ). Specifically, no dose limiting toxicities were observed for the range of doses tested (0.14–0.43 ml/kg). The highest dose of HP pyruvate yielded the best pyruvate and lactate SNR in regions of cancer (mean, range 116, 42–290, and 20.4, 11–46, respectively) and the best contrast for tumor relative to normal prostate (Figure 5).

One- and two-dimensionally localized dynamic HP data showed uptake of HP pyruvate approximately 20 s after injection, with a maximum pyruvate signal at 27 s and a maximum production of lactate at 45 s in cancer, continuing for more than 100 s. This data clearly demonstrated that the  $T_1$  of HP [ $1\text{-}^{13}\text{C}$ ]pyruvate was more than adequate to image uptake and metabolism in the prostate of patients. In addition, the time course of uptake and metabolism corresponded well with prior data from TRAMP<sup>41</sup> and human prostate tissue slice culture studies.<sup>111</sup> Fast 2-D and 3-D based  $^{13}\text{C}$  MRSI data also demonstrated the ability to map the presence and spatial extent of prostate cancer based on elevated HP lactate

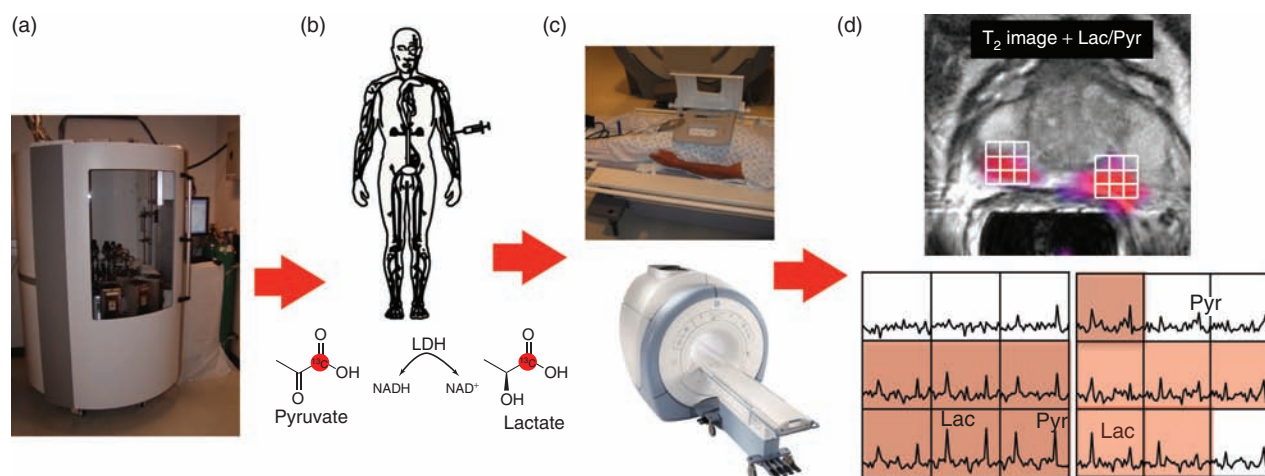


**Figure 5.** Phase 1 clinical trial of hyperpolarized  $[1-^{13}\text{C}]$ pyruvate in patients with prostate cancer. (a) Prepolarization of  $[1-^{13}\text{C}]$ pyruvate using the Spinlab polarizer (GE Healthcare); (b) An i.v. injection of the hyperpolarized  $[1-^{13}\text{C}]$ pyruvate; (c) MR hardware – clinical 3 T scanner and  $^{13}\text{C}$ -enabled clam shell coil; (d) Hyperpolarized lactate images overlaid on  $T_2$  weighted anatomical images, clearly depicting the tumor voxels

(Figure 5). As shown in Figure 5, the first step involved the sterile polarization of HP  $[1-^{13}\text{C}]$ pyruvate and making sure that the  $[1-^{13}\text{C}]$ pyruvate was sufficiently polarized, at physiologic temperature and pH, and that all of the radical was removed prior to i.v. injection administered into a patient (Figure 5b). In the phase 1 trial, this was accomplished with a polarizer in a clean room adjacent to the 3 T MRI scanner used for imaging.

Illustrated in Figure 5(a) is the next generation clinical polarizer that does not require a clean room and therefore greatly reduces the cost of HP  $^{13}\text{C}$  MRI patient studies. As mentioned earlier, the phase 1 trial was critically dependent on having a multinuclear-capable MRI scanner and appropriate  $^{13}\text{C}$  RF coils (Figure 5c). Figure 5(c) shows a  $^{13}\text{C}$  MRSI study performed using the highest  $[1-^{13}\text{C}]$ pyruvate dose from a patient with bilateral biopsy proven prostate cancer. In the phase 1 trial, all patients receiving HP  $^{13}\text{C}$  MRS also received a state-of-the-art multiparametric  $^1\text{H}$  MRI examination for comparison. This included anatomic imaging, diffusion weighted imaging, dynamic contrast-enhanced imaging, and 3-D  $^1\text{H}$  MRSI metabolic imaging. In the case shown in Figure 1(d), the  $^1\text{H}$  multiparametric examination had accurately identified the prostate cancer on the left side of the prostate but missed the cancer on the right side, which was identified by HP  $^{13}\text{C}$  MRI based on elevated HP lactate/pyruvate ratios. Clearly more patient studies will need to be performed with direct pathologic correlation in order to prove the clinical value of HP  $[1-^{13}\text{C}]$ pyruvate imaging in prostate cancer patients; however, the studies in the phase 1 trial remain very encouraging.

When combined with findings from preclinical studies, the results of this first-in-man study suggest that HP  $^{13}\text{C}$  metabolic imaging may be valuable for initial diagnosis and for monitoring therapy. In addition to improved technology for generating and delivering HP agents becoming available, designing new MR data acquisition sequences that use compressed sensing, parallel imaging strategies, and multichannel  $^{13}\text{C}$  RF coils should help advance the translation of these

methods into the clinic. These developments will allow similar methods to be applied to more diverse populations of cancer patients who are undergoing surgical resection or image-directed biopsy.

## Summary

HP  $^{13}\text{C}$  MR has been shown in over 350 published preclinical cell and animal studies and one phase 1 clinical trial, to provide unprecedented information on previously inaccessible aspects of biological processes by detecting nonradioactive, nontoxic  $^{13}\text{C}$ -labeled probes that can monitor enzymatic conversions through key biochemical pathways.<sup>4,7–24</sup> As HP  $^{13}\text{C}$  MR encodes chemical as well as spatial information, this new molecular imaging technique allows the simultaneous detection of multiple biologic compounds and metabolic products with sensitivity enhancements of  $>10\,000$ -fold.<sup>30</sup> This extraordinary new technique, therefore presents the fields of oncology and medical imaging with an opportunity to dramatically improve our ability to investigate human disease and to ultimately translate these techniques into the clinic for more individualized patient care.

HP-DNP technology is becoming increasingly widespread for scientific investigations with over 50 polarizers worldwide including a few custom-built DNP polarizers being used in university-based preclinical research and commercial polarizers available from Oxford Instruments since 2006 for in vitro and animal studies. Also, the recently completed human phase 1 FDA clinical trial has demonstrated the safety and feasibility of HP  $^{13}\text{C}$ -pyruvate MRI in prostate cancer patients.<sup>26</sup> Initial cost estimates are equal to or less than current nuclear medicine imaging methods such as PET, a method that is used clinically for other cancers, but has shown limited utility in detecting changes in glucose uptake and phosphorylation in prostate cancer. HP  $^{13}\text{C}$ -pyruvate MRI can detect dramatically altered conversion to lactate owing to genetic mutations in cancer that result in greatly increased LDH enzymatic activity (Figure 1),



an effect that correlates with cancer grade in an animal model.<sup>55</sup> This molecular imaging technology demonstrated safety and feasibility in a phase 1 clinical trial of prostate cancer, and given its relatively low cost and easily sited hardware, the approach could become a widespread, cost-effective method for assessing cancer aggressiveness and response to therapy.

Future efforts in humans will be driven by new HP probes, improved methods for polarization and delivery of <sup>13</sup>C substrates, MR pulse sequences using sparse sampling techniques, parallel imaging methodologies, and improved coil design. Most important, continued attention to biochemical detail will be needed to establish the clinical value of HP <sup>13</sup>C MRS alongside existing <sup>1</sup>H methods in the multiparametric prostate MR examination, and in comparison to PET.

### Biographical Sketches

Renuka Sriram, PhD works at the Hyperpolarized MRI Technology Resource Center in the Department of Radiology and Biomedical Imaging at the University of California, San Francisco, in Dr Kurhanewicz's Laboratory. Her research focuses on the development and validation of optimally relevant model systems to develop disease-specific hyperpolarized MR biomarkers based on metabolism.

John Kurhanewicz, PhD is a Professor in the Departments of Radiology and Biomedical Imaging, Urology, and Pharmaceutical Chemistry at University of California, San Francisco, and is a member of the California Institute for Quantitative Biology and UCSF Cancer Center, and faculty in the UCSF-UCB Bioengineering Graduate Group. He is the Director of the UCSF Body Imaging Program and the Biomedical NMR lab, and has internationally recognized research programs in cancer imaging, specifically prostate cancer, and the development and clinical translation of new molecular imaging probes and techniques. He has used novel preclinical cell and tissue culture and murine models, and high-field spectroscopic, and MR and PET imaging approaches to identify and translate biomarkers of cancer progression and response to therapy.

Daniel B. Vigneron, PhD is a Professor in the Departments of Radiology and Biomedical Imaging, and Bioengineering and Therapeutic Sciences at the University of California, San Francisco. He is the Director of the UCSF Advanced Imaging Technology Specialized Research Group, Director of the UCSF Hyperpolarized MR Technology Resource Center, and Associate Director of the UCSF Surbeck Laboratory for Advanced Imaging and has extensive expertise in MR instrumentation and technique development. His research focuses on the development of new hardware/software and MR methods to provide enhanced information on metabolism, tissue microstructure, and blood flow in addition to the anatomic information provided by conventional MRI.

### Related Articles

Animal Methods in MRS; Biosynthesis and Metabolic Pathways: Carbon-13 and Nitrogen-15 NMR; Chemical Shift Imaging; Spatial Localization Techniques for Human MRS; Cells and Cell Systems MRS; Dynamic Nuclear Polarization and High-Resolution NMR of Solids; Dynamic Nuclear Polarization: Applications to Liquid-State NMR Spectroscopy; Enzymatic Transformations: Isotope Probes; Hyperpolarized Gas Imaging; Image Formation Methods; Membranes: Carbon-13 NMR; Parahydrogen Enhanced NMR Spectroscopic Methods: A Chemical Perspective; Metabonomics:

NMR Techniques; Multiparametric Magnetic Resonance Imaging of Prostate Cancer at 3T

### References

1. K. Golman, J. H. Ardenaer-Larsen, J. S. Petersson, S. Månsson, and I. Leunbach, *Proc. Natl. Acad. Sci. U. S. A.*, 2003, **100**, 10435.
2. S. J. Kohler, Y. Yen, J. Wolber, A. P. Chen, M. J. Albers, R. Bok, V. Zhang, J. Tropp, S. Nelson, D. B. Vigneron, J. Kurhanewicz, and R. E. Hurd, *Magn. Reson. Med.*, 2007, **58**, 65.
3. C. H. Cunningham, A. P. Chen, M. J. Albers, J. Kurhanewicz, R. E. Hurd, Y. F. Yen, J. M. Pauly, S. J. Nelson, and D. B. Vigneron, *J. Magn. Reson.*, 2007, **187**, 357.
4. R. E. Hurd, Y.-F. Yen, A. Chen, and J. H. Ardenkjaer-Larsen, *J. Magn. Reson. Imaging*, 2012, **36**, 1314.
5. D. M. Wilson, K. R. Keshari, P. E. Z. Larson, A. P. Chen, S. Hu, M. Van Criekinge, R. Bok, S. J. Nelson, J. M. Macdonald, D. B. Vigneron, and J. Kurhanewicz, *J. Magn. Reson.*, 2010, **205**, 141.
6. C.von Morze, R. A. Bok, G. D. Reed, J. H. Ardenkjaer-Larsen, J. Kurhanewicz, and D. B. Vigneron, *Magn. Reson. Med.*, 2013, doi: 10.1002/mrm.25071 per Journal suggestion.
7. C. H. Cunningham, A. P. Chen, M. Lustig, B. A. Hargreaves, J. Lupo, D. Xu, J. Kurhanewicz, R. E. Hurd, J. M. Pauly, S. J. Nelson, and D. B. Vigneron, *J. Magn. Reson.*, 2008, **193**, 139.
8. K. R. Keshari and D. M. Wilson, *Chem. Soc. Rev.*, 2014, **43**, 1627.
9. C. Hilty and S. Bowen, *Org. Biomol. Chem.*, 2010, **8**, 3361.
10. Y.-F. Yen, K. Nagasawa, and T. Nakada, *Magn. Reson. Med. Sci.*, 2011, **10**, 211.
11. F. A. Gallagher, M. I. Kettunen, and K. M. Brindle, *NMR Biomed.*, 2011, **24**, 1006.
12. I. J. Rowland, E. T. Peterson, J. W. Gordon, and S. B. Fain, *Curr. Pharm. Biotechnol.*, 2010, **11**, 709.
13. A. Viale, F. Reineri, D. Santelia, E. Cerutti, S. Ellena, R. Gobetto, and S. Aime, *Q. J. Nucl. Med. Mol. Imaging*, 2009, **53**, 604.
14. K. Golman, R. I. Zandt, M. Lerche, R. Pehrson, and J. H. Ardenkjaer-Larsen, *Cancer Res.*, 2006, **66**, 10855.
15. K. M. Brindle, S. E. Bohndiek, F. A. Gallagher, and M. I. Kettunen, *Magn. Reson. Med.*, 2011, **66**, 505.
16. H. Dafni and S. M. Ronen, *Cancer Biomark.*, 2010, **7**, 189.
17. M. A. Schroeder, K. Clarke, S. Neubauer, and D. J. Tyler, *Circulation*, 2011, **124**, 1580.
18. C. R. Malloy, M. E. Merritt, and A. Dean Sherry, *NMR Biomed.*, 2011, **24**, 973.
19. P. Bhattacharya, B. D. Ross, and R. Bunger, *Exp. Biol. Med. (Maywood)*, 2009, **234**, 1395.
20. B. D. Ross, P. Bhattacharya, S. Wagner, T. Tran, and N. Sailasuta, *Am. J. Neuroradiol.*, 2010, **31**, 24.
21. S. Månsson, E. Johansson, P. Magnusson, C.-M. Chai, G. Hansson, J. S. Petersson, F. Ståhlberg, and K. Golman, *Eur. Radiol.*, 2005, **16**, 57.
22. P. Dutta, G. V. Martinez, and R. J. Gillies, *Biophys. Rev.*, 2013, **5**, 271.
23. K. Brindle, *Br. J. Radiol.*, 2012, **85**, 697.
24. S. J. Nelson, D. Vigneron, J. Kurhanewicz, A. Chen, R. Bok, and R. Hurd, *Appl. Magn. Reson.*, 2008, **34**, 533.
25. J. Kurhanewicz, D. B. Vigneron, K. Brindle, E. Y. Chekmenev, A. Comment, C. H. Cunningham, R. J. Deberardinis, G. G. Green, M. O. Leach, S. S. Rajan, R. R. Rizi, B. D. Ross, W. S. Warren, and C. R. Malloy, *Neoplasia*, 2011, **13**, 81.



26. S. J. Nelson, J. Kurhanewicz, D. B. Vigneron, P. E. Z. Larson, A. L. Harzstark, M. Ferrone, M. Van Criekinge, J. W. Chang, R. Bok, I. Park, G. Reed, L. Carvajal, E. J. Small, P. Munster, V. K. Weinberg, J. H. Ardenkjaer-Larsen, A. P. Chen, R. E. Hurd, L.-I. Odegardstuen, F. J. Robb, J. Tropp, and J. A. Murray, *Sci. Transl. Med.*, 2013, **5**, 198ra108.
27. K. H. Sze, Q. Wu, H. S. Tse, and G. Zhu, *Top. Curr. Chem.*, 2012, **326**, 215.
28. K.-N. Hu, *Solid State Nucl. Magn. Reson.*, 2011, **40**, 31.
29. T. Maly, G. T. Debelouchina, V. S. Bajaj, K.-N. Hu, C.-G. Joo, M. L. Mak Jurkauskas, J. R. Sirigiri, P. C. A. Van Der Wel, J. Herzfeld, R. J. Temkin, and R. G. Griffin, *J. Chem. Phys.*, 2008, **128**, 052211.
30. J. H. Ardenkjaer-Larsen, B. Fridlund, A. Gram, G. Hansson, L. Hansson, M. H. Lerche, R. Servin, M. Thaning, and K. Golman, *Proc. Natl. Acad. Sci.*, 2003, **100**, 10158.
31. A. Abragam and M. Goldman, *Rep. Prog. Phys.*, 1978, **41**, 395.
32. J. H. Ardenkjaer-Larsen, A. M. Leach, N. Clarke, J. Urbahn, D. Anderson, and T. W. Skloss, *NMR Biomed.*, 2011, **24**, 927.
33. S. Hu, P. E. Z. Larson, M. VanCriekinge, A. M. Leach, I. Park, C. Leon, J. Zhou, P. J. Shin, G. Reed, P. Keselman, C.von Morze, H. Yoshihara, R. A. Bok, S. J. Nelson, J. Kurhanewicz, and D. B. Vigneron, *Magn. Reson. Imaging*, 2013, **31**, 490.
34. S. Hu, M. Lustig, A. P. Chen, J. Crane, A. Kerr, D. A. Kelley, R. Hurd, J. Kurhanewicz, S. J. Nelson, J. M. Pauly, and D. B. Vigneron, *J. Magn. Reson.*, 2008, **192**, 258.
35. D. Mayer, Y. F. Yen, J. Tropp, A. Pfefferbaum, R. E. Hurd, and D. M. Spielman, *Magn. Reson. Med.*, 2009, **62**, 557.
36. M. A. Schroeder, L. E. Cochlin, L. C. Heather, K. Clarke, G. K. Radda, and D. J. Tyler, *Proc. Natl. Acad. Sci.*, 2008, **105**, 12051.
37. K. Golman, *Proc. Natl. Acad. Sci.*, 2006, **103**, 11270.
38. K. Golman and J. S. Petersson, *Acad. Radiol.*, 2006, **13**, 932.
39. D. Mayer, Y. S. Levin, R. E. Hurd, G. H. Glover, and D. M. Spielman, *Magn. Reson. Med.*, 2006, **56**, 932.
40. Y. S. Levin, D. Mayer, Y. F. Yen, R. E. Hurd, and D. M. Spielman, *Magn. Reson. Med.*, 2007, **58**, 245.
41. A. P. Chen, M. J. Albers, C. H. Cunningham, S. J. Kohler, Y. F. Yen, R. E. Hurd, J. Tropp, R. Bok, J. M. Pauly, S. J. Nelson, J. Kurhanewicz, and D. B. Vigneron, *Magn. Reson. Med.*, 2007, **58**, 1099.
42. K. Golman, J. S. Petersson, P. Magnusson, E. Johansson, P. Akeson, C. M. Chai, G. Hansson, and S. Månsson, *Magn. Reson. Med.*, 2008, **59**, 1005.
43. P. E. Larson, S. Hu, M. Lustig, A. B. Kerr, S. J. Nelson, J. Kurhanewicz, J. M. Pauly, and D. B. Vigneron, *Magn. Reson. Med.*, 2011, **65**, 610.
44. M. A. Ohliger, P. E. Z. Larson, R. A. Bok, P. Shin, S. Hu, J. Tropp, F. Robb, L. Carvajal, S. J. Nelson, J. Kurhanewicz, and D. B. Vigneron, *J. Magn. Reson. Imaging*, 2013, **38**, 701.
45. P. E. Larson, A. B. Kerr, A. P. Chen, M. S. Lustig, M. L. Zierhut, S. Hu, C. H. Cunningham, J. M. Pauly, J. Kurhanewicz, and D. B. Vigneron, *J. Magn. Reson.*, 2008, **194**, 121.
46. P. E. Larson, R. Bok, A. B. Kerr, M. Lustig, S. Hu, A. P. Chen, S. J. Nelson, J. M. Pauly, J. Kurhanewicz, and D. B. Vigneron, *Magn. Reson. Med.*, 2010, **63**, 582.
47. W. S. Warren, E. Jenista, R. T. Branca, and X. Chen, *Science*, 2009, **323**, 1711.
48. M. H. Levitt, *Annu. Rev. Phys. Chem.*, 2012, **63**, 89.
49. A. Lodi, S. M. Woods, and S. M. Ronen, *NMR Biomed.*, 2013, **26**, 299.
50. K. R. Keshari, R. Sriram, B. Koelsch, M. VanCriekinge, D. M. Wilson, J. Kurhanewicz, and W. Zhen, *Cancer Res.*, 2013, **73**, 529.
51. T. H. Witney, M. I. Kettunen, and K. M. Brindle, *J. Biol. Chem.*, 2011, **286**, 24572.
52. M. I. Kettunen, D.-E. Hu, T. H. Witney, R. McLaughlin, F. A. Gallagher, S. E. Bohndiek, S. E. Day, and K. M. Brindle, *Magn. Reson. Med.*, 2010, **63**, 872.
53. C. Harrison, C. Yang, A. Jindal, R. J. DeBerardinis, M. A. Hooshyar, M. Merritt, A. Dean Sherry, and C. R. Malloy, *NMR Biomed.*, 2012, **25**, 1286.
54. T. Harris, G. Eliyahu, L. Frydman, and H. Degani, *Proc. Natl. Acad. Sci. U. S. A.*, 2009, **106**, 18131.
55. M. J. Albers, R. Bok, A. P. Chen, C. H. Cunningham, M. L. Zierhut, V. Y. Zhang, S. J. Kohler, J. Tropp, R. E. Hurd, Y.-F. Yen, S. J. Nelson, D. B. Vigneron, and J. Kurhanewicz, *Cancer Res.*, 2008, **68**, 8607.
56. P. Lee, W. Leong, T. Tan, M. Lim, W. Han, and G. K. Radda, *Hepatology*, 2013, **57**, 515.
57. M. L. Zierhut, Y.-F. Yen, A. P. Chen, R. Bok, M. J. Albers, V. Zhang, J. Tropp, I. Park, D. B. Vigneron, J. Kurhanewicz, R. E. Hurd, and S. J. Nelson, *J. Magn. Reson.*, 2010, **202**, 85.
58. C. S. Ward, H. S. Venkatesh, M. M. Chaumeil, A. H. Brandes, M. Van-crickinge, H. Dafni, S. Sukumar, S. J. Nelson, D. B. Vigneron, J. Kurhanewicz, C. D. James, D. A. Haas-Kogan, and S. M. Ronen, *Cancer Res.*, 2010, **70**, 1296.
59. D. K. Hill, M. R. Orton, E. Mariotti, J. K. R. Boulton, R. Panek, M. Jafar, H. G. Parkes, Y. Jamin, M. F. Miniotis, N. M. S. Al-Saffar, M. Belouche-Babari, S. P. Robinson, M. O. Leach, Y.-L. Chung, and T. R. Eykyn, *PLoS One*, 2013, **8**, e71996.
60. J. A. M. Bastiaansen, T. Cheng, M. Mishkovsky, J. M. N. Duarte, A. Comment, and R. Gruetter, *Biochim. Biophys. Acta*, 2013, **1830**, 4171.
61. I. Park, P. E. Larson, M. L. Zierhut, S. Hu, R. Bok, T. Ozawa, J. Kurhanewicz, D. B. Vigneron, S. R. Vandenberg, C. D. James, and S. J. Nelson, *Neuro. Oncol.*, 2010, **12**, 133.
62. S. E. Day, M. I. Kettunen, F. A. Gallagher, D.-E. Hu, M. Lerche, J. Wolber, K. Golman, J. H. Ardenkjaer-Larsen, and K. M. Brindle, *Nat. Med.*, 2007, **13**, 1382.
63. A. P. Chen, W. Chu, Y.-P. Gu, and C. H. Cunningham, *PLoS One*, 2013, **8**, e56551.
64. H. Zhang, *Acad. Radiol.*, 2014, **21**, 215.
65. T. H. Witney, M. I. Kettunen, S. E. Day, D. E. Hu, A. A. Neves, F. A. Gallagher, S. M. Fulton, and K. M. Brindle, *Neoplasia*, 2009, **6**, 574.
66. H. Fukuda, K. Kubota, and T. Matsuzawa, *Tohoku J. Exp. Med.*, 2013, **230**, 155.
67. H. Schöder and M. Gönen, *J. Nucl. Med.*, 2007, **48 Suppl 1**, 45.
68. O. J. Rider and D. J. Tyler, *J. Cardiovasc. Magn. Reson.*, 2013, **15**, 93.
69. M. E. Merritt, C. Harrison, C. Storey, A. D. Sherry, and C. R. Malloy, *Magn. Reson. Med.*, 2008, **60**, 1029.
70. M. E. Merritt, C. Harrison, C. Storey, F. M. Jeffrey, A. D. Sherry, and C. R. Malloy, *Proc. Natl. Acad. Sci. U. S. A.*, 2007, **104**, 19773.
71. S. Josan, T. Xu, Y.-F. Yen, R. Hurd, J. Ferreira, C.-H. Chen, D. Mochly-Rosen, A. Pfefferbaum, D. Mayer, and D. Spielman, *NMR Biomed.*, 2013, **26**, 607.
72. J. Ozer, M. Ratner, M. Shaw, W. Bailey, and S. Schomaker, *Toxicology*, 2008, **245**, 194.
73. C.von Morze, P. E. Larson, S. Hu, K. Keshari, D. M. Wilson, J. H. Ardenkjaer-Larsen, A. Goga, R. Bok, J. Kurhanewicz, and D. B. Vigneron, *J. Magn. Reson. Imaging*, 2011, **33**, 692.
74. C. Laustsen, J. A. Østergaard, M. H. Lauritzen, R. Nørregaard, S. Bowen, L. V. Søgaard, A. Flyvbjerg, M. Pedersen, and J. H. Ardenkjaer-Larsen, *Diabetes Metab. Res. Rev.*, 2013, **29**, 125.
75. K. Thind, A. Chen, L. Friesen-Waldner, A. Ouriadov, T. J. Scholl, M. Fox, E. Wong, J. Vandyk, A. Hope, and G. Santyr, *Magn. Reson. Med.*, 2012, **70**, 601.

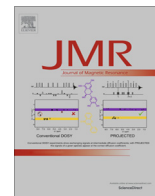
- 1 76. R. E. Hurd, Y. F. Yen, D. Mayer, A. Chen, D. Wilson, S. Kohler, R. Bok, 61
- 2 D. Vigneron, J. Kurhanewicz, J. Tropp, D. Spielman, and A. Pfefferbaum, 62
- 3 *Magn. Reson. Med.*, 2010, **63**, 1137. 63
- 4 77. M. A. Schroeder, H. J. Atherton, D. R. Ball, M. A. Cole, L. C. Heather, J. L. 64
- 5 Griffin, K. Clarke, G. K. Radda, and D. J. Tyler, *FASEB J.*, 2009, **23**, 2529. 65
- 6 78. A. P. Chen, R. E. Hurd, M. A. Schroeder, A. Z. Lau, Y.-P. Gu, W. W. Lam, J. 66
- 7 Barry, J. Tropp, and C. H. Cunningham, *NMR Biomed.*, 2012, **25**, 305. 67
- 8 79. J. M. Park, S. Josan, T. Grafendorfer, Y.-F. Yen, R. E. Hurd, D. M. Spielman, 68
- 9 and D. Mayer, *NMR Biomed.*, 2013, **26**, 1197. 69
- 10 80. F. A. Gallagher, M. I. Kettunen, D. E. Hu, P. R. Jensen, R. I. Zandt, M. 70
- 11 Karlsson, A. Gisselsson, S. K. Nelson, T. H. Witney, S. E. Bohndiek, G. 71
- 12 Hansson, T. Peitersen, M. H. Lerche, and K. M. Brindle, *Proc. Natl. Acad. 72*
- 13 *Sci.*, 2009, **106**, 19801. 73
- 14 81. P. R. Jensen, T. Peitersen, M. Karlsson, R. in 't Zandt, A. Gisselsson, G. 74
- 15 Hansson, S. Meier, and M. H. Lerche, *J. Biol. Chem.*, 2009, **284**, 36077. 75
- 16 82. S. E. Bohndiek, M. I. Kettunen, D.-E. Hu, and K. M. Brindle, *Cancer Res.*, 76
- 17 2012, **72**, 854. 77
- 18 83. M. R. Clatworthy, M. I. Kettunen, D.-E. Hu, R. J. Mathews, T. H. Witney, B. 78
- 19 W. C. Kennedy, S. E. Bohndiek, F. A. Gallagher, L. B. Jarvis, K. G. C. Smith, 79
- 20 and K. M. Brindle, *Proc. Natl. Acad. Sci.*, 2012, **109**, 13374. 80
- 21 84. A. P. Chen, J. Kurhanewicz, R. Bok, D. Xu, D. Joun, V. Zhang, S. J. Nelson, 81
- 22 R. E. Hurd, and D. B. Vigneron, *Magn. Reson. Imaging*, 2008, **26**, 721. 82
- 23 85. D. Mayer, Y.-F. Yen, S. Josan, J. M. Park, A. Pfefferbaum, R. E. Hurd, and 83
- 24 D. M. Spielman, *NMR Biomed.*, 2012, **25**, 1119. 84
- 25 86. J. A. Bastiaansen, H. A. Yoshihara, Y. Takado, R. Gruetter, and A. Comment, 85
- 26 *Metabolomics*, 2014, **10** (5), 986–994. 86
- 27 87. D. Daye and K. E. Wellen, *Semin. Cell Dev. Biol.*, 2012, **23**, 362. 87
- 28 88. F. A. Gallagher, M. I. Kettunen, S. E. Day, M. Lerche, and K. M. Brindle, 88
- 29 *Magn. Reson. Med.*, 2008, **60**, 253. 89
- 30 89. W. Qu, Z. Zha, B. P. Lieberman, A. Mancuso, M. Stetz, R. Rizzi, K. Ploessl, 90
- 31 D. Wise, C. Thompson, and H. F. Kung, *Acad. Radiol.*, 2011, **18**, 932. 91
- 32 90. C. Cabella, M. Karlsson, C. Canapè, G. Catanzaro, S. Colombo Serra, L. 92
- 33 Miragoli, L. Poggi, F. Uggeri, L. Venturi, P. R. Jensen, M. H. Lerche, and F. 93
- 34 Tedoldi, *J. Magn. Reson.*, 2013, **232**, 45. 94
- 35 91. K. R. Keshari, D. M. Wilson, A. P. Chen, R. Bok, P. E. Larson, S. Hu, M. Van 95
- 36 Crieckinge, J. M. Macdonald, D. B. Vigneron, and J. Kurhanewicz, *J. Am. 96*
- 37 *Chem. Soc.*, 2009, **131**, 17591. 97
- 38 92. H. Allouche-Arnon, T. Wade, L. F. Waldner, V. N. Miller, J. M. Gomori, R. 98
- 39 Katz-Brull, and C. A. McKenzie, *Contrast Media Mol. Imaging*, 2013, **8**, 99
- 40 72. 100
- 41 93. T. B. Rodrigues, E. M. Serrao, B. W. C. Kennedy, D.-E. Hu, M. I. Kettunen, 101
- 42 and K. M. Brindle, *Nat. Med.*, 2013, **20**, 93. 102
- 43 103
- 44 104
- 45 105
- 46 106
- 47 107
- 48 108
- 49 109
- 50 110
- 51 111
- 52 112
- 53 113
- 54 114
- 55 115
- 56 116
- 57 117
- 58 118
- 59 119
- 60 120





Contents lists available at ScienceDirect

Journal of Magnetic Resonance

journal homepage: [www.elsevier.com/locate/jmr](http://www.elsevier.com/locate/jmr)

## Dynamic UltraFast 2D EXchange SpectroscopyY (UF-EXSY) of hyperpolarized substrates

Christine Leon Swisher<sup>a,b</sup>, Bertram Koelsch<sup>a,b</sup>, Subramianam Sukumar<sup>a</sup>, Renuka Sriram<sup>a</sup>,  
Romelyn Delos Santos<sup>a</sup>, Zhen Jane Wang<sup>a</sup>, John Kurhanewicz<sup>a,b</sup>, Daniel Vigneron<sup>a,b,\*</sup>, Peder Larson<sup>a,b,\*</sup>

<sup>a</sup> Department of Radiology and Biomedical Imaging, University of California, San Francisco, United States

<sup>b</sup> UC Berkeley-UCSF Graduate Program in Bioengineering, University of California, San Francisco and University of California, Berkeley, United States

### ARTICLE INFO

#### Article history:

Received 24 March 2015

Revised 22 May 2015

Available online 15 June 2015

#### Keyword:

Hyperpolarized

<sup>13</sup>C

EXSY

Stimulated echo

2D NMR

MCT4

Chemical exchange

Ultrafast

### ABSTRACT

In this work, we present a new ultrafast method for acquiring dynamic 2D EXchange SpectroscopyY (EXSY) within a single acquisition. This technique reconstructs two-dimensional EXSY spectra from one-dimensional spectra based on the phase accrual during echo times. The Ultrafast-EXSY acquisition overcomes long acquisition times typically needed to acquire 2D NMR data by utilizing sparsity and phase dependence to dramatically undersample in the indirect time dimension. This allows for the acquisition of the 2D spectrum within a single shot. We have validated this method in simulations and hyperpolarized enzyme assay experiments separating the dehydration of pyruvate and lactate-to-pyruvate conversion. In a renal cell carcinoma cell (RCC) line, bidirectional exchange was observed. This new technique revealed decreased conversion of lactate-to-pyruvate with high expression of monocarboxylate transporter 4 (MCT4), known to correlate with aggressive cancer phenotypes. We also showed feasibility of this technique *in vivo* in a RCC model where bidirectional exchange was observed for pyruvate–lactate, pyruvate–alanine, and pyruvate–hydrate and were resolved in time. Broadly, the technique is well suited to investigate the dynamics of multiple exchange pathways and applicable to hyperpolarized substrates where chemical exchange has shown great promise across a range of disciplines.

© 2015 Elsevier Inc. All rights reserved.

### 1. Introduction

In the fields of chemistry and biology, multidimensional Nuclear Magnetic Resonance (NMR) acquisitions, which differentiate and correlate the resonances arising from individual sites onto multiple frequency axes, are commonly used to study structure, dynamics, reaction states, proteins, the chemical environment of molecules, or any other sample that contains nuclei possessing spin [1–3]. These experiments are intrinsically longer than their conventional one-dimensional (1D) counterparts. In general, 2D NMR techniques are limited by the inherent low sensitivity, resulting in acquisition times on the order of minutes to hours [1]. In carbon-13 NMR, this is particularly pronounced where less than 1% of carbon atoms possess the NMR detectable <sup>13</sup>C isotope. Moreover, SNR suffers from an intrinsically lower gyromagnetic ratio of the <sup>13</sup>C isotope.

\* Corresponding authors at: Byers Hall, Room 102C, 1700 4th St, San Francisco, CA 94158, United States.

E-mail addresses: [Dan.Vigneron@ucsf.edu](mailto:Dan.Vigneron@ucsf.edu) (D. Vigneron), [Peder.Larson@ucsf.edu](mailto:Peder.Larson@ucsf.edu) (P. Larson).

Not surprisingly, there has been an increased interest in using nuclei in the ‘hyperpolarized’ state, whose spin population differences depart significantly from the  $\approx 10^{-5}$  Boltzmann distribution. Dynamic Nuclear Polarization (DNP) yields over a 10,000-fold increase in SNR [2], which is far greater than what can be achieved by multiscan signal averaging. Hyperpolarization with its dramatic increase in sensitivity provides a unique opportunity to probe previously undetectable phenomena via NMR.

Signal detection of hyperpolarized substrates, however, is challenging due to nonrenewable longitudinal magnetization and short-lived signals. These challenges make conventional 2D NMR acquisition strategies incompatible with hyperpolarized substrates. Specifically, conventional acquisitions schemes for multidimensional NMR require an array of scans that are identical to one another aside from the serial incrementing of evolution delays. Given the non-renewable polarization and the shortened acquisition times due to signal decay by  $T_1$ , 2D NMR acquisitions with hyperpolarized substrates requires sequence modifications.

Shapiro and Frydman proposed a method for thermally polarized samples, where the serial indirect domain  $t_1$  encoding of 2D NMR is replaced by a parallelized procedure allowing for different

positions within a sample for inequivalent evolution times [4]. Then Frydman and Blazina extended this method to hyperpolarized substrates [1]. We propose a similar method utilizing their parallelized approach as the foundation for this work. The method presented here differs in several aspects: (1) it uses a symmetric slice selective excitation rather than a gradient acting in combination with a frequency-swept excitation for preparation and (2) it uses dephasing and rephasing gradients rather than an oscillating field gradient. The acquisition and reconstruction presented here relies on principles of phase accrual, which expands on our recently described 1D method Metabolic Activity Decomposition with Simulated Echo Acquisition Mode (MAD-STEAM) [5].

The key advancement presented in this work is its application to dynamic 2D EXchange SpectroscopyY (EXSY) of hyperpolarized carbon-13 substrates, which we show can be used to detect bidirectional exchange. Exchange is particularly important, where both preclinical cell and animal studies of hyperpolarized substrates [6,9], as well as the first-in-man clinical trial [10], have focused heavily on the exchange of hyperpolarized metabolites as markers of disease.

Magnetic Resonance Spectroscopy of hyperpolarized substrates provides a new tool for investigating tissue metabolism and kinetics *in vivo* [11,12]. Previously experiments using MAD-STEAM showed that in addition to increased conversion of pyruvate-to-lactate in tumors, the less studied conversion of lactate-to-pyruvate was significantly smaller in tumors compared to normal tissue with a transgenic model of prostate cancer [13], consistent with a decreased LDH-B expression and increased monocarboxylate transporter 4 (MCT4) and LDH-A expression. However, the rate as measured can be corrupted by alanine-to-pyruvate and hydrate-to-pyruvate conversion, warranting a method to separate these signals to reveal the origin of this change.

Investigation of bidirectional flux and exchange has a number of applications to the metabolism field such as reductive carboxylation [14,15], lipogenesis and its regulation of citrate and  $\alpha$ -ketoglutarate [16], glutamine addiction [17–20], gluconeogenesis, and the isoenzyme composition of LDH. Detection of these pathways has diagnostic and biomedical research potential. For instance, the directionality of reactions within the citric acid cycle has become an area of increased interest as reductive carboxylation has been shown to support tumor growth [14]. However, the signal from hyperpolarized experiments reports only on the bulk spin-exchange and cannot differentiate concomitant spin-exchange. 2D NMR techniques for hyperpolarized substrates could be further used to probe directionality of metabolic pathways. Moreover, 2D NMR could provide improved specificity to cancer metabolism and shed light on exchange and flux of hyperpolarized substrates.

## 2. Theory

### 2.1. Acquisition

Conventional dynamic EXSY acquisition schemes necessitate renewable longitudinal magnetization not available in hyperpolarized substrates. Additionally, conventional EXSY acquisition schemes require many repetitions to obtain the entire indirect spectral dimension (Fig. 1a). The dynamic UF (ultra fast)-EXSY pulse sequence is rapid and does not require renewable longitudinal magnetization making it ideal for hyperpolarized substrates (Fig. 1b). Key features include the symmetric slice selection gradient played with the first 90° RF pulse, gradients blips, which rephase echoes sequentially, and a small flip angle for the final RF pulse, which allows for dynamic acquisition of 2D EXSY spectra. The data can be used to measure build up curves for multiple

species that can be fit to an exchange model for extraction of kinetic rates of interconversion (Fig. 1c and d).

Since the method relies on stimulated echoes with gradient encoding, it is sensitive to motion and diffusion. For diffusion, high  $b$ -values can accelerate signal decay between TMs, shortening the measured T1 relaxation times (“effective T1” times<sup>13</sup>). In this work, we minimized the effect of diffusion by using short, low amplitude gradients, resulting in  $b$ -values  $<10$  s/mm<sup>2</sup>. Bulk motion would result in overall phase shift, however, a <sup>13</sup>C-Urea reference signal can be used to correct for the phase shift (Supplemental Fig. 1). Incoherent motion (e.g. turbulent flow) or non-rigid motion will result in additional unrecoverable signal losses. To prevent these losses in cell experiments, flow through the bioreactor was disabled during the signal acquisition.

This method also assumes spatial homogeneity within the voxel. To limit the effects of this assumption, we limited the number of echoes to the minimum requirement such that the inverse problem is not ill-posed. In the case of HP <sup>13</sup>C<sub>1</sub> pyruvate only 2–3 echoes are required to resolve concomitant exchanging spins. This limits the size of the assumed homogenous region.

### 2.2. Reconstruction

Conventional EXSY reconstruction methods require many  $\tau$  repetitions to reconstruct the 2D spectra. However, by choosing the  $\tau$  repetitions wisely, only a few repetitions can be used to acquire an entire 2D sparse spectra. The UF-EXSY reconstruction, shown in Fig. 2, reconstructs the entire 2D spectra from only a few echoes (Fig. 2) with high spectral resolution in the indirect frequency dimension.

The reconstruction relies on the phase accrual,  $\Delta\phi$ , of exchanging spins with a resonance frequency difference,  $\Delta f$ , at each echo time,  $\tau$ , which has been used to directly observe flux and exchange of a single reaction in real-time [5]. For each frequency,  $f_i$ , with a signal greater than the noise threshold in the direct frequency direction the cross peaks are calculated using the following equation:

$$S(f_1, f_2) = \begin{cases} \frac{\text{Imag}\{S(f_1, f_2)\}}{\sin(2\pi(f_1 - f_2)\tau)}, & f_1 \neq f_2 \\ \text{Re}\{S(f_1, f_2)\} - \sum_i \frac{\text{Imag}\{S(f_1, f_2)\}}{\tan(2\pi(f_1 - f_2)\tau)}, & f_1 = f_2 \end{cases} \quad (1)$$

By using the real and imaginary spectra, the 2D spectra can be reconstructed from a single echo utilizing the phase accrual,  $\Delta\phi$ , between all other frequencies with a signal greater than the noise threshold. However, multiple echo times need to be used to correct for concomitant exchange pathways at a single resonance such that  $\Delta\phi$  varies between the exchange pathways. Additionally it is required that for at least one echo the phase accrual does not equal zero ( $\Delta\phi \neq 0$ ). With these criteria fulfilled, the problem is no longer an ill-posed inverse problem. As the number of echoes increases, the accuracy will increase. To ensure accuracy at least one unique echo is required for each concomitant spin exchange. For instance in the renal cell carcinoma model, UOK262, there are three possible concomitant spin exchanges at pyruvate's resonance, namely lactate-to-pyruvate, hydrate-to-pyruvate, and alanine-to-pyruvate. Because alanine SNR is below the noise threshold, we only need two echoes to accurately reconstruct the data (Fig. 2).

There will be a small loss in SNR at each repetition due to parsing of the signal. Fortunately, much of the original SNR can be recovered. Where the SNR of a cross peak is a function of  $\tau_i$  and is defined by

$$\text{SNR}(\Delta f) = \frac{S}{n\sigma} \left( \frac{1}{\sin(\Delta\phi(\tau_1))} + \frac{1}{\sin(\Delta\phi(\tau_2))} + \dots + \frac{1}{\sin(\Delta\phi(\tau_n))} \right) \quad (2)$$

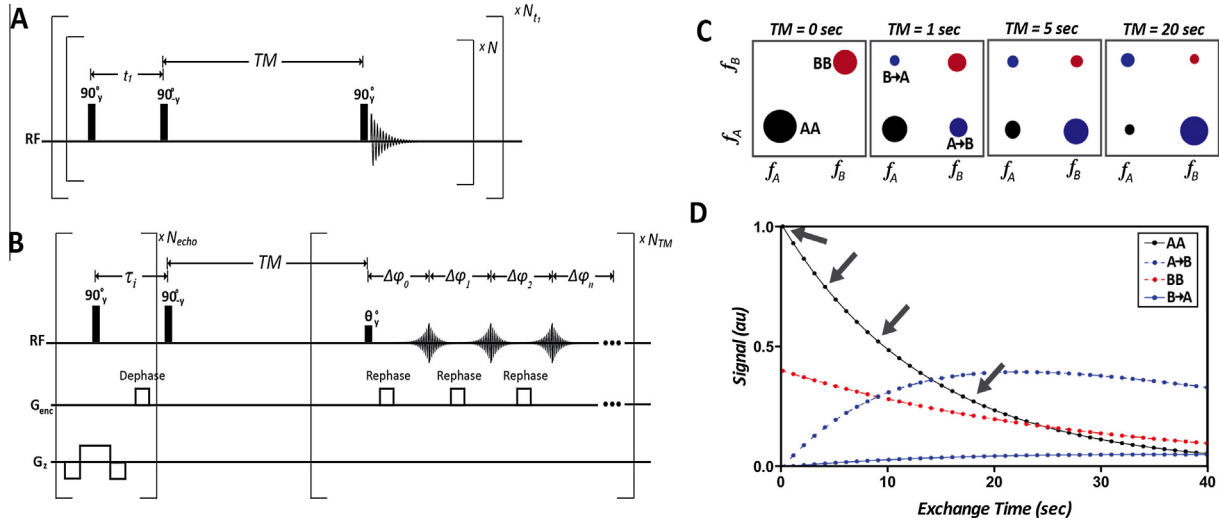


**Fig. 1.** (A) Conventional Dynamic EXchange Spectroscopy (EXSY) requiring renewable longitudinal magnetization not available in hyperpolarized substrates and many repetitions to obtain the entire indirect spectral direction. (B) Dynamic UltraFast EXSY (UF-EXSY) pulse sequence is rapid and does not require renewable longitudinal magnetization making it ideal for hyperpolarized substrates. (C) Schematic of dynamic 2D exchange spectra and (D) simulated build up curves from four measured signal intensities in (c) which can be fit to an exchange model to extract kinetic rates of interconversion. Arrows denote time points shown in 2D spectra (c).

where  $n$  is the number of echoes. As stated previously, to detect a cross peak it is necessary that for at least one echo the phase must not be equal to 0 and  $\pi$  ( $\pm k$  rotations) with sufficient SNR.

More generally, the entire spectra can be described by the following equations:

$$\text{cross peaks} : X = A^{(-1)}a \quad (3)$$

$$\text{diagonal} : Y = b - \sum_f XB \quad (4)$$

where

$$A = \begin{bmatrix} \sin(\varphi_{1,\tau_1}) & \sin(\varphi_{1,\tau_2}) & \cdots \\ \sin(\varphi_{2,\tau_1}) & \sin(\varphi_{2,\tau_2}) & \cdots \\ \vdots & \vdots & \ddots \end{bmatrix} \quad a = \begin{bmatrix} \text{Im}\{S(\tau_1)\} \\ \text{Im}\{S(\tau_2)\} \\ \vdots \end{bmatrix}$$

$$B = \begin{bmatrix} \cos(\varphi_{1,\tau_1}) & \cos(\varphi_{1,\tau_2}) & \cdots \\ \cos(\varphi_{2,\tau_1}) & \cos(\varphi_{2,\tau_2}) & \cdots \\ \vdots & \vdots & \ddots \end{bmatrix} \quad b = \text{Re}\{S(\tau_1)\} + \text{Re}\{S(\tau_1)\} + \cdots \quad (5)$$

Such that the 2D reconstructed spectra can be described by the following equation:

$$\text{2D Spectra} = X + \text{diag}(Y) \quad (6)$$

where

$$X(f_i) = \begin{bmatrix} \text{New}\{S(f_i \rightarrow f_0)\} \\ \text{New}\{S(f_i \rightarrow f_1)\} \\ \vdots \end{bmatrix} \quad (7)$$

and

$$Y(f_i) = \text{Orig}\{S(f_i)\} \quad (8)$$

The reconstruction is summarized in Fig. 2, where selectively sampled FIDs are first reconstructed with 1D Fourier transforms. All frequency locations with an SNR less than the noise

(mean + variance) were set below the threshold. The phase accrual for those frequency locations was automatically determined based on their frequency shift and the dephasing time. Finally, a least squares solution was used to obtain the 2D spectra.

In the case of low SNR not observed in this work, noise amplification can be reduced by choosing echo times based on a priori knowledge of cross peak locations. Additionally, noise amplification could be reduced with Tikhonov Regularization. The UF-EXSY reconstruction workflow used in this work is summarized in Supplemental Fig. 1.

### 3. Methods

#### 3.1. NMR experiments

These studies were conducted on a 14.1T wide-bore microimaging spectrometer equipped with 100 G/cm gradients and a 10 mm broadband probe (Agilent Technologies). The sequence shown in Fig. 1b was acquired with  $\Delta\tau = 8.575$  ms,  $t_{\text{phase}} = 52$   $\mu$ s,  $G_{\text{phase}} = 5$  G/cm,  $t_{\text{crush}} = 10$  ms,  $G_{\text{crush}} = 15$  G/cm,  $N_{\text{echo}} = 3$ ,  $TM = 1$ – $2$  s temporal resolution,  $N_{TM} = 5$ – $20$  repetitions,  $\Delta z = 3$  mm,  $20^\circ$  flip, 64 spectral points, and 4006 Hz bandwidth. Noise was subtracted to remove cross peak artifacts.  $T_2$  signal loss between echoes was small and considered negligible because of the long  $T_2$ s of the hyperpolarized substrates [21]. However, in the case of short  $T_2$ s, signal loss between echoes can be corrected in the reconstruction. The number of echo times acquired was always chosen to equal to or greater than the maximum number of concomitant spin exchanges at a single resonance, typically 2–3 for pyruvate. The NMR signal was pre-processed with a 20 Hz Gaussian spectral apodization window on the symmetric echo and zero order spectral phase correction using HP  $^{13}\text{C}$  Urea as a reference.

#### 3.2. Polarization of $[1-^{13}\text{C}]$ pyruvate and $^{13}\text{C}$ -Urea

$[1-^{13}\text{C}]$ -Pyruvate mixed with the trityl radical OX063 (Tris[8-carboxyl-2,2,6,6-tetra[2-(1-hydroxyethyl)]-benzo(1,2-d:4,5-d)bis(1,3)dithiole-4-yl]methyl sodium salt, Oxford Instruments, Abingdon UK) was hyperpolarized using conventional DNP methods and a HyperSense DNP polarizer (Oxford Instruments, Abingdon, UK) operating at 3.3T and a temperature of 1.3 K. For

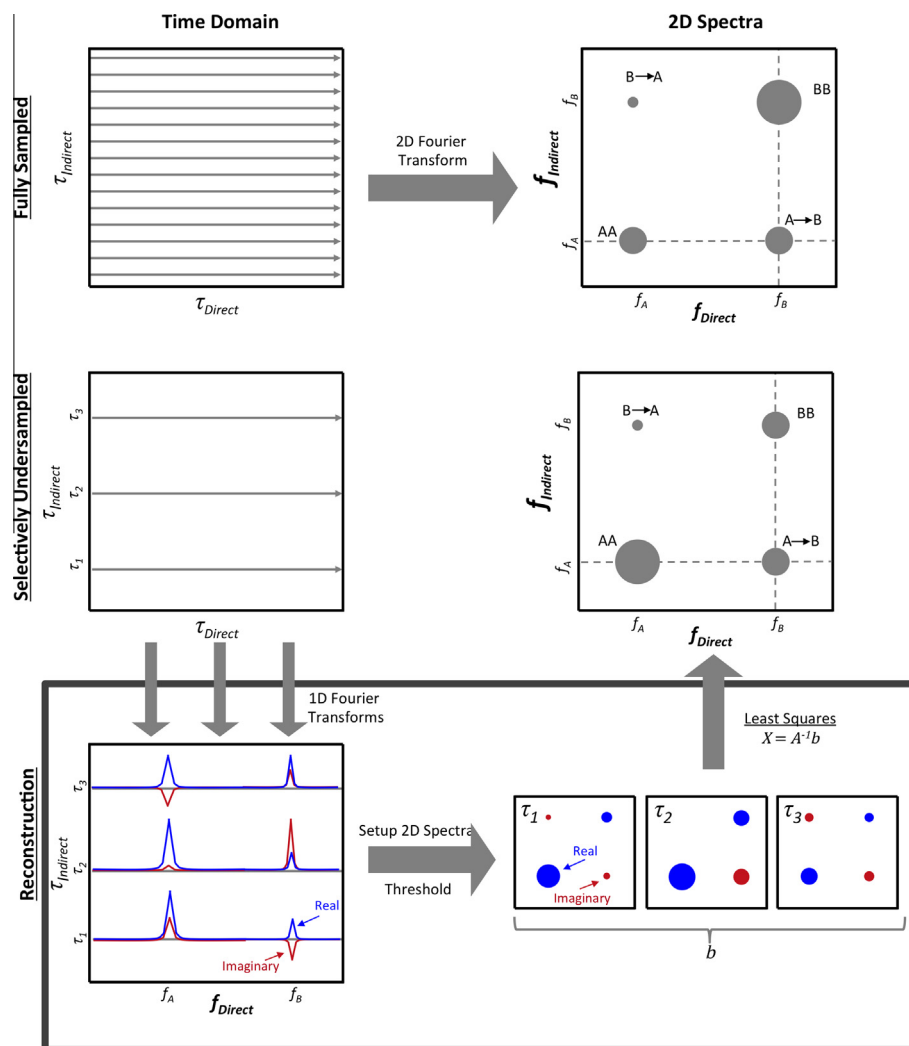


**Fig. 2.** Schematic of Ultra FastEXchange Spectroscopy (UF-EXSY) reconstruction. Using conventional EXSY the 2D spectra can be reconstructed from the magnitude of the 1D spectrum but requires many  $\tau$  repetitions. Using the UF-EXSY reconstruction the entire 2D spectra can be reconstructed from a few echoes with high spectral resolution in the indirect frequency direction equal to that of the direct frequency direction. For each frequency,  $f_i$ , with a signal greater than the noise threshold in the direct frequency direction the cross peaks are calculated using Eq. (6) or with linear least squares based on the phase accrual and frequency difference between every other frequency with a signal also greater than the noise threshold. 2D spectra can be reconstructed from a single acquisition as long as the number of echoes is greater than the number of concomitant exchange pathways at a single resonance.

validations studies,  $[1-^{13}\text{C}]$ -Pyruvate was copolarized [22] with  $^{13}\text{C}$ -urea mixed with the trityl pyruvate OX063. All samples were dissolved to produce solutions with 80 mM pyruvate and 80 mM urea and a biologically appropriate pH ( $\sim 7.4$ ) with TRIS/NaOH/EDTA dissolution media. The microwave power was 20 mW and the frequency was 94.1 GHz.

### 3.3. Cell studies

The UOK262 cell line was derived from a metastasis of a highly aggressive hereditary leiomyomatosis RCC (HLRCC) [18]. As described previously by Keshari et al. [8], cells were grown in Dulbecco's Modified Eagle's Medium (DMEM) with 4.5 g/L glucose and then passaged serially. At passages 2–10 and at 60–80% confluency the cells were used for assays and magnetic resonance experiments. This cell lines was chosen because of its high expression of the monocarboxylate transporter 4 (MCT4), which regulates lactate efflux out of the cell as well as for its high lactate dehydrogenase (LDH) activity [8].

### 3.4. Hyperpolarized $^{13}\text{C}$ magnetic resonance bioreactor experiment

As previously described [7], cells were electrostatically encapsulated into 2.5% w/v alginate microspheres. The microspheres were then loaded into a magnetic resonance-compatible bioreactor and perfused within the bioreactor with DMEM H-21 media at 37 °C maintained 95% air/5%  $\text{CO}_2$ . Prior to and after spectroscopy experiments, media was perfused with a flow rate of 0.5 mL/min. During acquisition, however, the flow was stopped for the duration of the EXSY acquisition (60 s) to prevent metabolites from flowing-out of the bioreactor. 5  $\mu\text{L}$  of the HP dissolution product was injected over 60 s.

### 3.5. LDH validation experiments

A 4.5 mL buffered solution (pH  $\sim 7.4$ ) of HP pyruvate and HP urea (7.5  $\mu\text{L}$  and 15  $\mu\text{L}$ , respectively, of each formulation described previously [5]) was prepared. 15 mg of NADH and 5 mg of LDH (isoenzyme III, isolated from bovine heart, 646 units/mg protein) in 2 mL phosphate buffer solution were added to 2 mL of the HP dissolution product. The solution was mixed vigorously and the

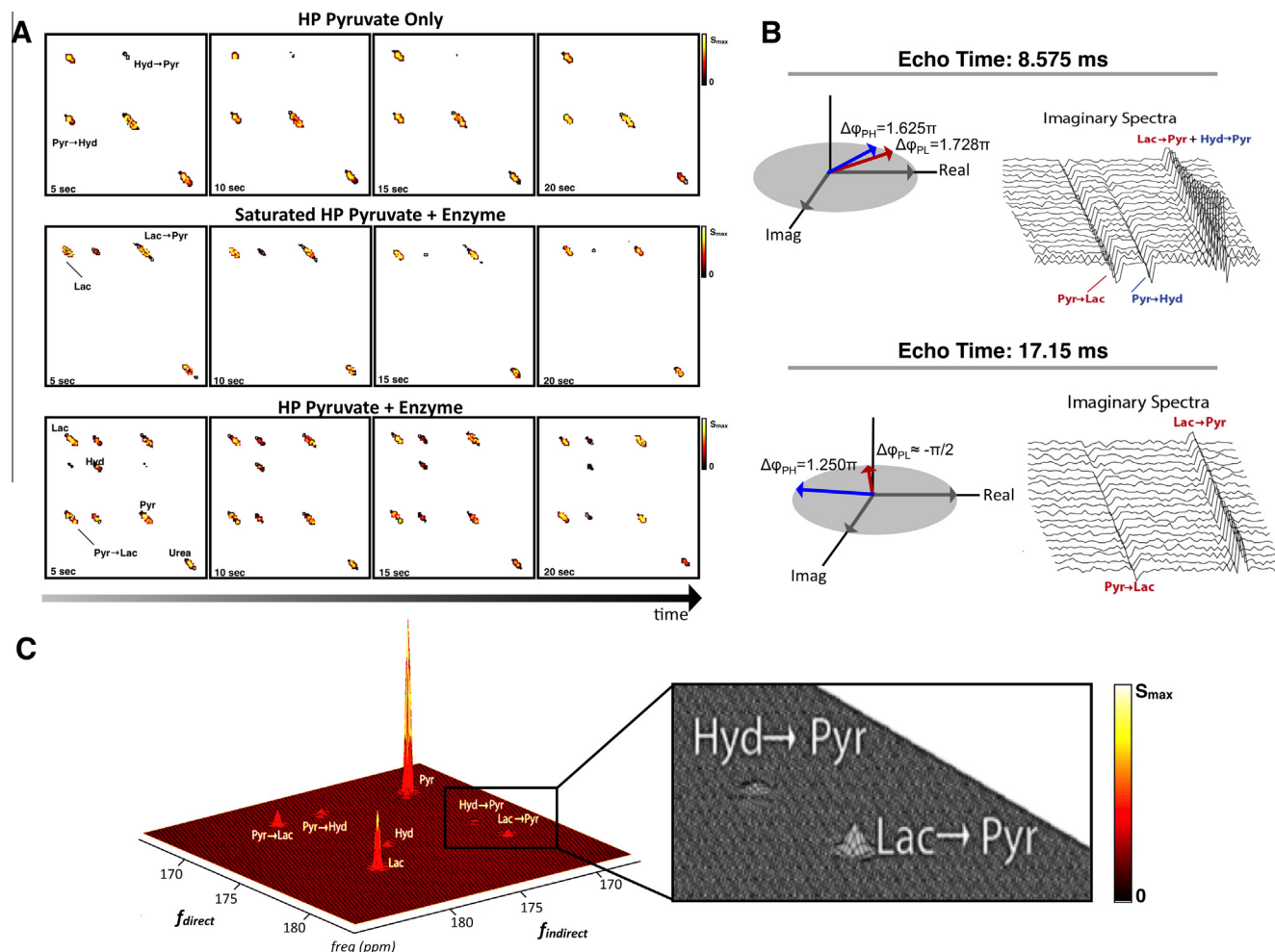


**Fig. 3.** (A) Dynamic EXSY spectra of (top) pyruvate hydration co-polarized with  $^{13}\text{C}$ -urea, (middle) pyruvate conversion to lactate via LDH enzyme and cofactor NADH with and (bottom) without saturation pulses on pyruvate. (B) Validation of phase encoding for multiple echoes. Schematic shows phase dependence of the (left) first and (right) second echo and their corresponding raw dynamic imaginary spectra from UOK262 renal cell carcinoma (RCC) cell-filled alginate microspheres ( $TR = 1$  s) in MR-compatible bioreactor (C) and the 2D spectra (sum of all time points,  $TR = 1$  s,  $N = 20$ ) from the RCC cells.

acquisition was started immediately after. Saturation experiments used a CHESS saturation scheme [5].

### 3.6. MCT4 inhibition

The inhibitor 4,4-diisothiocyanatostilbene-2,2-disulfonate (DIDS) was chosen based on its preference for MCT4 [23]. UF-EXSY experiments with hyperpolarized  $^{13}\text{C}_1$ -Pyruvate were acquired before and 40 min after the administration of 1 mM DIDS in a UOK262 cell line in a bioreactor.

### 3.7. In Vivo

To show feasibility a UOK262 cell line was implanted in the renal capsule of Rag2 immunocompromised mouse. 80 mM HP  $^{13}\text{C}_1$ -Pyruvate and  $^{13}\text{C}$ -Urea buffered solution (pH  $\sim 7.4$ , 300  $\mu\text{L}$  of the HP dissolution product) was injected over 15 s. Acquisition started at 20 s after the start of injection. 8 mm  $\times$  8 mm  $\times$  8 mm voxels were acquired in both the normal and abnormal kidney. The pulse sequence was adapted to be able to select multiple voxels with the addition of slice selection gradients played during the second and third RF pulses (shown in Fig. 5a).

## 4. Results and discussion

### 4.1. Validation

The method was validated with a Bloch simulator (SpinBench, Heartvista, Palo Alto, CA) and with hyperpolarized phantom experiments where the hydration of pyruvate and LDH enzymatic activity were observed dynamically (Fig. 3a). To further validate the technique, pyruvate was saturated after allowing hyperpolarized pyruvate to be converted to hyperpolarized lactate via the LDH enzyme and cofactor NADH (Fig. 3a). As expected, only the conversion of lactate-to-pyruvate was observed.

In Fig. 3b, we show that the expected phase shift matches our actual phase shift in a cell study. Here both forward and backward exchange of pyruvate–lactate and pyruvate–hydrate was resolved (Fig. 3c) and acquired dynamically (Supplemental Fig. 3).

### 4.2. Bidirectional exchange

To investigate the sensitivity of the technique to detect bidirectional exchange, the technique was applied to hyperpolarized pyruvate perfused over renal cell carcinoma (RCC) cell line in a bioreactor to produce 2D EXSY spectra (Fig. 3c). The metastatic RCC cell line (UOK262) was used as a model due to its



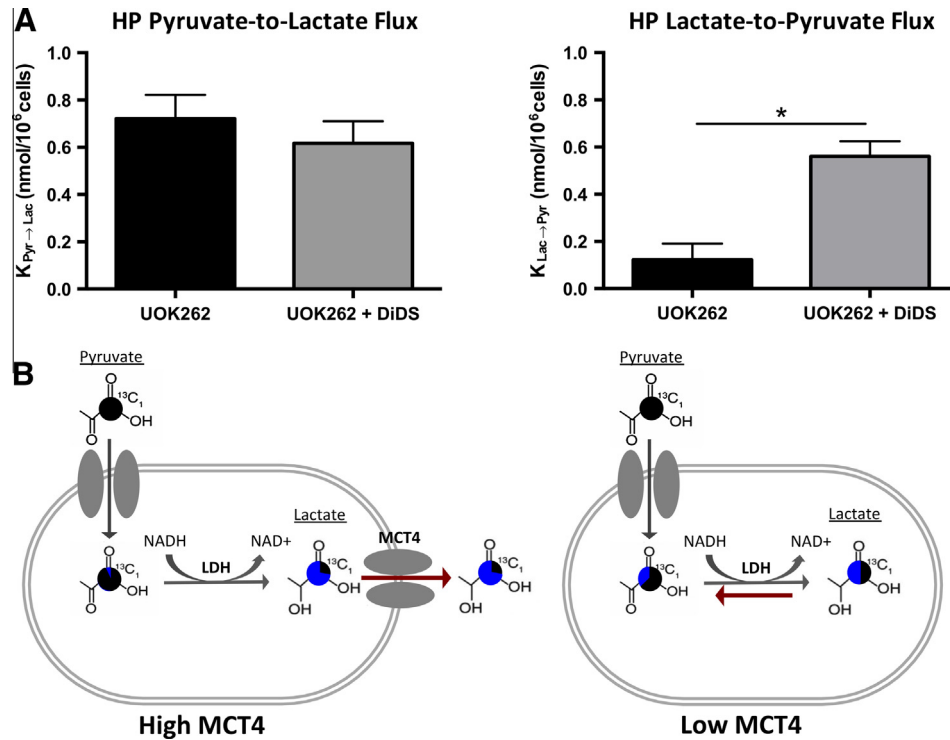


**Fig. 4.** (A) Dynamic UltraFast 2D Exchange Spectroscopy (UF-EXSY) reveals high MCT4 in metastatic renal cell carcinomas and reveals decreased conversion of lactate back to pyruvate with the efflux of lactate out of the cell. All values are reported as mean  $\pm$  SE. \*Denotes significant difference ( $p < 0.05$ ). (B) Schematic of pyruvate and lactate exchange with high and low MCT4. Pie charts demonstrate the proportion of the label that is generated after encoding with “Original” shown in black. (For interpretation of the references to color in this figure legend, the reader is referred to the web version of this article.)

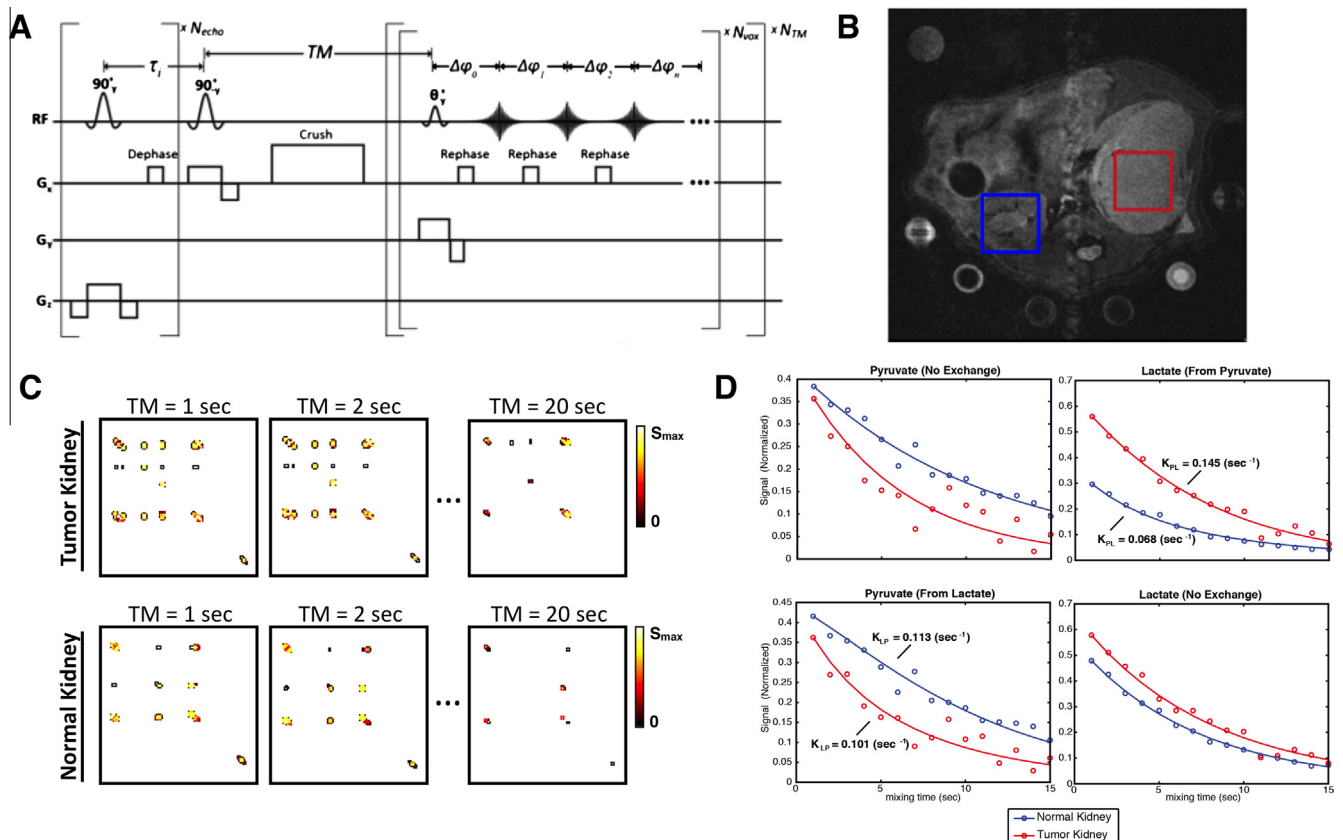


**Fig. 5.** In vivo feasibility (A) Multivoxel pulse sequence for *in vivo* studies. (B) Location of voxels on  $T_2W$  anatomical image. One voxel was acquired in a UOK262 implanted tumor and the other was acquired in the contralateral normal kidney. Both voxels were acquired within a single acquisition. (C) Dynamic 2D spectra data and (D) Dynamic traces with corresponding fitted kinetic parameters show contrast between kidneys.

characteristic elevated expression of MCT4 (Slca16a3), which is known to be indicative of aggressive cancer phenotypes [23–25]. The detection of the activity of a membrane transporter such as MCT4 remains a challenge. We hypothesized that the rate of lactate-to-pyruvate exchange is altered by MCT4 by changing the proximity of lactate to the enzyme as well as altering the intracellular pool size.

#### 4.3. Transport modulates flux

To better isolate the effect of MCT4 on bidirectional exchange, the MCT4 inhibitor, DIDS, was administered in the UOK262 cell line. There was no statistical difference in the flux of HP pyruvate-to-lactate before and after the addition of the selective MCT4 inhibitor (Fig. 4a). However, the inhibitor resulted in a statistically significant increase (95% Confidence Interval, paired students *t*-test) in the conversion of lactate-to-pyruvate conversion (Fig. 4a). The increased observance of lactate-to-pyruvate flux in the DIDS treated UOK262 cells compared to untreated cells, suggests that efflux of lactate is the major deterrent to lactate-to-pyruvate flux in the UOK262 cell line. To explain this result, we hypothesize that pool-size effects modulate flux (Fig. 4b). HP lactate is more likely to be extracellular when MCT4 is highly expressed and less likely to interact with intracellular LDH. However, when MCT4 is reduced, more HP lactate molecules are near LDH and can be converted to pyruvate. Thus we show that bidirectional exchange is modulated by MCT4, a transporter often highly expressed in aggressive cancers [24,25].

Finally, feasibility of the application of the Ultrafast EXSY technique *in vivo* was tested in a single experiment comparing a normal kidney and a kidney in a mouse with implanted UOK262 cell line under the renal capsule (Fig. 5B). Comparing the RCC tumor model kidney to the contralateral normal kidney, we observed increased conversion of HP pyruvate-to-lactate and reduced conversion HP lactate-to-pyruvate, which based on our cell studies, suggests high LDH and high MCT4, respectively (Fig. 5D). However, more experiments are needed to prove this hypothesis. More significantly, this single proof-of-concept study shows that bidirectional exchange can be observed *in vivo* for pyruvate–lactate, pyruvate–alanine, and pyruvate–hydrate and that they can be resolved in time.

## 5. Conclusions

In this work, we present a new UltraFast method for acquiring dynamic 2D EXchange Spectroscopy (UF-EXSY) within a single acquisition using phase accrual. The presented dynamic UF-EXSY pulse sequence is rapid and does not require renewable longitudinal magnetization making it ideal for hyperpolarized substrates. This method overcomes the three main challenges associated with 2D NMR of hyperpolarized substrates: (1) 2D NMR experiments are time intensive, (2) longitudinal magnetization is not renewable, and (3) the signal decays quickly requiring fast acquisition.

Additionally, we show that 2D NMR of hyperpolarized substrates can provide a new tool to probe the directionality of exchange and flux of metabolic pathways. The technique provided insights on the effect of transporters on exchange as well as showed the potential of using bidirectional exchange as a marker of transport. Here we show that bidirectional exchange is modulated by MCT4 in metastatic RCC cell line.

Outside of the field of oncology, the potential applications of this technique are broad including applications such as solvent hydrogen-exchange, protein interactions, protein folding, and conformational changes such as cis-trans isomerizations and domain movements as well as to investigate multistep chemical reactions. More broadly the utilization of phase in 2D NMR acquisitions could

be adapted to quickly acquire sparse 2D spectra for other nuclei such as  $^1\text{H}$ ,  $^{15}\text{N}$ ,  $^{31}\text{P}$ , and  $^{129}\text{Xe}$ .

## Acknowledgments

The authors acknowledge Dr. Kayvan Keshari and Mark Van Criekeing for their development of the bioreactor system as well as Dr. Michael Lustig and Peter Shin for discussions on optimization, Drs. John Pauly and Adam Kerr for discussions on stimulated echoes, and Dr. Christian Frezza for discussions of abnormal cancer metabolism in renal cell carcinomas. The DNP polarizers and related infrastructure were supported by an NIH center Grant (P41EB013598). This study was also supported by NIH Grants R00EB012064 (to PEZL), R01EB016741 (to PEZL) as well as a DOD CA110032 Visionary Post-doctoral Fellowship (to RS).

## Appendix A. Supplementary material

Supplementary data associated with this article can be found, in the online version, at <http://dx.doi.org/10.1016/j.jmr.2015.05.011>.

## References

- [1] L. Frydman, D. Blazina, Ultrafast two-dimensional nuclear magnetic resonance spectroscopy of hyperpolarized solutions, *Nat. Phys.* 3 (2007) 415–419.
- [2] J.H. Ardenkjaer-Larsen, B. Fridlund, A. Gram, G. Hansson, L. Hansson, M.H. Lerche, R. Servin, M. Thaning, K. Golman, Increase in signal-to-noise ratio of >10,000 times in liquid-state NMR, *Proc. Natl. Acad. Sci.* 100 (2003) 10158–10163.
- [3] M. Mishkovsky, L. Frydman, Progress in hyperpolarized ultrafast 2D NMR spectroscopy, *Chem. Phys. Chem.* 9 (2008) 2340–2348.
- [4] B. Shapira, L. Frydman, Arrayed acquisition of 2D exchange NMR spectra within a single scan experiment, *J. Magn. Reson.* 165 (2003) 320–324.
- [5] P.E.Z. Larson, A.B. Kerr, C. Leon Swisher, J.M. Pauly, D.B. Vigneron, A rapid method for direct detection of metabolic conversion and magnetization exchange with application to hyperpolarized substrates, *J. Magn. Reson.* 225 (2012) 71–80.
- [6] T. Harris, G. Eliyahu, L. Frydman, H. Degani, Kinetics of hyperpolarized  $^{13}\text{C}$ -pyruvate transport and metabolism in living human breast cancer cells, *Proc. Natl. Acad. Sci.* 106 (2009) 18131–18136.
- [7] S.E. Day, M.I. Kettunen, M.K. Cherukuri, J.B. Mitchell, M.J. Lizak, H.D. Morris, S. Matsumoto, A.P. Koretsky, K.M. Brindle, Detecting response of rat C6 glioma tumors to radiotherapy using hyperpolarized  $[1-^{13}\text{C}]$ pyruvate and  $^{13}\text{C}$  magnetic resonance spectroscopic imaging, *Magn. Reson. Med.* 65 (2011) 557–563.
- [8] K.R. Keshari, R. Sriram, B.L. Koelsch, M. Van Criekeing, D.M. Wilson, J. Kurhanewicz, Z.J. Wang, Hyperpolarized  $^{13}\text{C}$ -pyruvate magnetic resonance reveals rapid lactate export in metastatic renal cell carcinomas, *Cancer Res.* 73 (2013) 529–538.
- [9] J. Kurhanewicz, D.B. Vigneron, K. Brindle, E.Y. Chekmenev, A. Comment, C.H. Cunningham, R.J. DeBerardinis, G.G. Green, M.O. Leach, S.S. Rajan, R.R. Rizi, B.D. Ross, W.S. Warren, C.R. Malloy, Analysis of cancer metabolism by imaging hyperpolarized nuclei: prospects for translation to clinical research, *Neoplasia* 13 (2011) 81–97.
- [10] S.J. Nelson, J. Kurhanewicz, D.B. Vigneron, P.E. Larson, A.L. Harzstark, M. Ferrone, M. van Criekeing, J.W. Chang, R. Bok, I. Park, G. Reed, L. Carvajal, E.J. Small, P. Munster, V.K. Weinberg, J.H. Ardenkjaer-Larsen, A.P. Chen, R.E. Hurd, L.I. Odegardstuen, F.J. Robb, J. Tropp, J.A. Murray, Metabolic imaging of patients with prostate cancer using hyperpolarized  $[1-^{13}\text{C}]$ pyruvate, *Sci. Transl. Med.* 5 (2013) 198ra108.
- [11] J.M. Park, S. Josan, T. Jang, M. Merchant, Y.F. Yen, R.E. Hurd, L. Recht, D.M. Spielman, D. Mayer, Metabolite kinetics in C6 rat glioma model using magnetic resonance spectroscopic imaging of hyperpolarized  $[1-^{13}\text{C}]$ pyruvate, *Magn. Reson. Med.* 68 (2012) 1886–1893.
- [12] M.L. Zierhut, Y.F. Yen, A.P. Chen, R. Bok, M.J. Albers, V. Zhang, J. Tropp, I. Park, D.B. Vigneron, J. Kurhanewicz, R.E. Hurd, S.J. Nelson, Kinetic modeling of hyperpolarized  $^{13}\text{C}$ -pyruvate metabolism in normal rats and TRAMP mice, *J. Magn. Reson.* 202 (2010) 85–92.
- [13] C. Leon Swisher, P.E. Larson, K. Kruttwig, A.B. Kerr, S. Hu, R.A. Bok, A. Goga, J.M. Pauly, S.J. Nelson, J. Kurhanewicz, D.B. Vigneron, Quantitative measurement of cancer metabolism using stimulated echo hyperpolarized carbon-13 MRS, *Magn. Reson. Med.* 71 (2014) 1–11.
- [14] A.R. Mullen, W.W. Wheaton, E.S. Jin, P.H. Chen, L.B. Sullivan, T. Cheng, Y. Yang, W.M. Linehan, N.S. Chandel, R.J. DeBerardinis, Reductive carboxylation supports growth in tumour cells with defective mitochondria, *Nature* 481 (2012) 385–388.
- [15] A.R. Mullen, Z. Hu, X. Shi, L. Jiang, L.K. Borroughs, Z. Kovacs, R. Boriack, D. Rakheja, L.B. Sullivan, W.M. Linehan, N.S. Chandel, R.J. DeBerardinis, Oxidation



- of alpha-ketoglutarate is required for reductive carboxylation in cancer cells with mitochondrial defects, *Cell Rep.* 7 (2014) 679–690.
- [16] J.A. Menendez, R. Lupu, Fatty acid synthase and the lipogenic phenotype in cancer pathogenesis, *Nat. Rev. Cancer* 7 (2007) 763–777.
- [17] S. Hu, A. Balakrishnan, R.A. Bok, B. Anderton, P.E. Larson, S.J. Nelson, J. Kurhanewicz, D.B. Vigneron, A. Goga,  $^{13}\text{C}$ -pyruvate imaging reveals alterations in glycolysis that precede c-Myc-induced tumor formation and regression, *Cell Metab.* 14 (2011) 131–142.
- [18] C.V. Dang, MYC, microRNAs and glutamine addiction in cancers, *Cell Cycle* 8 (2009) 3243–3245.
- [19] J. Son, C.A. Lyssiotis, H. Ying, X. Wang, S. Hua, M. Ligorio, R.M. Perera, C.R. Ferrone, E. Mullarky, N. Shyh-Chang, Y. Kang, J.B. Fleming, N. Bardeesy, J.M. Asara, M.C. Haigis, R.A. DePinho, L.C. Cantley, A.C. Kimmelman, Glutamine supports pancreatic cancer growth through a KRAS-regulated metabolic pathway, *Nature* 496 (2013) 101–105.
- [20] D.R. Wise, C.B. Thompson, Glutamine addiction: a new therapeutic target in cancer, *Trends Biochem. Sci.* 35 (2010) 427–433.
- [21] G.D. Reed, C. von Morze, R. Bok, B.L. Koelsch, M. Van Criekinge, K.J. Smith, H. Shang, P.E. Larson, J. Kurhanewicz, D.B. Vigneron, High resolution  $(^{13}\text{C})$  MRI with hyperpolarized urea: in vivo  $T(2)$  mapping and  $(^{15}\text{N})$  labeling effects, *IEEE Trans. Med. Imaging* 33 (2014) 362–371.
- [22] D.M. Wilson, K.R. Keshari, P.E. Larson, A.P. Chen, S. Hu, M. Van Criekinge, R. Bok, S.J. Nelson, J.M. Macdonald, D.B. Vigneron, J. Kurhanewicz, Multi-compound polarization by DNP allows simultaneous assessment of multiple enzymatic activities in vivo, *J. Magn. Reson.* 205 (2010) 141–147.
- [23] K.S. Dimmer, B. Friedrich, F. Lang, J.W. Deitmer, S. Broer, The low-affinity monocarboxylate transporter MCT4 is adapted to the export of lactate in highly glycolytic cells, *Biochem. J.* 350 (2000) 219–227.
- [24] Y. Gotanda, Y. Akagi, A. Kawahara, T. Kinugasa, T. Yoshida, Y. Ryu, I. Shiratsuchi, M. Kage, K. Shirouzu, Expression of monocarboxylate transporter (MCT)-4 in colorectal cancer and its role: MCT4 contributes to the growth of colorectal cancer with vascular endothelial growth factor, *Anticancer Res.* 33 (2013) 2941–2947.
- [25] K.S. Lim, A.C. Price, B.A. Orr, C.G. Eberhart, E.E. Bar, Inhibition of monocarboxylate transporter-4 depletes stem-like glioblastoma cells and inhibits HIF transcriptional response in a lactate-independent manner, *Oncogene* 33 (2013) 4433–4441.

# Real-time measurement of hyperpolarized lactate production and efflux as a biomarker of tumor aggressiveness in an MR compatible 3D cell culture bioreactor

Renuka Sriram<sup>a\*</sup>, Mark Van Criekinge<sup>a</sup>, Ailin Hansen<sup>b</sup>, Zhen J. Wang<sup>a</sup>, Daniel B. Vigneron<sup>a</sup>, David M. Wilson<sup>a</sup>, Kayvan R. Keshari<sup>c</sup> and John Kurhanewicz<sup>a</sup>



We have developed a 3D cell/tissue culture bioreactor compatible with hyperpolarized (HP)  $^{13}\text{C}$  MR and interrogated HP  $[1-^{13}\text{C}]$  lactate production and efflux in human renal cell carcinoma (RCC) cells. This platform is capable of resolving intracellular and extracellular HP lactate pools, allowing the kinetic measurement of lactate production and efflux in the context of cancer aggressiveness and response to therapy. HP  $^{13}\text{C}$  MR studies were performed on three immortalized human renal cell lines: HK2, a normal renal proximal tubule cell line from which a majority of RCCs arise, UMRC6, a cell line derived from a localized RCC, and UOK262, an aggressive and metastatic RCC. The intra- ( $\text{Lac}_{\text{in}}$ ) and extracellular ( $\text{Lac}_{\text{ex}}$ ) HP lactate signals were robustly resolved in dynamic  $^{13}\text{C}$  spectra of the cell lines due to a very small but reproducible chemical shift difference ( $0.031 \pm 0.0005$  ppm). Following HP  $[1-^{13}\text{C}]$  pyruvate delivery, the ratio of HP  $\text{Lac}_{\text{in}}/\text{Lac}_{\text{ex}}$  was significantly lower for UOK262 cells compared with both UMRC6 and HK2 cells due to a significant ( $p < 0.05$ ) increase in the  $\text{Lac}_{\text{ex}}$  pool size.  $\text{Lac}_{\text{in}}/\text{Lac}_{\text{ex}}$  correlated with the MCT4 mRNA expression of the cell lines, and inhibition of MCT4 transport using DIDS resulted in a significant reduction in the HP  $\text{Lac}_{\text{ex}}$  pool size. The extension of these studies to living patient-derived RCC tissue slices using HP  $[1,2-^{13}\text{C}_2]$  pyruvate demonstrated a similarly split lactate doublet with a high  $\text{Lac}_{\text{ex}}$  pool fraction; in contrast, only a single NMR resonance is noted for HP  $[5-^{13}\text{C}]$  glutamate, consistent with intracellular localization. These studies support the importance of lactate efflux as a biomarker of cancer aggressiveness and metastatic potential, and the utility of the MR compatible 3D cell/tissue culture bioreactor to study not only cellular metabolism but also transport. Additionally, this platform offers a sophisticated way to follow therapeutic interventions and screen novel therapies that target lactate export. Copyright © 2015 John Wiley & Sons, Ltd.

Additional supporting information may be found in the online version of this article at the publisher's web site.

**Keywords:** hyperpolarized  $^{13}\text{C}$  magnetic resonance (HP  $^{13}\text{C}$  MR); dynamic nuclear polarization (DNP); pyruvate; lactate; aerobic glycolysis; lactate efflux; renal cell carcinoma (RCC); cancer aggressiveness

## INTRODUCTION

There is growing evidence that the upregulation of aerobic glycolysis and lactate production and efflux is an adaptation of cancer cells that aids in survival, growth, and metastasis (1,2). Tumor excretion of lactic acid, combined with poor tumor perfusion, results in an acidic extracellular pH in tumors compared with normal tissue (3). The resulting acidic environment promotes cancer aggressiveness and metastasis by promoting a degradation of the extracellular matrix by proteinases (4,5), increasing angiogenesis through the release of vascular endothelial growth factor (6), and inhibiting the immune response to tumor antigens (7). Extracellular acidification also may render tumors chemoresistant (8). Taken together, these observations suggest that not only increased lactic acid production but also its efflux are important parameters associated with aggressive cancer phenotypes (9,10). Moreover, tumor-specific metabolic shifts, such as increased production and efflux of lactate, can

\* Correspondence to: Dr Renuka Sriram, Radiology and Biomedical Imaging, University of California San Francisco, San Francisco, CA, USA.  
E-mail: renuka.sriram@ucsf.edu

a R. Sriram, M. Van Criekinge, Z. J. Wang, D. B. Vigneron, D. M. Wilson, J. Kurhanewicz  
Radiology and Biomedical Imaging, University of California San Francisco, San Francisco, CA, USA

b A. Hansen  
Norwegian University of Science and Technology, Trondheim, Norway

c K. R. Keshari  
Radiology and Molecular Pharmacology and Chemistry Program, Memorial Sloan Kettering Cancer Center, New York, NY, USA

**Abbreviations used:** HP, hyperpolarized; RCC, renal cell carcinoma; DIDS, 4,4'-diisothiocyanostilbene-2,2'-disulfonic acid; MCT, monocarboxylate transporter; LDH, lactate dehydrogenase;  $\text{Lac}_{\text{in}}$ , intracellular lactate;  $\text{Lac}_{\text{ex}}$ , extracellular lactate; LWHM, line width at half maximum; ERETIC, Electronic Reference to Access In Vivo Concentrations.

potentially be exploited for cancer therapy with minimal impact on normal tissues (3).

Hyperpolarized (HP)  $^{13}\text{C}$  MR is a new molecular imaging technique that allows rapid and noninvasive monitoring of dynamic pathway-specific metabolic and physiologic processes (11). Fast  $^{13}\text{C}$  MR after injection of HP  $[1-^{13}\text{C}]\text{pyruvate}$  has allowed the measurement of increased HP  $[1-^{13}\text{C}]\text{lactate}$  production in both pre-clinical models of cancer (12) and patients with prostate cancer (13). Increased HP  $[1-^{13}\text{C}]\text{pyruvate}$  to lactate conversion has been associated with cancer presence (14) and correlated with increasing cancer aggressiveness/pathologic grade (15). Furthermore, reduced HP  $[1-^{13}\text{C}]\text{lactate}$  early after therapy correlated with therapeutic efficacy (16–19). Current HP  $^{13}\text{C}$  MR approaches have not delineated intracellular and extracellular lactate ( $\text{Lac}_{\text{in}}$  and  $\text{Lac}_{\text{ex}}$  respectively) pools, although recent diffusion-weighted HP  $^{13}\text{C}$  MR approaches have shown the potential to interrogate these two compartments (20–22).

An MR compatible 3D cell/tissue culture bioreactor has been engineered and used to provide a platform to serially monitor the metabolism of viable human cells (23) and tissues (24) in a very controlled environment and with excellent spectral resolution. The bioreactor set-up provides a continuous perfusion of nutrients at a well regulated temperature with adequate oxygen delivery. The use of smaller cell and tissue sample chamber in a 5 mm diameter susceptibility-matched bioreactor design has provided a high mass sensitivity (filling factor) with sufficient  $B_0$  field homogeneity under continuous perfusion conditions for the acquisition of well-resolved serial multinuclear ( $^{31}\text{P}$  and  $^{13}\text{C}$ ) NMR spectra from small numbers of living cells ( $\approx 8$  million) and tissues ( $\approx 60$  mg) (25).

The goal of this study was to determine if the MR compatible 3D culture bioreactor could be used with HP  $^{13}\text{C}$  MR to monitor both the increased cellular production of lactate and its efflux in renal cell carcinoma (RCC), thereby providing a means to test the importance of this process in cancer aggressiveness, metastasis, and response to therapy. To accomplish this, HP  $^{13}\text{C}$  MR studies were performed on three human renal cell lines in the MR compatible 3D cell culture bioreactor: the HK-2 renal proximal tubule cell line (from which most RCCs arise), UMRC6, derived from a localized RCC, and UOK262, established from a highly aggressive metastatic RCC. These cell lines are also known to have differential levels of lactate production and efflux (26). The ability of the bioreactor platform to measure the inhibition of lactic acid efflux using a small molecule monocarboxylate transporter (MCT) inhibitor, DIDS (4,4'-diisothiocyanostilbene-2,2'-disulfonic acid), was also investigated. Lactate is exported out of the cell by the MCTs, predominantly MCT4 (27). DIDS irreversibly and efficiently binds to MCT transporters (an order of magnitude higher affinity for MCT4 than MCT1) and inhibits lactate efflux and to a lesser degree pyruvate uptake (27,28). The studies described in this manuscript demonstrate that intra- and extracellular pools of lactate can be detected and quantified in dynamic (3 s temporal resolution) 1D  $^{13}\text{C}$  MR spectra after injection of HP  $[1-^{13}\text{C}]\text{pyruvate}$ , and that the HP intracellular/extracellular  $[1-^{13}\text{C}]\text{lactate}$  ratio differentiates between localized and metastatic human RCC cells. Further, we have shown that the HP  $\text{Lac}_{\text{in}}/\text{Lac}_{\text{ex}}$  fraction correlates with MCT4 mRNA expression, and the inhibition of lactate efflux with DIDS results in significantly decreased  $\text{Lac}_{\text{ex}}$ .

## MATERIALS AND METHODS

### Cell lines

All three cell lines were grown in monolayers in DMEM (Dulbecco's modified Eagle's medium) with 4.5 g/L glucose media with 10% serum. HK-2 cell line (29) was purchased from ATCC (Manassas, VA, USA). The other two cell lines, UMRC6, and UOK262, were a kind gift from Dr Bart Grossman (MD Anderson Cancer Center, Houston, TX, USA) and Dr W. Marston Linehan (National Cancer Institute, Bethesda, MD, USA) respectively. The UMRC6 cells were derived from a localized human clear cell RCC (30). The UOK262 cells were derived from a metastasis of the highly aggressive hereditary leiomyomatosis RCC (HLRCC).

### MR experiments

As described previously (26), trypsinized cells were prepared for bioreactor MR experiments by electrostatic encapsulation into alginate microspheres. A homogenous mixture of 200–250  $\mu\text{L}$  of cell-laden microspheres (Supplementary Fig. S1) was maintained at physiological conditions by circulating media at 37 °C and supplying 95% air/5%  $\text{CO}_2$  via a gas exchanger in the 5 mm MR compatible bioreactor. A 500 MHz Varian INOVA (Agilent Technologies, Palo Alto, CA, USA) console equipped with a 5 mm, triple-tuned, direct-detect, broadband probe was used for the bioreactor studies. A HyperSense polarizer (Oxford Instruments, Oxford, UK) was used to polarize 14.2 M  $[1-^{13}\text{C}]\text{pyruvate}$  mixed with 15 mM of the trityl radical (GE Health, Menlo Park, CA, USA) and 2.5 mM gadolinium chelate. 16  $\mu\text{mol}$  HP  $[1-^{13}\text{C}]\text{pyruvate}$  was injected into the bioreactor containing the cell-laden microspheres. A 30° flip angle was used to acquire carbon data every 3 s for a total of 5 min. Cell viability was assessed by phosphorus spectra acquired with 2048 averages, repetition time of 2 s and a 90° pulse. The Electronic REference To access In vivo Concentrations (ERETIC) signal (31) was adapted for the phosphorus channel and used to estimate the amount of  $\beta\text{-NTP}$  of cells within the sensitive volume of the RF coil, a more stringent measure of viable cells. The intracellular inorganic phosphate ( $\text{P}_i$ ) peak was resolved from the  $\text{P}_i$  signal arising from the circulating medium for both the UOK262 and the UMRC6 cells. The intracellular pH values of these cells were calculated using the chemical shift of the  $\text{P}_i$  peak, the known pH of the medium ( $7.67 \pm 0.04$  at 37 °C), and published methods (32,33). All bioreactor studies were conducted under the continuous perfusion condition of 0.5 mL/min ( $n = 6$ ), except for the flow modulation experiments when the pump was stopped 15 s after the completion of the HP substrate infusion ( $n = 3$ ). For MCT inhibition studies ( $n = 3$ ), DIDS (disodium salt) was purchased from Molecular Probes (Life Technologies, Foster City, CA, USA) and dissolved in DMSO (dimethyl sulfoxide) to a concentration of 1 mM. It was added via a filter to the medium used to perfuse the cells, after baseline phosphorus and carbon measurements were made.

The rate of lactate accumulation in the media of the UOK262 cells grown in DMEM with 25 mM  $[3-^{13}\text{C}]\text{pyruvate}$  in 2D culture with and without DIDS inhibition was quantified by  $^1\text{H}$  MR spectroscopy ( $n = 3$  each). The media of the UOK262 cells were sampled serially over 8 h. Fully relaxed  $^1\text{H}$  NMR spectra were measured in an 800 MHz Bruker DRX spectrometer (Billerica, MA, USA) equipped with a cryo-cooled 5 mm triple-axis heteronuclear probe, and the  $J$ -coupled  $^{13}\text{C}$  satellite resonance was quantified using ACD/Labs software as described below.

## qRT-PCR

mRNA qRT-PCR was performed as described previously (26) on the total RNA extracted from the cells with an RNeasy purification kit (Qiagen, Valencia, CA, USA). In brief, reverse transcription using an iScript cDNA synthesis kit (Bio-Rad Laboratories, Hercules, CA, USA) was performed and subsequently the cDNA generated was utilized for PCR in triplicate with TaqMan chemistry on the ABI 7900HT (Applied Biosystems, Foster City, CA, USA). Assays for MCT4 were procured from Applied Biosystems. The mRNA expression was calculated relative to the housekeeping gene  $\beta$ -actin.

## Data analysis

The MR data were processed and analyzed using ACD/Labs software (Toronto, Ontario, Canada). The  $\beta$ -NTP peak was quantified in nanomoles from the  $^{31}\text{P}$  spectra by normalizing the integrated peak area against the calibrated ERETIC peak. The  $^{13}\text{C}$  data were processed with (5 Hz) broadening and deconvolved with Lorentzian peak fitting. The HP lactate data (total area under the curve over time) were then normalized to nanomoles of  $\beta$ -NTP, and the pyruvate peak area for comparison across experiments and cell lines. All data are represented as mean  $\pm$  standard error. Student's *t*-test was used to assess the difference between groups. Significant ( $p < 0.05$ ) differences between cell lines are denoted by an asterisk (\*).

## Renal tissue slice bioreactor set-up

Renal tumor tissues were obtained from nephrectomy, sliced into 300  $\mu\text{m}$  thick disks and cultured for 12 h (34). Four slices were placed in the 5 mm MR compatible bioreactor using a specialized construct to hold the tissue in place, and were well perfused in circulating medium at physiological temperature. NMR

data were acquired on a narrow bore 11.7 T Varian INOVA equipped with a 5 mm broadband probe.  $^{31}\text{P}$  spectra were obtained to monitor tissue viability. HP  $^{13}\text{C}$  MR was acquired dynamically (10° pulses, 3 s interval for 300 s) following injection of 1 mL of 4 mM [ $1,2\text{-}^{13}\text{C}_2$ ]pyruvate to assess its metabolism in the renal carcinoma tissue slices.

## RESULTS

### Combining HP $^{13}\text{C}$ MRS with an MR compatible bioreactor provides a measure of the intra-/extracellular compartmentalization of lactate

The custom built 5 mm diameter MR compatible bioreactor allowed the metabolic evaluation of an average of  $40 \pm 7$  million cells with good sensitivity (HP lactate signal to noise ratio ranging from 19 to 216 depending on the cell line) and excellent  $B_0$  field homogeneity (average water line width at half maximum, LWHM, is  $11.37 \pm 0.69$  Hz). These line widths were routinely obtained by gradient shimming along the Z axis followed by manual shimming of the X and Y gradients, which took approximately 15 min. This  $B_0$  field homogeneity was achievable due to the material utilized in the construction of the bioreactor having a similar magnetic susceptibility to that of water, and by ensuring that there were no air interfaces (i.e. air bubbles) within the bioreactor. Figure 1(A) shows a schematic diagram of the 5 mm bioreactor that was optimized for maximal homogeneity and minimal cell culture material requirement. The viability of all three cell lines during the course of the HP MR studies was demonstrated by  $^{31}\text{P}$  NMR spectra acquired before and after each HP [ $1\text{-}^{13}\text{C}$ ]pyruvate injection (Fig. 1(B)). The  $^{31}\text{P}$  spectra were similar to what was previously published for these cell lines (HK-2, UMRC6, and UOK262) (26), and the  $\beta$ -NTP did not change significantly during the time course of the HP studies.  $^{31}\text{P}$  NMR also

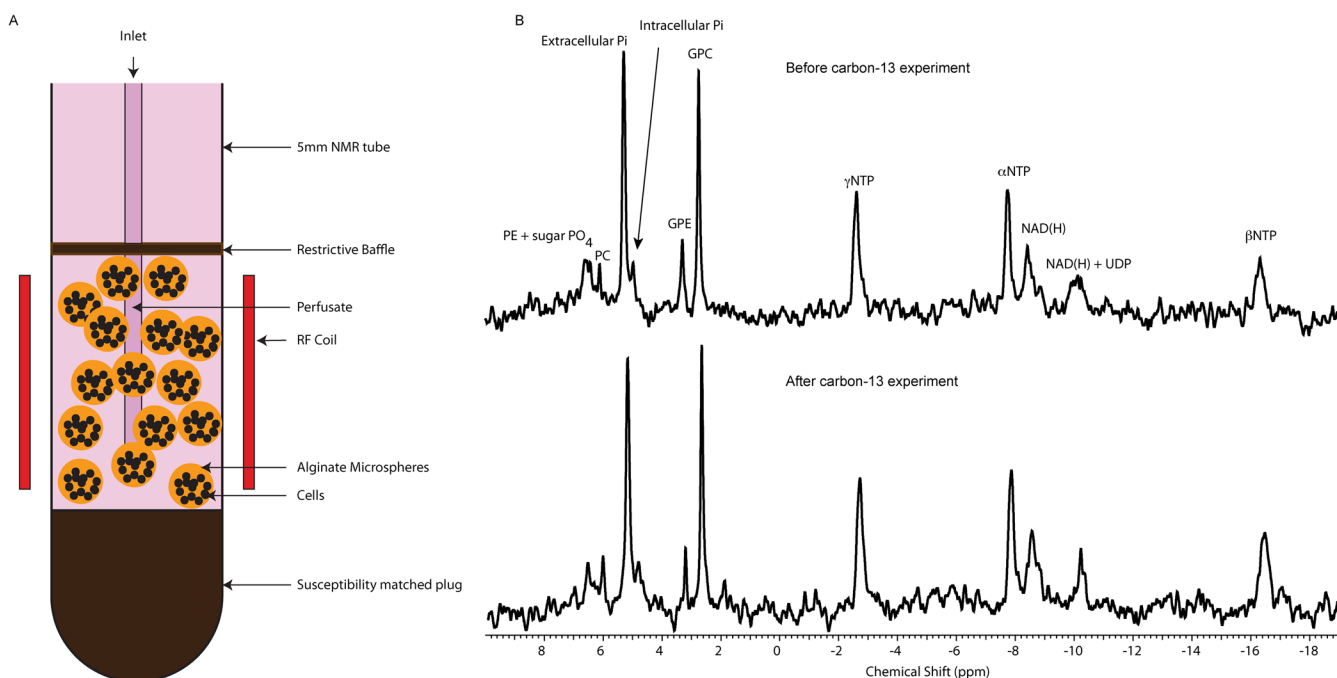


**Figure 1.** Bioreactor set-up and viability assessment. (A) Graphical representation of the 5 mm MR compatible bioreactor optimized for maximal homogeneity. (B) Representative  $^{31}\text{P}$  spectra of showing unaltered bioenergetics of the UOK262 cells under study before and after the HP carbon-13 experiment.

demonstrated similar intracellular pH values of  $7.32 \pm 0.01$  and  $7.33 \pm 0.04$  respectively for UMRC6 and UOK262 RCC cell lines. Unfortunately, the intracellular  $P_i$  peak of the HK-2 cell line could not be spectrally resolved from the media  $P_i$  peak, presumably due to either the more alkaline intracellular pH of this cell line or the inherently low intracellular  $P_i$  levels due to the nonglycolytic nature of these proximal tubular cells (35).

A splitting of the lactate peak was observed for all three renal cell lines (HK-2, UMRC6, and UOK262) studied. Figure 2(A) (top) shows an example of the splitting of the HP  $[1-^{13}\text{C}]$ lactate peak (upfield peak,  $183.13 \pm 0.006$ ; downfield peak,  $183.15 \pm 0.006$  ppm) for the UOK262 cells encapsulated in alginate microspheres at 81 s (time point of maximum  $^{13}\text{C}$  lactate signal) after the injection of HP  $[1-^{13}\text{C}]$ pyruvate into the MR compatible bioreactor. The lower panel in Fig. 2(A) shows the  $^{13}\text{C}$  carbonyl NMR signals from co-polarized HP  $[1-^{13}\text{C}]$ pyruvate and HP  $[1-^{13}\text{C}]$ lactate in perfused alginate microspheres devoid of UOK262 cells. The presence of a single lactate resonance demonstrates that the differences in magnetic field susceptibility of the alginate microsphere microenvironment alone are not responsible for the splitting of the HP lactate peak, and suggests that the resonance at 183.15 ppm corresponds to the  $\text{Lac}_{\text{ex}}$  pool. The assignment of the downfield 183.15 resonance as arising from the  $\text{Lac}_{\text{ex}}$  pool was also supported by peak line-width measurements. The LWHM for the upfield lactate resonance ( $4.3 \pm 0.1$  Hz) was significantly larger than the downfield resonance ( $2.5 \pm 0.07$  Hz), which was similar to the LWHM observed for lactate in the alginate beads without the presence of cells ( $2.18 \pm 0.05$  Hz). Based

on these findings, we initially assigned the up- and downfield lactate resonances as arising from  $\text{Lac}_{\text{in}}$  and  $\text{Lac}_{\text{ex}}$  pools. The difference in chemical shift ( $3.92 \pm 0.06$  Hz) of the  $\text{Lac}_{\text{in}}$  and  $\text{Lac}_{\text{ex}}$  resonances was reproducible within the same study as well as between studies. Although the  $\text{Lac}_{\text{in}}$  and  $\text{Lac}_{\text{ex}}$  resonances were not baseline resolved, the resonances were sufficiently separated to be accurately fit to two Lorentzian line shapes (Fig. 2(B)).

Several studies were performed to modulate the  $\text{Lac}_{\text{ex}}$  and  $\text{Lac}_{\text{in}}$  pools in order to confirm the chemical shift of the corresponding lactate resonances. These studies included (a) increasing cell density within the bioreactor in order to increase  $\text{Lac}_{\text{in}}$ , (b) inhibiting the efflux of lactate in order to decrease  $\text{Lac}_{\text{ex}}$ , (c) stopping media flow during the HP MR study in order to increase  $\text{Lac}_{\text{ex}}$ , and (d) quantifying the amount of non-HP lactate in the medium to correlate with extracellular HP lactate measurements. The results of these validation studies are provided below. Although leakage of lactate dehydrogenase (LDH) from a small number of dead cells in the bioreactor is possible, this leakage did not result in a significant LDH concentration in the media (Supplementary Fig. 2) and therefore did not confound the interpretation of the  $\text{Lac}_{\text{ex}}$  pool.

In Fig. 2(C), a linear increase in  $\text{Lac}_{\text{in}}$  resonance was demonstrated as UOK262 cell density in the bioreactor was increased. In these studies, the cell density of viable UOK262 cells within the sensitive volume of the MR coil was calculated based on the  $\beta$ -NTP resonance in the  $^{31}\text{P}$  spectra using the value of  $18.6 \pm 1.5$  fmol of ATP (adenosine triphosphate)/cell previously determined for the UOK262 cell line (26).

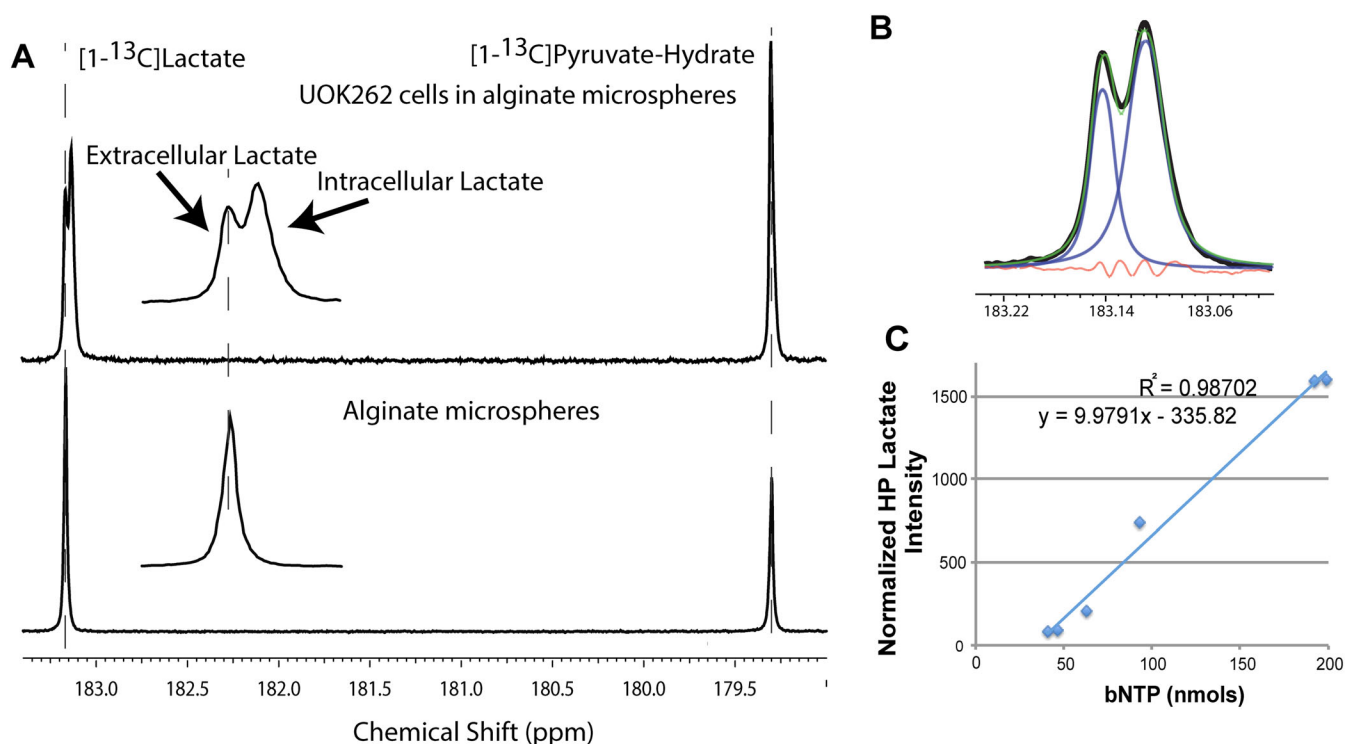


**Figure 2.** Differential compartmentalization of HP  $[1-^{13}\text{C}]$ lactate. (A) The lower panel shows the spectrum in alginate microspheres devoid of cells, infused with co-polarized  $[1-^{13}\text{C}]$ lactate and  $[1-^{13}\text{C}]$ pyruvate. Only one peak was observed for the  $[1-^{13}\text{C}]$ lactate signal, while two peaks were observed in the alginate microspheres with UOK262 cells when infused with HP  $[1-^{13}\text{C}]$ pyruvate (upper panel). The inset (2.5 $\times$ ) clearly shows the well-resolved peaks of lactate, where the chemical shift of the downfield peak coincides with that of the signal of lactate in empty alginate microspheres. (B) Lorentzian decomposition of the two peaks clearly reveals the wider line width of the  $\text{Lac}_{\text{in}}$  peak compared with the  $\text{Lac}_{\text{ex}}$  peak (downfield). (C) Plot of  $\text{Lac}_{\text{in}}$  (blue diamonds) as a function of cell density. The x axis represents the  $\beta$ -NTP concentration, which was used to quantify the viable UOK262 cells within the sensitive coil of the bioreactor.



Figure 3(A) shows representative  $^{13}\text{C}$  NMR spectra of HP  $[1-^{13}\text{C}]$ lactate acquired from untreated (top) and DIDS treated (bottom) UOK262 cells (bottom) taken at the time of maximum lactate production after injection of HP pyruvate (dotted line in Fig. 3(B)). The corresponding plots of the dynamic (every 3 s) intra- and extracellular  $[1-^{13}\text{C}]$ lactate spectra before and after DIDS treatment are shown in Fig. 3(B). There is a clear visual reduction in the extracellular HP lactate peak in the treated spectra and an associated reduction in the area under the curve for extracellular HP lactate of the treated versus untreated UOK262 cells. Figure 3(C) (solid bar) quantitatively shows that there is a  $64 \pm 15\%$  increase in the  $\text{Lac}_{\text{in}}/\text{Lac}_{\text{ex}}$  pool ratio when lactate efflux is inhibited by DIDS. With DIDS inhibition, the total HP  $[1-^{13}\text{C}]$ lactate pool also decreased by  $57 \pm 11\%$  relative to untreated cells due to the inhibition of pyruvate uptake by DIDS inhibition of MCT1. This confounding change in total HP  $[1-^{13}\text{C}]$ lactate pool size with DIDS inhibition is eliminated by taking the  $\text{Lac}_{\text{in}}/\text{Lac}_{\text{ex}}$  ratio, which clearly demonstrates a much larger impact on the  $\text{Lac}_{\text{ex}}$  pool, consistent with the higher affinity of DIDS for MCT4 as compared with MCT1 (27).

Subsequently, we compared the dynamic  $^{13}\text{C}$  NMR spectra of HP  $[1-^{13}\text{C}]$ lactate acquired from UOK262 cells using a normal constant medium flow rate (0.5 mL/min) with those acquired when flow was stopped 15 s after the infusion of HP  $[1-^{13}\text{C}]$ pyruvate. 15 s was the time required for the bolus of pyruvate to arrive in the cellular compartment of the bioreactor. Figure 3(C) shows that the  $\text{Lac}_{\text{in}}/\text{Lac}_{\text{ex}}$  peak area ratio was reduced by  $34 \pm 6\%$  ( $p = 0.055$ ) under stop-flow conditions relative to the constant media flow condition. The decrease in the  $\text{Lac}_{\text{in}}/\text{Lac}_{\text{ex}}$  ratio was due to an increase in the  $\text{Lac}_{\text{ex}}$  peak area ( $164 \pm 74\%$  of control) since it was no longer flowing out of the sensitive volume of the NMR coil, while the  $\text{Lac}_{\text{in}}$  peak remained relatively constant ( $102 \pm 46\%$  of

control). Under stop-flow conditions, the total HP  $[1-^{13}\text{C}]$ lactate pool increased by  $29 \pm 58\%$  relative to the same cells under normal flow conditions, presumably due to the increased time that the  $[1-^{13}\text{C}]$ pyruvate bolus was exposed to the cells, leading to increased uptake and conversion to lactate. This confounding increase in total HP  $[1-^{13}\text{C}]$ lactate pool size was eliminated by using the  $\text{Lac}_{\text{in}}/\text{Lac}_{\text{ex}}$  ratio.

Stopping the media flow did not have an impact on the viability of the UOK262 cells as determined by the stable  $\beta\text{-NTP}$  peak area in  $^{31}\text{P}$  spectra acquired before and after the stoppage of medium flow. The efflux of lactate and its associated proton into the media during this period of no flow resulted in a transient reduction in extracellular pH ( $\leq 6.8$ ), as observed by the “yellowing” of the phenol red indicator in the media. This media was equilibrated with fresh media flowing into the cell-containing chamber, soon after the flow was turned on at the end of the HP experiment, with the media pH returning to 7.6. There was no difference in the resonance frequency of the  $\text{Lac}_{\text{ex}}$  during this transient change in pH, suggesting that the downfield shift of  $\text{Lac}_{\text{ex}}$  was not due to a more acidic extracellular pH. This is also supported by the finding that the  $^{13}\text{C}$  chemical shift of the carbonyl resonance of lactate decreased rather than increased with decreasing pH (0.015 ppm upfield shift going from pH 7.4 to 6.9).

Finally, for UOK262 cells grown in  $[3-^{13}\text{C}]$ pyruvate containing media the rate of extracellular  $[3-^{13}\text{C}]$ lactate accumulation in 2D culture was sampled serially over 8 h and quantified by measuring the  $^{13}\text{C}$  satellites of the lactate methyl protons in 800 MHz  $^1\text{H}$  MR spectra. Figure 4 shows a plot of  $[3-^{13}\text{C}]$ lactate accumulation in the medium over time for untreated and DIDS treated UOK262 cells. Fitting these data demonstrated a lactate efflux of 1.34 nmol/min/million

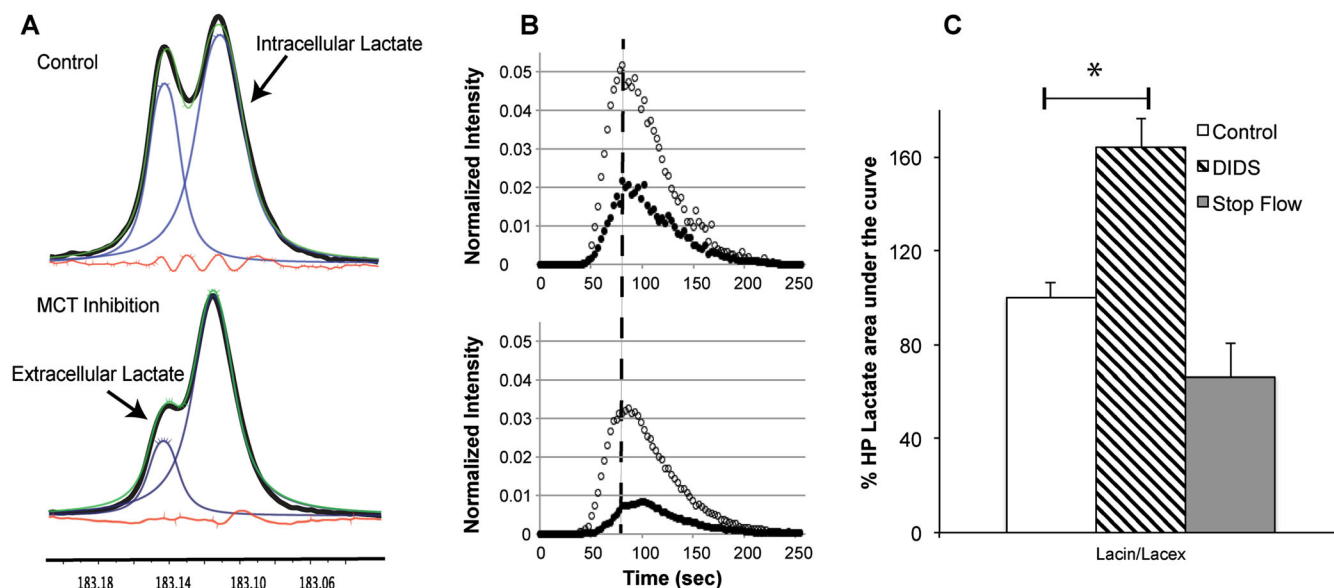


**Figure 3.** Differential modulation of the lactate pools. (A) Representative  $^{13}\text{C}$  MR spectra of HP  $[1-^{13}\text{C}]$ lactate acquired from untreated (top) and DIDS treated (bottom) UOK262 cells acquired at the time of maximal lactate production (indicated by the dashed line in B). (B) Dynamic measurement of HP  $\text{Lac}_{\text{ex}}$  (filled circles) and  $\text{Lac}_{\text{in}}$  (open circles) without (top panel) and with DIDS treatment (bottom panel). (C) Bar graph of the HP  $[1-^{13}\text{C}]$ lactate peaks of UOK262 cells under different flow and treatment conditions relative to control (flow at 0.5 mL/min) normalized to 100%. The bar filled with black slanted lines represents the  $\text{Lac}_{\text{in}}/\text{Lac}_{\text{ex}}$  ratio of UOK262 cells pretreated with DIDS inhibitor for 45 min ( $n = 3$ ). The change in the ratio is significantly different ( $p = 0.016$ ). The grey bar denotes the  $\text{Lac}_{\text{in}}/\text{Lac}_{\text{ex}}$  measurements after flow was stopped 15 s post HP  $[1-^{13}\text{C}]$ pyruvate infusion for a period of 4.25 min ( $n = 3$ ) and has a  $p$  value of 0.055 as measured by Student's  $t$  test when compared with control.

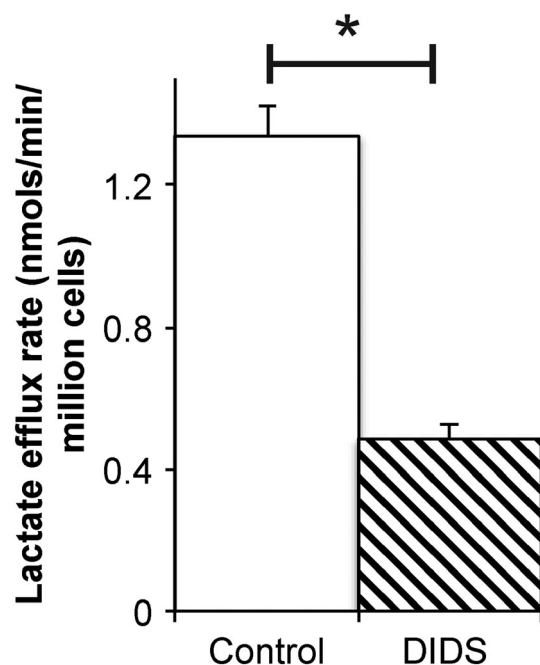


**Figure 4.** Rate of lactate efflux inhibition of UOK262 cells using non-HP MR measurements. Bar graph of  $[3\text{-}^{13}\text{C}]$ lactate efflux rate of untreated ( $n = 3$ ) and DIDS treated (slanted lines,  $n = 3$ ) UOK262 cells grown in  $[3\text{-}^{13}\text{C}]$ pyruvate containing media. The significantly decreased efflux rate ( $p \leq 0.05$ ) with DIDS treatment relative to the untreated controls is consistent with hindered lactate efflux due to MCT4 inhibition.

cells for the untreated UOK262 cells. In the presence of DIDS, the rate of lactate efflux was reduced by 64% to 0.48 nmol/min/million cells. This reduction in lactate efflux was similar to that observed with integrated HP  $\text{Lac}_{\text{in}}/\text{Lac}_{\text{ex}}$  signal intensity (total area under the curve over time) after treatment with DIDS (Fig. 3(B)).

Taken together, the results of these studies clearly demonstrate that the up- and downfield HP  $[1\text{-}^{13}\text{C}]$ lactate resonances were due to the intra- and extracellular pools of lactate.

### HP intracellular to extracellular $[1\text{-}^{13}\text{C}]$ lactate ratio differentiates the varying aggressiveness of RCC cells

HP  $^{13}\text{C}$  MR studies were performed on three renal cell lines, ranging from normal renal tubule cells (HK-2) through localized RCCs (UMRC6) to metastatic RCCs (UOK262). These cell lines were selected since they demonstrate varying  $\text{Lac}_{\text{in}}$  and  $\text{Lac}_{\text{ex}}$  pool sizes due to their known differential MCT1, MCT4, and LDHA mRNA expression and LDH activity (26). HP  $^{13}\text{C}$  MR studies demonstrated significantly different  $\text{Lac}_{\text{in}}/\text{Lac}_{\text{ex}}$  ratios for the three cell lines. The bar graph in Fig. 5(A) shows that the  $\text{Lac}_{\text{in}}/\text{Lac}_{\text{ex}}$  ratio in UOK262 cells is significantly lower than that of UMRC6 as well as HK-2 cells by more than two- and 2.5-fold. This is due to a significant increase in the HP extracellular  $^{13}\text{C}$  lactate fraction, which comprises  $38 \pm 5\%$  of the total  $^{13}\text{C}$  lactate pool in UOK262 cells, and was significantly greater than that for UMRC6 and HK-2 cells, at  $23 \pm 4\%$  and  $17 \pm 1\%$ , respectively. MCT4 mRNA expression ( $p < 0.05$ ) was significantly elevated in the UOK262 cells compared with the other cell lines (HK-2  $p = 0.0011$ , UMRC6  $p = 0.0171$ ), and Fig. 5(B) shows a negative linear correlation ( $R^2$  of 0.997) of MCT4 mRNA expression and HP  $\text{Lac}_{\text{in}}/\text{Lac}_{\text{ex}}$  ratio for the three cell lines.

### Measurement of $\text{Lac}_{\text{in}}$ and $\text{Lac}_{\text{ex}}$ in living human renal tissue slices

The ability of this approach to measure  $\text{Lac}_{\text{in}}$  and  $\text{Lac}_{\text{ex}}$  was extended to living patient-derived renal tissue slices in the 5 mm MR compatible bioreactor. Five slices with approximately 88 mg of tissue (wet weight) from high-grade urothelial carcinoma were used for this study. Tissue viability, monitored using  $^{31}\text{P}$ , was maintained for the duration of the study (4.5 h). Figure 6 shows the  $^{13}\text{C}$  spectrum of the living human tissue slice cultures in the 5 mm bioreactor, after injection of HP  $[1,2\text{-}^{13}\text{C}_2]$ pyruvate. Flux to both HP  $[1,2\text{-}^{13}\text{C}_2]$ lactate and  $[5\text{-}^{13}\text{C}]$ glutamate was observed. Similar to renal cancer cell lines, the lactate doublet (centered at 183.1 ppm) was split by the intra- and extracellular micro-environment, with  $\text{Lac}_{\text{ex}}$  resonating 3.92 Hz downfield of the intracellular pool, while only a singlet denoting the intracellular compartment was observed for the  $[5\text{-}^{13}\text{C}]$ glutamate. The

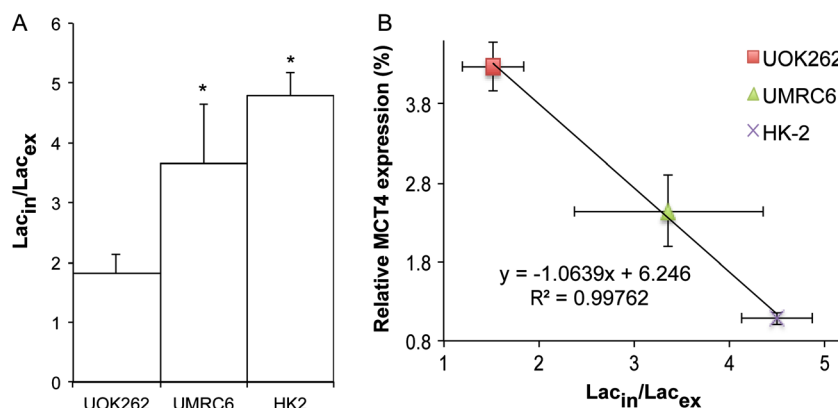


**Figure 5.** Estimation of extracellular HP lactate pools in renal cells of varying phenotypes. (A) Graph of  $\text{Lac}_{\text{in}}/\text{Lac}_{\text{ex}}$  for HK2, UMRC6, and UOK262 cell lines.  $\text{Lac}_{\text{in}}/\text{Lac}_{\text{ex}}$  increases going from UOK262 to UMRC6 to HK-2 ( $n = 3$  each). The metastatic UOK262 cell line had significantly ( $p < 0.05$ ) lower HP  $\text{Lac}_{\text{in}}/\text{Lac}_{\text{ex}}$  ratio than both HK2 and UMRC6 cell lines. (B) Graph of HP  $\text{Lac}_{\text{in}}/\text{Lac}_{\text{ex}}$  as a function of MCT4 mRNA expression. A negative linear correlation exists between the measured HP  $\text{Lac}_{\text{in}}/\text{Lac}_{\text{ex}}$  ratio and the MCT4 mRNA expression in the three cell lines studied. All data are represented as mean  $\pm$  standard error.

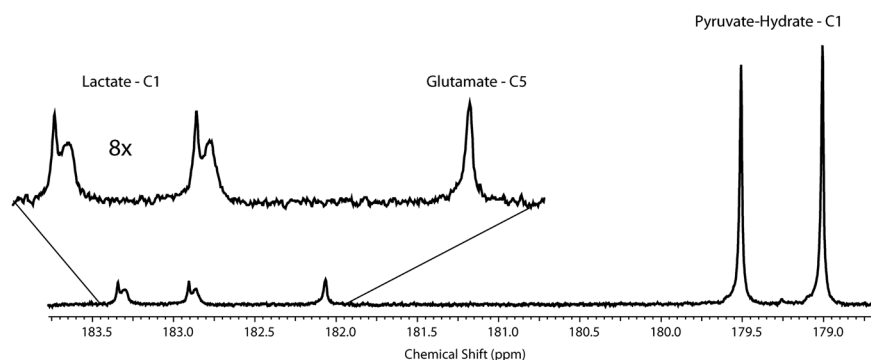


**Figure 6.**  $^{13}\text{C}$  spectrum of HP  $[1,2-^{13}\text{C}_2]$ pyruvate metabolism of tissue slice culture. Four tissue slices of a high-grade urothelial carcinoma were perfused in the 5 mm MR compatible bioreactor. The C-1 doublet of HP  $[1,2-^{13}\text{C}_2]$ lactate from metabolism of  $[1,2-^{13}\text{C}_2]$ pyruvate, each split into two peaks, represents the two cellular compartments. Only a singlet denoting the intracellular compartment is observed for the  $[5-^{13}\text{C}]$ glutamate, as seen in the spectral inset.

ratio of the extracellular pool of lactate to the total lactate signal ( $42 \pm 2\%$ ) is similar to the aggressive metastatic UOK262 cell line, indicating a similar upregulation of MCT4 mRNA expression. There was a threefold increase in MCT4 mRNA expression in patient-derived renal cancer relative to normal renal tissue, and a fourfold increase in MCT4 mRNA expression in UOK262 cells relative to normal HK2 cells.

## DISCUSSION

In this study, intra- and extracellular HP  $^{13}\text{C}$  lactate pools were dynamically measured using a 5 mm susceptibility-matched MR compatible 3D cell culture bioreactor. The intra- and extracellular HP lactate signals could be resolved in 1D  $^{13}\text{C}$  spectra due to a chemical shift difference between the two resonances ( $0.031 \pm 0.0005$  ppm), which was reproducible across studies and cell lines. Although the exact origin of the downfield shift of the  $\text{Lac}_{\text{ex}}$  relative to the  $\text{Lac}_{\text{in}}$  pool is not known, it was not due to a lower extracellular pH, since reduced extracellular pH would have resulted in a  $\text{Lac}_{\text{ex}}$  chemical shift in the opposite direction. The observed difference in chemical shift could arise from differences in the bulk magnetic susceptibility or differences in hydrogen bonding between the intra- and extracellular microenvironments. Intra- and extracellular chemical shift differences, attributed in part to bulk magnetic susceptibility, have been previously reported in  $^1\text{H}$ ,  $^{19}\text{F}$ ,  $^{31}\text{P}$ , and  $^{13}\text{C}$  magic angle spinning NMR spectra of erythrocyte cell suspensions (36,37) and for intra- and extracellular lipid signals in *in vivo* muscle spectra (38). Additionally, as observed by Kuchel *et al.* (36,37,39–42) and further validated by Barry *et al.* (43), protein-induced differences in hydrogen bonding between the intracellular and extracellular compartment have also resulted in NMR chemical shift differences between the compartments.

The extracellular HP lactate signal was used to discriminate normal HK-2 renal epithelial cells from both RCC cell lines (UOK262, UMRC6), and more importantly to differentiate the metastatic UOK262 RCC cell line from the localized RCC cell line UMRC6. The extracellular HP lactate findings are consistent with prior steady-state labeling studies with  $[1-^{13}\text{C}]$ glucose, which demonstrated that  $[3-^{13}\text{C}]$ lactate in the medium was highest for UOK262 followed by UMRC6 and HK2 cells (26). There was also a robust linear correlation between the MCT4 mRNA expression of the three cell lines and HP  $\text{Lac}_{\text{in}}/\text{Lac}_{\text{ex}}$  ratio, which is due

to significant changes in the  $\text{Lac}_{\text{ex}}$  pool size. This finding is consistent with the upregulation of aerobic glycolysis and lactate production and efflux associated with a more aggressive, metastatic cancer phenotype (9). The observed increased lactate efflux is known to be facilitated by an overexpression of MCT4 (MCTs) (27,28). It has been shown in numerous cancers, including cervical cancer (44), prostate cancer (45), lung cancer (46), and clear cell RCC (47), that MCT4 upregulation correlates with aggressive, invasive behavior. The MCT4 transporter serves two important functions: (1) the export of lactate to maintain a high rate of glycolysis and (2) removal of protons to maintain alkaline intracellular pH.  $^{31}\text{P}$  NMR measurements in this study demonstrated a constant alkaline intracellular pH for both of the RCC cell lines, consistent with the ability of cells to maintain a constant intracellular pH regardless of the degree of lactate production. While the cancer cell lines produced and transported more lactate out of the cell, the normal renal cell line also produced and transported a substantial amount of lactate. The relatively high level of extracellular HP lactate signal observed in the HK-2 cells could be due both to a metabolic aberration associated with immortalization of the normal renal epithelium and/or the fact that normal human kidney cortex cells also express substantial MCT4 (48), which is key to the lactate shuttle between the cortex and the medulla (49).

Considering the important function that MCT4 plays in maintaining the glycolytic tumor phenotype and alkaline intracellular pH, MCT4 inhibition has been considered as a therapeutic target (3,50), and this paper demonstrates that the MR compatible bioreactor platform can be used to monitor such a therapeutic approach in real time. The inhibition of lactate efflux by DIDS resulted in a significant reduction of the extracellular HP lactate pool in the aggressive metastatic UOK262 cell line. However, there was also a small reduction of the intracellular HP lactate pool, which is consistent with DIDS's ability to bind and inhibit both MCT1 and 4 transporters, although with different affinities. Consistent with the higher affinity of DIDS for MCT4 as compared with MCT1 (27), the observed significant increase in the  $\text{Lac}_{\text{in}}/\text{Lac}_{\text{ex}}$  ratio was primarily due to a reduction in the  $\text{Lac}_{\text{ex}}$  pool.

The results of these studies demonstrate the importance of lactate efflux as a biomarker of cancer presence and metastatic potential, and the utility of the MR compatible 3D cell and tissue culture bioreactor as a platform capable of studying not only cellular metabolism, but also transport and the impact of therapeutic interventions. The extension of these studies to living

patient-derived human renal cancer tissue slices was also demonstrated. Recent  $^1\text{H}$  and HP  $^{13}\text{C}$  MR studies of 3D patient-derived tissue slice cultures in a MR compatible bioreactor have demonstrated that they provide a more realistic model of the human situation for metabolic investigation (24). In this study we were able to observe the  $\text{Lac}_{\text{in}}$  and  $\text{Lac}_{\text{ex}}$  pools using five  $300\ \mu\text{m} \times 8\ \text{mm}$  slices ( $\approx 88\ \text{mg}$ ) of renal cancer obtained at surgery, after injection of HP  $[1,2\text{-}^{13}\text{C}_2]\text{pyruvate}$ . The use of the doubly labeled pyruvate allowed the measurement of flux to both HP  $[1,2\text{-}^{13}\text{C}_2]\text{Lactate}$  and  $[5\text{-}^{13}\text{C}]\text{glutamate}$ . Interestingly, the downfield shift of the  $\text{Lac}_{\text{ex}}$  resonance was identical to that observed for the renal cells, and the ratio of the extracellular pool of lactate to the total lactate signal was very similar to what was observed for the UOK262 cell line. This finding was consistent with overexpression of MCT4 in both RCC tissues and cells. The MCT4 mRNA expression in patient-derived renal cancer tissue slices was approximately three times higher than normal renal tissue, similar to the fold increase (four times higher) in MCT4 mRNA expression in UOK262 cells relative to the normal HK2 cells. Only a single resonance was observed in HP  $[5\text{-}^{13}\text{C}]\text{glutamate}$ , which arises from the C-2 carbon of HP  $[1,2\text{-}^{13}\text{C}_2]\text{pyruvate}$  in the TCA (tricarboxylic acid) cycle. This finding is consistent with glutamate being predominately intracellular (51,52), and demonstrates that this technique can be used to study the compartmentalization of metabolites other than lactate. The practicality of acquiring localized HP  $^{13}\text{C}$  MR kinetic data opens the possibility of measuring metabolic fluxes by fitting the dynamic data to kinetic models (15,53,54). However, the modeling of metabolic fluxes from HP  $^{13}\text{C}$  MR data is still in its infancy and current approaches suffer from a number of factors, including assumed/estimated  $T_1$  values, unknown metabolite pool sizes, and the assumptions underlying the specific models used. Therefore, the ability to measure metabolite pool sizes and estimate their respective  $T_1$  values in the very controlled environment of a 3D MR compatible bioreactor could aid in calculating and interpreting *in vivo* metabolic fluxes measured using HP  $^{13}\text{C}$  MR.

Although there are a number of ways to measure  $\text{Lac}_{\text{ex}}$  *in vitro*, only two of these techniques can be applied for *in vivo* measurements, namely steady-state MR spectroscopic and microelectrode measurements. Diffusion-weighted  $^1\text{H}$  and  $^1\text{H}\text{-}^{13}\text{C}$  (proton-observed carbon-edited) spectroscopy approaches have previously been used to assess the compartmentalization of the lactate in the rat brain *in vivo*, but these measurements are limited by poor signal to noise ratio, requiring long acquisition times for single time point, single voxel measurements (55,56) and therefore unable to provide dynamic measurements of lactate efflux, as is achievable for cells and tissues in the MR compatible bioreactor. While the microelectrode technique can yield dynamic measurements, it lacks specific localization, and is invasive (57). In contrast, the dynamic HP MR technique can estimate in real time the rate of lactate export from the cell and help distinguish between localized and metastatic cancer cells as demonstrated. HP  $^{13}\text{C}$  MR has already been applied to patient studies, thereby demonstrating future applicability to *in vivo* measurements (13). The small difference in chemical shift between the  $\text{Lac}_{\text{ex}}$  and  $\text{Lac}_{\text{in}}$  resonances observed in our *ex vivo* studies will be difficult to resolve *in vivo*. However, the results of such *ex vivo* studies can be used to help interpret the results of *in vivo* diffusion-weighted HP  $^{13}\text{C}$  MR studies in pre-clinical animal models (22,58), as well as future patient studies (20). This platform also could provide a rapid and inexpensive way to test efficacy of drugs that target cellular metabolism and transport.

## Acknowledgements

We thank Bertram Koelsch, Dave Korenchen, Sukumar Subramaniam, Justin Delos Santos, Romelyn Delos Santos and Jessie Lee for assistance in performing experiments.

qRT-PCR analysis was conducted at the Genome Analysis Core Facility, Helen Diller Family Comprehensive Cancer Center, University of California, San Francisco.

Grant Sponsors: National Institutes of Health (R01 EB013427, R01 EB017449, R01 CA183071, P41 EB013598, R21 EB005363, R00 EB014328 and R01 CA166655) and Department of Defense (USAMRMC CA110032).

## REFERENCES

- Hirschhaeuser F, Sattler UGA, Mueller-Klieser W. Lactate: a metabolic key player in cancer. *Cancer Res.* 2011; 71: 6921–6925.
- Feron O. Pyruvate into lactate and back: from the Warburg effect to symbiotic energy fuel exchange in cancer cells. *Radiother. Oncol.* 2009; 92: 329–333.
- Parks SK, Chiche J, Pouyssegur J. Disrupting proton dynamics and energy metabolism for cancer therapy. *Nat. Rev. Cancer* 2013; 13: 611–623.
- Estrella V, Chen T, Lloyd M, Wojtkowiak J, Cornnell HH, Ibrahim-Hashim A, Bailey K, Balagurunathan Y, Rothberg JM, Sloane BF, Johnson J, Gatenby RA, Gillies RJ. Acidity generated by the tumor microenvironment drives local invasion. *Cancer Res.* 2013; 73: 1524–1535.
- Gatenby RA, Gawlinski ET, Gmitro AF, Kaylor B, Gillies RJ. Acid-mediated tumor invasion: a multidisciplinary study. *Cancer Res.* 2006; 66: 5216–5223.
- Fukumura D, Xu L, Chen Y, Gohongi T, Seed B, Jain RK. Hypoxia and acidosis independently up-regulate vascular endothelial growth factor transcription in brain tumors *in vivo*. *Cancer Res.* 2001; 61: 6020–6024.
- Lardner A. The effects of extracellular pH on immune function. *J. Leukoc. Biol.* 2001; 69: 522–530.
- McCarty MF, Whitaker J. Manipulating tumor acidification as a cancer treatment strategy. *Altern. Med. Rev.* 2010; 15: 264–272.
- Dhup S, Kumar Dadhich R, Ettore Porporato P, Sonveaux P. Multiple biological activities of lactic acid in cancer: influences on tumor growth, angiogenesis and metastasis. *Curr. Pharm. Des.* 2012; 18: 1319–1330.
- Collier HA. Is cancer a metabolic disease? *Am. J. Pathol.* 2014; 184: 4–17.
- Keshari KR, Wilson DM. Chemistry and biochemistry of  $^{13}\text{C}$  hyperpolarized magnetic resonance using dynamic nuclear polarization. *Chem. Soc. Rev.* 2014; 43: 1627–1659.
- Kurhanewicz J, Vigneron DB, Brindle K, Chekmenev EY, Comment A, Cunningham CH, DeBerardinis RJ, Green GG, Leach MO, Rajan SS, Rizi RR, Ross BD, Warren WS, Malloy CR. Analysis of cancer metabolism by imaging hyperpolarized nuclei: prospects for translation to clinical research. *Neoplasia* 2011; 13: 81–97.
- Nelson SJ, Kurhanewicz J, Vigneron DB, Larson PEZ, Harzstark AL, Ferrone M, Van Criekinge M, Chang JW, Bok R, Park I, Reed G, Carvajal L, Small EJ, Munster P, Weinberg VK, Ardenkjaer-Larsen JH, Chen AP, Hurd RE, Odegardstuen L-I, Robb FJ, Tropp J, Murray JA. Metabolic imaging of patients with prostate cancer using hyperpolarized  $[1\text{-}^{13}\text{C}]\text{pyruvate}$ . *Sci. Transl. Med.* 2013; 5: 198ra108.
- Chen AP, Albers MJ, Cunningham CH, Kohler SJ, Yen YF, Hurd RE, Tropp J, Bok R, Pauly JM, Nelson SJ, Kurhanewicz J, Vigneron DB. Hyperpolarized C-13 spectroscopic imaging of the TRAMP mouse at 3T – initial experience. *Magn. Reson. Med.* 2007; 58: 1099–1106.
- Albers MJ, Bok R, Chen AP, Cunningham CH, Zierhut ML, Zhang VY, Kohler SJ, Tropp J, Hurd RE, Yen Y-F, Nelson SJ, Vigneron DB, Kurhanewicz J. Hyperpolarized  $^{13}\text{C}$  lactate, pyruvate, and alanine: noninvasive biomarkers for prostate cancer detection and grading. *Cancer Res.* 2008; 68: 8607–8615.
- Chen AP, Chu W, Gu Y-P, Cunningham CH. Probing early tumor response to radiation therapy using hyperpolarized  $[1\text{-}^{13}\text{C}]\text{pyruvate}$  in MDA-MB-231 xenografts. *PLoS ONE* 2013; 8: e56551.
- Brindle K. New approaches for imaging tumour responses to treatment. *Nat. Rev. Cancer.* 2008; 8: 1–14.



18. Park I, Bok R, Ozawa T, Phillips JJ, James CD, Vigneron DB, Ronen SM, Nelson SJ. Detection of early response to temozolomide treatment in brain tumors using hyperpolarized  $^{13}\text{C}$  MR metabolic imaging. *J. Magn. Reson. Imaging* 2011; 33: 1284–1290.
19. Chaumeil MM, Ozawa T, Park I, Scott K, James CD, Nelson SJ, Ronen SM. Hyperpolarized  $^{13}\text{C}$  MR spectroscopic imaging can be used to monitor Everolimus treatment in vivo in an orthotopic rodent model of glioblastoma. *NeuroImage* 2012; 59: 193–201.
20. Koelsch BL, Reed GD, Keshari KR, Chaumeil MM, Bok R, Ronen SM, Vigneron DB, Kurhanewicz J, Larson PEZ. Rapid in vivo apparent diffusion coefficient mapping of hyperpolarized  $^{13}\text{C}$  metabolites. *Magn. Reson. Med.* 2014; doi:10.1002/mrm.25422.
21. Schilling F, Düwel S, Köllisch U, Durst M, Schulte RF, Glaser SJ, Haase A, Otto AM, Menzel MI. Diffusion of hyperpolarized  $^{13}\text{C}$ -metabolites in tumor cell spheroids using real-time NMR spectroscopy. *NMR Biomed.* 2013; 26: 557–568.
22. Søgaard LV, Schilling F, Janich MA, Menzel MI, Ardenkjaer-Larsen JH. *In vivo* measurement of apparent diffusion coefficients of hyperpolarized  $^{13}\text{C}$ -labeled metabolites. *NMR Biomed.* 2014; 27: 561–569.
23. Keshari KR, Kurhanewicz J, Jeffries RE, Wilson DM, Dewar BJ, Van Criekinge M, Zierhut M, Vigneron DB, Macdonald JM. Hyperpolarized  $^{13}\text{C}$  spectroscopy and an NMR-compatible bioreactor system for the investigation of real-time cellular metabolism. *Magn. Reson. Med.* 2010; 63: 322–329.
24. Keshari KR, Sriram R, Van Criekinge M, Wilson DM, Wang ZJ, Vigneron DB, Peehl DM, Kurhanewicz J. Metabolic reprogramming and validation of hyperpolarized  $^{13}\text{C}$  lactate as a prostate cancer biomarker using a human prostate tissue slice culture bioreactor. *Prostate* 2013; 73: 1171–1181.
25. Keshari KR, Wilson DM, VanCriekinge M, Sriram R, Koelsch BL, VanBrocklin HF, Peehl DM, O'Brien T, Sampath D, Carano RAD, Kurhanewicz J. Metabolic response of prostate cancer to nicotinamide phosphoribosyltransferase inhibition in a hyperpolarized MR/PET compatible bioreactor. *The Prostate* 2015 in press; doi:10.1002/pros.23036.
26. Keshari KR, Sriram R, Koelsch BL, Van Criekinge M, Wilson DM, Kurhanewicz J, Wang ZJ. Hyperpolarized  $^{13}\text{C}$ -pyruvate magnetic resonance reveals rapid lactate export in metastatic renal cell carcinomas. *Cancer Res.* 2013; 73: 529–538.
27. Dimmer KS, Friedrich B, Lang F, Deitmer JW, Bröer S. The low-affinity monocarboxylate transporter MCT4 is adapted to the export of lactate in highly glycolytic cells. *Biochem. J.* 2000; 350(1): 219–227.
28. Carpenter L, Halestrap AP. The kinetics, substrate and inhibitor specificity of the lactate transporter of Ehrlich-Lettre tumour cells studied with the intracellular pH indicator BCECF. *Biochem. J.* 1994; 304(3): 751–760.
29. Ryan MJ, Johnson G, Kirk J, Fuerstenberg SM, Zager RA, Torok-Storb B. HK-2: an immortalized proximal tubule epithelial cell line from normal adult human kidney. *Kidney Int.* 1994; 45: 48–57.
30. Grossman HB, Wedemeyer G, Ren LQ. Human renal carcinoma: characterization of five new cell lines. *J. Surg. Oncol.* 1985; 28: 237–244.
31. Albers MJ, Butler TN, Rahwa I, Bao N, Keshari KR, Swanson MG, Kurhanewicz J. Evaluation of the ERETIC method as an improved quantitative reference for  $^1\text{H}$  HR-MAS spectroscopy of prostate tissue. *Magn. Reson. Med.* 2009; 61: 525–532.
32. Adam WR, Koretsky AP, Weiner MW.  $^{31}\text{P}$ -NMR in vivo measurement of renal intracellular pH: effects of acidosis and  $\text{K}^+$  depletion in rats. *Am. J. Physiol. Renal Physiol.* 1986; 251(5): F904–F910.
33. Lutz NW, Franks SE, Frank MH, Pomer S, Hull WE. Investigation of multidrug resistance in cultured human renal cell carcinoma cells by  $^{31}\text{P}$ -NMR spectroscopy and treatment survival assays. *Magn. Reson. Mater. Phys. Biol. Med.* 2005; 18: 144–161.
34. Thong AE, Zhao H, Ingels A, Valta MP, Nolley R, Santos J, Young SR, Peehl DM. Tissue slice grafts of human renal cell carcinoma: an authentic preclinical model with high engraftment rate and metastatic potential. *Urol. Oncol.* 2014; 32: 43.e23–30.
35. Wirthssohn G, Guder WG. Renal substrate metabolism. *Physiol. Rev.* 1986; 66: 469–497.
36. Philp DJ, Bubba WA, Kuchel PW. Chemical shift and magnetic susceptibility contributions to the separation of intracellular and supernatant resonances in variable angle spinning NMR spectra of erythrocyte suspensions. *Magn. Reson. Med.* 2004; 51: 441–444.
37. Kuchel PW, Chapman BE, Xu ASL. Rates of anion transfer across erythrocyte membranes measured with NMR spectroscopy. *Prog. Cell Res.* 1992; 2: 105–119.
38. Boesch C, Kreis R. Dipolar coupling and ordering effects observed in magnetic resonance spectra of skeletal muscle. *NMR Biomed.* 2001; 14: 140–148.
39. Kirk K, Kuchel PW. Physical basis of the effect of hemoglobin on the phosphorus-31 NMR chemical shifts of various phosphoryl compounds. *Biochemistry* 1988; 27: 8803–8810.
40. Kuchel PW. Spin-exchange NMR spectroscopy in studies of the kinetics of enzymes and membrane transport. *NMR Biomed.* 1990; 3: 102–119.
41. Potts JR, Hounslow AM, Kuchel PW. Exchange of fluorinated glucose across the red-cell membrane measured by  $^{19}\text{F}$ -n.m.r. magnetization transfer. *Biochem. J.* 1990; 266: 925–928.
42. Larkin TJ, Bubba WA, Kuchel PW. pH and cell volume effects on  $\text{H}_2\text{O}$  and phosphoryl resonance splitting in rapid-spinning NMR of red cells. *Biophys. J.* 2007; 92: 1770–1776.
43. Barry JA, McGovern KA, Lien YH, Ashmore B, Gillies RJ. Dimethyl methylphosphonate (DMMP): a  $^{31}\text{P}$  nuclear magnetic resonance spectroscopic probe of intracellular volume in mammalian cell cultures. *Biochemistry* 1993; 32: 4665–4670.
44. Pinheiro C, Longatto-Filho A, Pereira SMM, Etlinger D, Moreira MAR, Jubé LF, Queiroz GS, Schmitt F, Baltazar F. Monocarboxylate transporters 1 and 4 are associated with CD147 in cervical carcinoma. *Dis. Markers* 2009; 26: 97–103.
45. Pinheiro C, Longatto-Filho A, Azevedo-Silva J, Casal M, Schmitt FC, Baltazar F. Role of monocarboxylate transporters in human cancers: state of the art. *J. Bioenerg. Biomembr.* 2012; 44: 127–139.
46. Meijer T, Schuurbiers O, Kaanders J. Differences in metabolism between adeno- and squamous cell non-small cell lung carcinomas: spatial distribution and prognostic value of GLUT1 and MCT4. *Lung Cancer* 2012; 76: 316–323.
47. Gerlinger M, Santos CR, Spencer-Dene B, Martinez P, Endesfelder D, Burrell RA, Vetter M, Jiang M, Saunders RE, Kelly G, Dykema K, Rioux-Leclercq N, Stamp G, Patard J-J, Larkin J, Howell M, Swanton C. Genome-wide RNA interference analysis of renal carcinoma survival regulators identifies MCT4 as a Warburg effect metabolic target. *J. Pathol.* 2012; 227: 146–156.
48. Wang Q, Lu Y, Yuan M, Darling IM, Repasky EA, Morris ME. Characterization of monocarboxylate transport in human kidney HK-2 cells. *Mol. Pharm.* 2006; 3: 675–685.
49. Bellomo R. Bench-to-bedside review: lactate and the kidney. *Crit. Care* 2002; 6: 322.
50. Kennedy KM, Dewhirst MW. Tumor metabolism of lactate: the influence and therapeutic potential for MCT and CD147 regulation. *Future Oncol.* 2010; 6: 127–148.
51. Gegelashvili G, Schousboe A. Cellular distribution and kinetic properties of high-affinity glutamate transporters. *Brain Res. Bull.* 1998; 45: 233–238.
52. Danbolt NC. Glutamate uptake. *Prog. Neurobiol.* 2001; 65: 1–105.
53. Lee P, Leong W, Tan T, Lim M, Han W, Radda GK. *In vivo* hyperpolarized carbon-13 magnetic resonance spectroscopy reveals increased pyruvate carboxylase flux in an insulin-resistant mouse model. *Hepatology* 2013; 57: 515–524.
54. Zierhut ML, Yen Y-F, Chen AP, Bok R, Albers MJ, Zhang V, Tropp J, Park I, Vigneron DB, Kurhanewicz J, Hurd RE, Nelson SJ. Kinetic modeling of hyperpolarized  $^{13}\text{C}$ -pyruvate metabolism in normal rats and TRAMP mice. *J. Magn. Reson.* 2010; 202: 85–92.
55. Pfeuffer J, Tkáč I, Gruetter R. Extracellular–intracellular distribution of glucose and lactate in the rat brain assessed noninvasively by diffusion-weighted  $^1\text{H}$  nuclear magnetic resonance spectroscopy *in vivo*. *J. Cereb. Blood Flow Metab.* 2000; 20: 736–746.
56. Pfeuffer J, Lin JC, Delabarre L, Uğurbil K, Garwood M. Detection of intracellular lactate with localized diffusion  $\{^1\text{H}-^{13}\text{C}\}$ -spectroscopy in rat glioma *in vivo*. *J. Magn. Reson.* 2005; 177: 129–138.
57. Rassaei L, Olthuis W, Tsujimura S, Sudhölter EJR, van den Berg A. Lactate biosensors: current status and outlook. *Anal. Bioanal. Chem.* 2014; 406: 123–137.
58. Patrick PS, Kettunen MI, Tee SS, Rodrigues TB, Serrao E, Timm KN, McGuire S, Brindle KM. Detection of transgene expression using hyperpolarized  $^{13}\text{C}$  urea and diffusion-weighted magnetic resonance spectroscopy. *Magn. Reson. Med.* 2014.

## SUPPORTING INFORMATION

Additional supporting information may be found in the online version of this article at the publisher's web site.



# Appendix V

## **Noninvasive differentiation of benign renal tumors from renal cell carcinomas using clinically translatable hyperpolarized $^{13}\text{C}$ pyruvate magnetic resonance**

Renuka Sriram<sup>1\*</sup>, Mark Van Criekinge<sup>1</sup>, Justin DeLos Santos<sup>1</sup>, Kayvan R. Keshari<sup>2</sup>,  
Donna Peehl<sup>3</sup>, John Kurhanewicz<sup>1</sup> and Zhen J. Wang<sup>1</sup>

1. Radiology and Biomedical Imaging, University of California San Francisco, San Francisco, CA, United States.
2. Radiology and Molecular Pharmacology and Chemistry Program, Memorial Sloan Kettering Cancer Center, New York, NY, United States. 2. Stanford University, Stanford CA, United States.

\*Correspondence and Reprint Request:

University of California, San Francisco

San Francisco, CA 94158

Tel: (415)

Fax: (415) 514

Email: @ucsf.edu

Grant Sponsor: National Institutes of Health (R01 EB013427, R01 EB017449, R01 CA183071, P41 EB013598, R21 EB005363, R00 EB014328 and R01 CA166655) and Department of Defense (USAMRMC CA110032)

Word Count:

Running Title:

**Noninvasive differentiation of benign renal tumors from renal cell carcinomas using clinically translatable hyperpolarized  $^{13}\text{C}$  pyruvate magnetic resonance**

Keywords: Hyperpolarized  $^{13}\text{C}$  magnetic resonance (HP  $^{13}\text{C}$  MR), dynamic nuclear polarization (DNP), pyruvate, lactate, aerobic glycolysis, lactate efflux, renal cell carcinoma (RCC), cancer aggressiveness, patient derived tissue slice cultures

Abbreviations used:

HP – hyperpolarized  
MR – magnetic resonance  
MRS – magnetic resonance spectroscopy  
DNP – dynamic nuclear polarization  
RCC – renal cell carcinoma  
VEGF – vascular endothelial growth factor  
DMEM - Dulbecco's Modified Eagle's medium  
ATP – adenosine tri-phosphate  
MCT – monocarboxylate transporter  
LDH – lactate dehydrogenase  
TCA – tricarboxylic acid  
S/N – signal to noise ratio  
  
LWHM – Line width at half maximum

## **Introduction**

The widespread use of cross-sectional imaging has led to a significant increase in the incidence of renal tumors (1), many of which are localized, clinical stage 1 tumors.

These tumors have a wide spectrum of benign and malignant histology and aggressiveness, and pose significant challenges in clinical management. Approximately 20% of the clinical stage 1 renal tumors are benign tumors such as oncocytomas or minimal fat angiomyolipomas (2-5). These benign tumors cannot be reliably differentiated from RCCs preoperatively using conventional imaging (6). Percutaneous tumor biopsy also has its limitations, including low negative predictive value of biopsy for small renal masses and overlapping histologic features between some benign renal tumors and RCCs (7). Because of these limitations, localized renal tumors are most

frequently treated with surgical resection. This has led to greater than 10,000 unnecessary operations of benign tumors each year in the U.S. alone (8), with inherent risks of surgery, loss of renal function, and cost. Therefore, new imaging methods are needed to distinguish benign renal tumors from RCCs in order to guide management.

Increasing evidence has shown that RCCs are strongly linked to abnormal metabolism (9, 10). In particular, increased glycolysis with lactate production (Warburg effect) is a dominant metabolic feature of RCCs. For example, clear cell RCCs, which account for 70-80% of all RCCs, have characteristic reprogramming of glucose and energy metabolism that promotes glycolysis and lactate production (11, 12) (39, 40). High expression of monocarboxylate transporters 1 and 4, which are essential for maintaining high level of glycolysis and lactate transport, are associated with more aggressive RCCs (13-15). These studies provide the rationale for metabolic imaging as a means to differentiate benign renal tumors from RCCs.

Hyperpolarized carbon-13 (HP  $^{13}\text{C}$ ) magnetic resonance (MR) is a powerful molecular imaging technique that allows rapid and noninvasive investigation of dynamic metabolic and physiological processes previously inaccessible by imaging (16). HP  $^{13}\text{C}$  pyruvate is the most widely studied probe to date (17, 18), reflecting its central role in cellular metabolism. In particular, pyruvate is reduced to lactate in a reaction catalyzed by the enzyme lactate dehydrogenase. Several previous studies have shown that *in vivo* HP  $^{13}\text{C}$  pyruvate to lactate flux can provide noninvasive markers of tumor grade in preclinical cancer models (19, 20). Notably, the safety and feasibility of HP  $^{13}\text{C}$  pyruvate has already been demonstrated in the phase I clinical trial in prostate cancer patients (21), which opens doors for potential clinical translation of this technology to other diseases.

In this study, we compared the HP  $^{13}\text{C}$  pyruvate-to-lactate flux in living patient-derived renal tumor tissue slices maintained in a MR-compatible bioreactor. The bioreactor provides a platform for the assessment of tissue metabolism in a controlled and physiologic setting. We showed that, compared to benign renal tumors, clear cell RCCs have more rapid export of lactate out of the cells, likely mediated by the elevated monocarboxylate transporter 4 expression. This suggests that HP  $^{13}\text{C}$  pyruvate has the potential to noninvasively differentiate benign renal tumors from RCCs.

## **Material and Methods**

### **Patient derived renal tissue slice**

Fresh tissues were obtained from patients undergoing nephrectomy for renal tumors between September 2012 and August 2014 under an institutional review board approved protocol. Eight mm cores of both the tumors and uninvolved normal renal parenchyma were obtained from the nephrectomy specimen (22). The tissues were precision cut to 300-350 micron thick slices using a Krumdieck slicer, and then cultured for 12-18 hours in specialized media in an angled rotating plate at 30° degree as previously described (23). Subsequently, 4-6 tissue slices were loaded into a 5mm MR compatible bioreactor (24, 25) for hyperpolarized experiment below.

### **3D MR compatible bioreactor experiments**

The tissue slices were maintained at physiological conditions in the bioreactor in circulating media at 37°C with 95% air/5% CO<sub>2</sub> via a gas exchanger. All the bioreactor experiments were conducted using a 500MHz Varian Inova (Agilent Technologies, Palo

Alto, CA) with a 5mm, triple-tune, direct-detect, broadband probe. For the HP  $^{13}\text{C}$  pyruvate studies, 7.5 uL of 14.2 M [ $1\text{-}^{13}\text{C}$ ]pyruvate mixed with 15 mM of the trytl radical (GE Health, Menlo Park, CA, USA) and 2.5 mM gadolinium chelate was polarized on a Hypersense polarizer (Oxford Instruments, Oxford, UK). This was followed by dissolution in 5 mL of 50 mM phosphate buffer. 750 uL of the resulting 16mM HP  $^{13}\text{C}$  pyruvate solution was injected over 90 seconds into the bioreactor containing the tissue slices. Hyperpolarized  $^{13}\text{C}$  MR data were acquired dynamically with a  $30^\circ$  flip angle, pulse repetition time of 3s and for a duration of 300 seconds.  $^{31}\text{P}$  spectra were acquired before and after each hyperpolarized  $^{13}\text{C}$  study to assess tissue viability, using a repetition time of 2s, 2048 averages and a  $90^\circ$  flip angle. The  $\beta\text{NTP}$  peak was quantified using the ERETC method (26).

### **Immunohistochemical staining and pathological grading**

At the end of the MR experiments, the renal tissue slices were rapidly fixed in cryo-embedding media (Optimal Cutting Temperature Compound) and frozen for subsequent histological and immunohistochemical analyses. The renal tumor histology and grade (Furhman nuclear grading if RCCs) were determined by a clinical pathologist on hemotoxylin and eosin (H&E) staining. Additionally, the slices were also stained for proliferation (Ki67) and MCT4 (monocarboxylate 4) expression. The pathological features of the tissue slices used for the bioreactor study is summarized in table 1.

### **Lactate efflux measurement of renal tissue slices**



Adjacent tissue slices from the same nephrectomy specimen were incubated in 2D culture in medium containing 25mM [3-<sup>13</sup>C]pyruvate. The rate of lactate efflux from the tissue slices was evaluated by sampling the media every 60-120 minutes serially over 8 hours. The lactate in the medium was measured by <sup>1</sup>H MR spectroscopy in a 800MHz Bruker DRX spectrometer (Billerica, MA) equipped with a cryo-cooled 5mm triple-axis heteronuclear probe. The J-coupled <sup>13</sup>C satellite resonance was quantified using ACD/Labs software as described below.

#### **Tissue slice mRNA expression and enzyme activity assay**

mRNA expression of LDHA, MCT1 and MCT4 was determined by qRT-PCR as described previously (24, 27). Total RNA was extracted from the tissue slices with RNAeasy procedure kit (Qiagen, USA). Reverse transcription using iScript cDNA Synthesis kit (BioRad Laboratories, Hercules, CA, USA) was performed and subsequently the cDNA generated was utilized for PCR in triplicate with TaqMan chemistry on the ABI 7900HT (Applied Biosystems, Foster City, CA, USA). Primers for the genes were obtained from Applied Biosystems (Foster City, CA, USA). The gene expression was calculated relative to the housekeeping gene b-actin in the log scale.

LDH activity of tissue slices was measured spectrophotometrically by quantifying the linear decrease in NADH absorbance at varying pyruvate concentrations at 339 nm using a micro-plate reader (Tecan Group Ltd.) (24). The maximum velocity (V<sub>max</sub>) and the Michaelis–Menten constant (K<sub>m</sub>) were estimated using the Lineweaver–Burke plot and was normalized to the protein content.

## Data analysis

The MR data was processed and analyzed using ACD/Labs software (Toronto, Ontario, Canada). The  $^{13}\text{C}$  data were processed with minimal line broadening and the dynamic data were summed and is expressed as a ratio of the hyperpolarized lactate peak area to that of pyruvate in order to normalize any differences in polarization across experiments. All data are represented as mean  $\pm$  standard error. Two-tailed Student's t-test was used to assess the difference between groups.

## Results

### **Bioenergetics and viability of renal tissue slices in the 3D MR compatible bioreactor:**

Patient-derived renal slices were obtained from 10 ccRCC (predominantly of Furhman grade 2, with one case each for grade 1 and 3), 3 benign renal tumors (2 oncocytomas and one angiomyolipoma), and 12 normal renal parenchyma tissues not involved by tumors. These fresh tissue slices were studied in a 3D tissue bioreactor.

The micro-engineered 3D 5mm tube MR compatible bioreactor has been shown previously to allow maintenance of tissue viability and to provide reproducible HP MR data {Keshari:2013ip}. In this study, it allowed the metabolic evaluation of 60-90 mg of tissue and had excellent  $B_0$  field homogeneity (average water line width at half maximum was  $12.2 \pm 0.68$  Hz).  $^{31}\text{P}$  MR spectroscopy was employed to monitor changes in renal tissue bioenergetics during the bioreactor studies. Figure 1A shows a representative spectrum of a clear cell RCC (ccRCC). NMR signals for the nucleoside triphosphates (NTPs:  $\gamma\text{NTP}$ ,  $\alpha\text{NTP}$ , and  $\beta\text{NTP}$ ), phosphocholine (PC), inorganic phosphate ( $\text{P}_i$ ), and glycerol phosphocholine (GPC) were readily visible. The  $\beta\text{NTP}$  content was unchanged following the injection of HP  $^{13}\text{C}$  pyruvate, indicating maintenance of tissue bioenergetics

during the course of hyperpolarized experiments. Furthermore, we showed that tissue viability was maintained in the bioreactor with near constant  $\beta$ NTP for over 24 hours ( inset of figure 1A).

Figure 1B shows the varying levels of phospholipids in the renal tissue slices. Interestingly the phosphocholine (PC) level in the benign renal tumors is significantly higher than both the normal renal parenchyma ( $p=0.019$ ) and ccRCC ( $p=0.008$ ) tissues. This finding is similar to that of prior  $^1\text{H}$  high-resolution study of renal tissue extracts {Tugnoli:2003bu}, and indicates that while PC has been used as a biomarker of tumor proliferation and aggressiveness in other types of cancer {Podo:1999er}, it has limited value for renal tumor characterization. PC is converted from choline by the enzyme choline kinase-alpha (CHKA) in the phosphatidylcholine synthesis (kennedy) pathway. A prior study reported that functional interaction between CHK-alpha, EGFR receptor and c-Src is required for cell proliferation. Such functional interaction may explain the lack of direct correlation between PC level and renal tumor aggressiveness in our study. The glycerophosphocholine (GPC) is significantly higher in both benign renal tumors and ccRCCs compared to normal renal parenchyma tissue ( $p=0.027$  and  $0.003$  respectively). While GPC is an osmolyte in the renal medulla, it is also involved in cell membrane synthesis and breakdown. The higher level in both the benign renal tumors and the ccRCCs compared to normal renal parenchyma may be ascribed to tumor cell proliferation.

**Hyperpolarized  $^{13}\text{C}$  pyruvate metabolism of renal tissue slices in the 3D MR compatible bioreactor:**

Figure 2A illustrates the scheme of  $^{13}\text{C}$  labeled carbon atom transitions used to detect [1- $^{13}\text{C}$ ] pyruvate metabolism during the HP MR experiment. After injection of hyperpolarized [1- $^{13}\text{C}$ ]pyruvate into the bioreactor, the pyruvate to lactate conversion in the renal tissue slices was assessed in real time. The  $^{13}\text{C}$  lactate spectrum had excellent SNR of  $15 \pm 2$  (**figure 2B**). Both the benign renal tumors and ccRCCs showed higher pyruvate to lactate conversion, consistent with higher glycolysis, when compared to normal renal parenchymal tissues (both p-values < 0.05). However, the observed pyruvate to lactate conversion was lower in ccRCCs than benign renal tumors. Prior studies of RCC cells in a similar continuous perfusion system showed that rapidly exported  $^{13}\text{C}$  lactate quickly flows out of the MR sensitive volume without contributing to the measured hyperpolarized lactate signal (27). Therefore, we hypothesize that the apparent lower pyruvate to lactate conversion in ccRCC when compared to benign renal tumors may be a result of rapid lactate efflux in ccRCCs.

Hyperpolarized alanine was detectable only in the normal renal tissues with a SNR of at least 3. Alanine was not detectable in the benign renal tumor tissues, and it was occasionally observed (in 1/3 of the cases) at low levels in the ccRCC tissues. The low alanine level in the tumor tissues may be a result of the increased pyruvate to lactate conversion.

**Tissue analysis confirms that ccRCCs have higher lactate production and efflux than benign renal tumors:**

To test the hypothesis that ccRCCs have higher lactate production and efflux than benign renal tumors, we then assayed the mRNA expressions and enzyme activity of LDH, and the mRNA expression of MCT1 and MCT4 of the tissue slices. LDHA encodes the M subunits of LDH, which catalyzes the conversion between pyruvate and lactate. MCT1 mediates the pyruvate transport into the cells, and MCT4 mediates the efflux of the lactate out of the cells (ref). The LDH-A mRNA expression was significantly higher in ccRCCs compared to both normal renal tissues and benign tumors ( $p=0.001$  and  $p=0.016$  respectively) (**figure.3A**). Additionally the LDH activity was also significantly higher ( $p<0.05$ ) in ccRCC compared to the normal renal tissues and benign tumors by 2.4 and 1.7 times respectively (**figure.3B**). [need MCT1 data here]. The MCT4 mRNA expression in the ccRCCs was four-fold higher ( $p=0.021$ ) than that normal renal tissues and almost 7 fold higher than that of benign tumors ( $p=0.045$ ). Corresponding immunohistochemical staining also showed progressively increased MCT4 staining from normal renal tissues to ccRCCs. To further verify that the higher MCT4 expression in ccRCCs resulted in increased lactate efflux, we quantified the rate of lactate efflux in the tissue slices in culture by thermal labeling with  $[3-^{13}\text{C}]$ pyruvate. The incubating media was sampled periodically for up to 8 hours and the  $[3-^{13}\text{C}]$ lactate was measured using high-resolution MR spectroscopy. The normal renal tissues and benign tumors had similar levels of lactate efflux rate, while ccRCCs had significantly higher efflux rate of  $5 \pm 0.57$  nmols/min ( $p=0.01$  and  $0.002$  respectively). Taken together, these observations support the notion that ccRCCs have the highest lactate production and efflux compared to benign renal tumors and normal renal tissues. The rapid lactate efflux likely accounted for the apparent lower HP lactate in ccRCCs than benign renal tumors.



## Discussion and Conclusion

An unmet need in the management of patients with localized renal tumors is the lack of imaging biomarkers that can reliably discriminate benign tumors from RCCs. In this study, we investigated the pyruvate metabolism in living patient-derived renal tumor tissues using a clinically translatable HP  $^{13}\text{C}$  MR probe. We showed that rapid lactate efflux is a characteristic feature of clear cell RCC, which comprise the majority of RCCs, and that this feature can be used to differentiate cancers from benign renal tumors.

Lactate efflux is predominantly mediated by MCT4, a proton-coupled lactate transporter, exporting lactate and  $\text{H}^+$  in the same direction out of the cells. Rapid lactate export plays a key role in maintaining high level of lactate production, acidifying the tumor interstitium and promoting invasion and metastasis, all key features of cancers. The potential importance of MCT4 in RCCs was suggested by a recent study which showed that MCT4 protein expression in clear cell RCC was associated with poorer relapse-free survival, and correlated with Fuhrman nuclear grade. In our current work, we showed that the rapid lactate efflux, likely as a result of high MCT4 expression in the patient –derived clear cell RCC tissues, can be monitored using HP  $^{13}\text{C}$  MR. We also showed, to our knowledge, for the first time that clear cell RCCs have higher MCT4 expression compared to benign renal tumors. Such differential expression and the resultant lactate efflux rate may be explored noninvasively using HP  $^{13}\text{C}$  MR. In our current pre-clinical study which utilized an ex vivo system, the higher lactate export in RCCs compared to benign tumors was inferred from a combination of HP  $^{13}\text{C}$  MR and steady-state labeling experiment. However, it is possible to discriminate the local

environment of HP metabolites using diffusion-weighted HP  $^{13}\text{C}$  MR in vivo. Our findings provide rationale for such in vivo studies, and work is ongoing to use in vivo diffusion-weighted HP  $^{13}\text{C}$  MR to directly interrogate the relative amount of intracellular versus extracellular lactate.

The development of novel imaging markers of RCC presence and aggressiveness has been impeded by the lack of robust models that recapitulate human disease. Available preclinical models are predominantly based on immortalized aggressive RCC cells either grown in culture or implanted in animals. We have previously studied pyruvate metabolism in immortalized RCC cells (27), but were not able to investigate the metabolism of benign renal tumors as there are no existing preclinical models of benign human renal tumors. Immortalized RCC cells also have unusually high proliferation indices compared to patient-derived renal tumor tissues, which may be reflected in the observed metabolism. Furthermore, immortalized cell models do not capture the complex tumor cell-matrix interactions which occur in human renal tumors, and which are likely important for tumor metabolism. To overcome these difficulties, we utilized in this study patient-derived renal tumor slice model for the metabolic assessment of intact living human tissues. The novel MR-compatible micro-engineered bioreactor permits evaluation of living tissue metabolism in a physiological environment, and has been previously validated by our group in prostate cancer studies (24). The combination of primary human renal tumor tissue slices and MR-compatible bioreactor provides a unique and realistic model for HP  $^{13}\text{C}$  biomarker discovery in renal tumors prior to patient studies.

The main limitation of our study is the small number of benign renal tumors. A high percentage of tumor tissues was from radical nephrectomy for large renal tumors (average size of 6.6cm). The proportion of benign tumors was low in this cohort since benign tumors tend to be smaller in size (~3cm), and more likely to be treated with partial nephrectomy. Nonetheless, we have shown a significant difference in both the hyperpolarized  $^{13}\text{C}$  data and the tissue correlative findings between benign tumors and RCCs. The results of the study provide motivation for future clinical studies of HP  $^{13}\text{C}$  pyruvate MR in patients with renal tumors. Another limitation of our study is that we have only included clear cell RCCs, and not other subtypes of RCCs. This in part reflects the fact that clear cell RCCs comprises majority of RCCs (70-80%), and we did not obtain sufficient number of other subtype of RCCs to include in our analysis. An additional limitation of our study is that the majority of the clear cell RCC tissues we obtained were grade 1 or 2. We did not have sufficient number of higher grade (grade 3 or 4) clear cell RCCs to perform separate analysis based on grade, and future studies are warranted to assess any potential grade dependent findings. Development of imaging markers that can reliably differentiate low from high grade RCCs will be of great interest given the increasing recognition that low grade indolent RCCs may be treated conservatively.

Notwithstanding these limitations, we showed that high lactate production and rapid lactate efflux is a dominant feature of clear cell RCC, and that this feature can be explored to differentiate cancers from benign renal tumors using hyperpolarized  $^{13}\text{C}$  MR. These initial findings provide strong motivation for developing hyperpolarized  $^{13}\text{C}$  MR

for clinical evaluation of renal tumors, a disease with increasing frequency, with the ultimate goal of guiding treatment selection.

## References

1. Sun M, Thuret R, Abdollah F, Lughezzani G, Schmitges J, Tian Z, Shariat SF, Montorsi F, Patard JJ, Perrotte P, Karakiewicz PI. Age-adjusted incidence, mortality, and survival rates of stage-specific renal cell carcinoma in North America: a trend analysis. *European Urology*, 2010 ed. 2011;59:135–141.
2. Frank I, Blute ML, Cheville JC, Lohse CM, Weaver AL, Zincke H. Solid renal tumors: an analysis of pathological features related to tumor size. *J Urol* 2003;170:2217–2220.
3. Snyder ME, Bach A, Kattan MW, Raj GV, Reuter VE, Russo P. Incidence of benign lesions for clinically localized renal masses smaller than 7 cm in radiological diameter: influence of sex. *J Urol* 2006;176:2391–5– discussion 2395–6.
4. DeRoche T, Walker E, Magi-Galluzzi C, Zhou M. Pathologic characteristics of solitary small renal masses: can they be predicted by preoperative clinical parameters? *Am J Clin Pathol* 2008;130:560–564.
5. Murphy AM, Buck AM, Benson MC, McKiernan JM. Increasing detection rate of benign renal tumors: evaluation of factors predicting for benign tumor histologic features during past two decades. *Urology*, 2009 ed. 2009;73:1293–1297.
6. Woo S, Cho JY. Imaging Findings of Common Benign Renal Tumors in the Era of Small Renal Masses: Differential Diagnosis from Small Renal Cell Carcinoma: Current Status and Future Perspectives. *Korean J Radiol* 2015;16:99.

7. Ljungberg B, Hanbury DC, Kuczyk MA, Merseburger AS, Mulders P, Patard JJ, Sinescu IC. Guidelines on renal cell carcinoma. *European Association of Urology* 2008;1:1–22.
8. Asnis-Alibozek AG, Fine MJ, Russo P, McLaughlin T, Farrelly EM, LaFrance N, Lowrance W. Cost of care for malignant and benign renal masses. *Am J Manag Care* 2013;19:617–624.
9. Pinthus JH, Whelan KF, Gallino D, Lu J-P, Rothschild N. Metabolic features of clear-cell renal cell carcinoma: mechanisms and clinical implications. *Canadian Urological Association Journal* 2011;5:274–282.
10. Zaravinos A, Pieri M, Mourmouras N, Anastasiadou N, Zouvani I, Delakas D, Deltas C. Altered metabolic pathways in clear cell renal cell carcinoma: A meta-analysis and validation study focused on the deregulated genes and their associated networks. *Oncoscience*. 2014;
11. Unwin RD, Craven RA, Harnden P, Hanrahan S, Totty N, Knowles M, Eardley I, Selby PJ, Banks RE. Proteomic changes in renal cancer and co-ordinate demonstration of both the glycolytic and mitochondrial aspects of the Warburg effect. *Proteomics* 2003;3:1620–1632.
12. Singer K, Kastenberger M, Gottfried E, Hammerschmied CG, Büttner M, Aigner M, Seliger B, Walter B, Schlösser H, Hartmann A, Andreesen R, Mackensen A, Kreutz M. Warburg phenotype in renal cell carcinoma: High expression of glucose-transporter 1 (GLUT-1) correlates with low CD8+ T-cell infiltration in the tumor. *Int J Cancer* 2010;128:2085–2095.
13. Fisel P, Stühler V, Bedke J, Winter S, Rausch S, Hennenlotter J, Nies AT, Stenzl A, Scharpf M, Fend F, Kruck S, Schwab M, Schaeffeler E. MCT4 surpasses the prognostic relevance of the ancillary protein CD147 in clear cell renal cell carcinoma. *Oncotarget* 6:30615–30627.
14. Fisel P, Kruck S, Winter S, Bedke J, Hennenlotter J, Nies AT, Scharpf M, Fend F, Stenzl A, Schwab M, Schaeffeler E. DNA Methylation of the SLC16A3 Promoter Regulates Expression of the Human Lactate Transporter MCT4 in Renal Cancer with Consequences for Clinical Outcome. *Clinical Cancer Research* 2013;19:5170–5181.
15. Gerlinger M, Santos CR, Spencer-Dene B, Martinez P, Endesfelder D, Burrell RA, Vetter M, Jiang M, Saunders RE, Kelly G, Dykema K, Rioux-Leclercq N, Stamp G, Patard J-J, Larkin J, Howell M, Swanton C. Genome-wide RNA interference analysis of renal carcinoma survival regulators identifies MCT4 as a Warburg effect metabolic target. *J Pathol* 2012;227:146–156.
16. Keshari KR, Wilson DM. Chemistry and biochemistry of <sup>13</sup>C hyperpolarized magnetic resonance using dynamic nuclear polarization. *Chem Soc Rev* 2014;43:1627–1659.
17. Sriram R, Kurhanewicz J, Vigneron DB. Hyperpolarized Carbon-13 MRI and MRS Studies. *eMagRes* 2014;3:311–324.
18. Chaumeil MM, Najac C, Ronen SM. Studies of Metabolism Using <sup>13</sup>C MRS of Hyperpolarized Probes. *sciencedirectcom Elsevier*; 2015. doi:10.1016/bs.mie.2015.04.001.
19. Albers MJ, Bok R, Chen AP, Cunningham CH, Zierhut ML, Zhang VY, Kohler SJ, Tropp J, Hurd RE, Yen Y-F, Nelson SJ, Vigneron DB, Kurhanewicz J.



- Hyperpolarized  $^{13}\text{C}$  lactate, pyruvate, and alanine: noninvasive biomarkers for prostate cancer detection and grading. *Cancer Research* 2008;68:8607–8615.
20. Kurhanewicz J, Vigneron DB, Brindle K, Chekmenev EY, Comment A, Cunningham CH, DeBerardinis RJ, Green GG, Leach MO, Rajan SS, Rizi RR, Ross BD, Warren WS, Malloy CR. Analysis of cancer metabolism by imaging hyperpolarized nuclei: prospects for translation to clinical research. *Neoplasia* 2011;13:81–97.
  21. Nelson SJ, Kurhanewicz J, Vigneron DB, Larson PEZ, Harzstark AL, Ferrone M, Van Criekinge M, Chang JW, Bok R, Park I, Reed G, Carvajal L, Small EJ, Munster P, Weinberg VK, Ardenkjaer-Larsen JH, Chen AP, Hurd RE, Odegardstuen L-I, Robb FJ, Tropp J, Murray JA. Metabolic Imaging of Patients with Prostate Cancer Using Hyperpolarized  $[1-^{13}\text{C}]$ Pyruvate. *Sci Transl Med* 2013;5:198ra108.
  22. Thong AE, Zhao H, Ingels A, Valta MP, Nolley R, Santos J, Young SR, Peehl DM. Tissue slice grafts of human renal cell carcinoma: an authentic preclinical model with high engraftment rate and metastatic potential. *Urol Oncol* 2014;32:43.e23–30.
  23. Maund SL, Nolley R, Peehl DM. Optimization and comprehensive characterization of a faithful tissue culture model of the benign and malignant human prostate. *Lab Invest* 2013;94:208–221.
  24. Keshari KR, Sriram R, Van Criekinge M, Wilson DM, Wang ZJ, Vigneron DB, Peehl DM, Kurhanewicz J. Metabolic reprogramming and validation of hyperpolarized  $^{13}\text{C}$  lactate as a prostate cancer biomarker using a human prostate tissue slice culture bioreactor. *Prostate* 2013;73:1171–1181.
  25. Keshari KR, Wilson DM, Van Criekinge M, Sriram R, Koelsch BL, Wang ZJ, VanBrocklin HF, Peehl DM, O'Brien T, Sampath D, Carano RAD, Kurhanewicz J. Metabolic response of prostate cancer to nicotinamide phosphoribosyltransferase inhibition in a hyperpolarized MR/PET compatible bioreactor. *Prostate* 2015;doi:10.1002/pros.23036.
  26. Albers MJ, Butler TN, Rahwa I, Bao N, Keshari KR, Swanson MG, Kurhanewicz J. Evaluation of the ERETIC method as an improved quantitative reference for  $^1\text{H}$  HR-MAS spectroscopy of prostate tissue. *Magn Reson Med* 2009;61:525–532.
  27. Keshari KR, Sriram R, Koelsch BL, Van Criekinge M, Wilson DM, Kurhanewicz J, Wang ZJ. Hyperpolarized  $^{13}\text{C}$ -pyruvate magnetic resonance reveals rapid lactate export in metastatic renal cell carcinomas. *Cancer Research* 2013;73:529–538.
  28. Ross B, Freeman D, Chan L. Contributions of nuclear magnetic resonance to renal biochemistry. *Kidney Int* 1986;29:131–141.

## Acknowledgements

We thank Rosalie Nolley, Romelyn Delos Santos, Laura Tabatabai, Ailin Hansen, Dave Korenchen, Sukumar Subramaniam, Bertram Koelsch and Jessie Lee for assistance in performing experiments.

qRT-PCR analysis was conducted at the Genome Analysis Core Facility, Helen Diller Family Comprehensive Cancer Center, University of California, San Francisco

## Figures

**Figure 1.** Bioenergetics of renal tissue slices. A)  $^{31}\text{P}$  spectrum of grade 2 ccRCC. The inset shows the temporal  $\beta\text{NTP}$  concentration of ccRCC tissue slices continuously perfused in the bioreactor for over 24 hours. B) Bar graph of the varying levels of phospholipids in renal tissue slices. (white bars = normal renal tissue, gray bars= benign renal tumors, and black bars=ccRCCs)

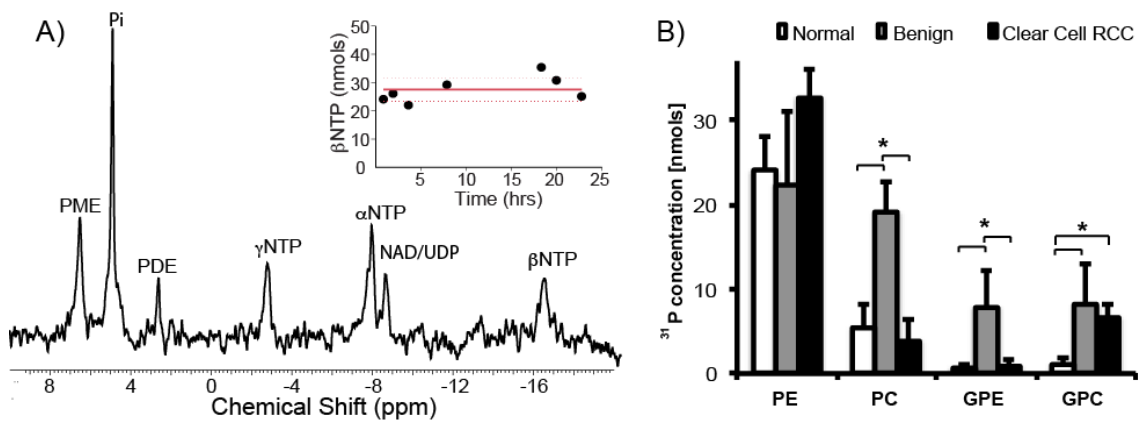


**Figure 2.** Hyperpolarized  $[1-^{13}\text{C}]$ Pyruvate metabolism of renal tissue slices. A) Representative hyperpolarized  $^{13}\text{C}$  spectrum of grade 2 ccRCC tissue slices. Inset shows the lactate kinetics over 5 minutes. B) Bar graphs of normalized hyperpolarized  $[1-^{13}\text{C}]$  alanine and  $[1-^{13}\text{C}]$  lactate in the renal tissue slices. (white bars = normal renal tissue, gray bars= benign renal tumors and black bars=ccRCC)

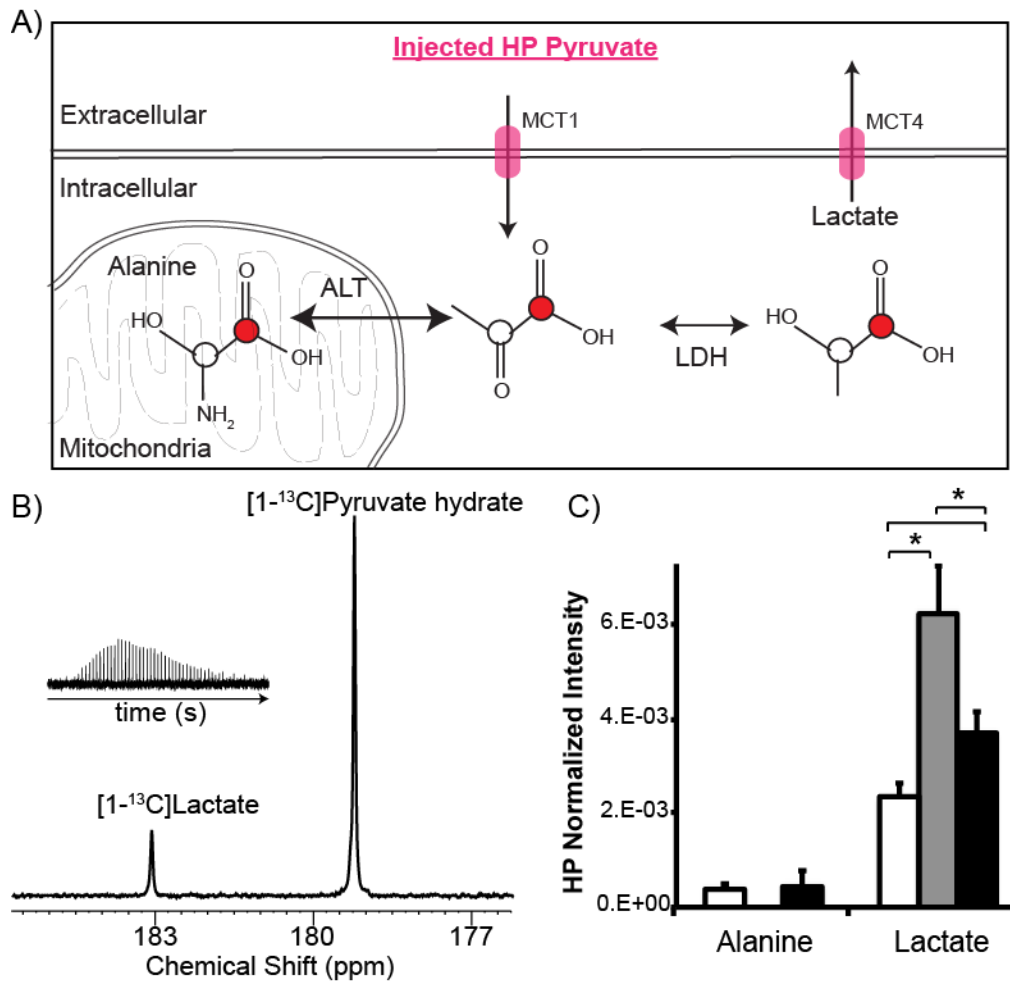


**Figure 3.** LDH activity and expression A) LDH-A expression of renal tissue slices. B) LDH activity of renal tissue slices. (white bars = normal renal tissue, gray bars= benign renal tumors and black bars=ccRCC)

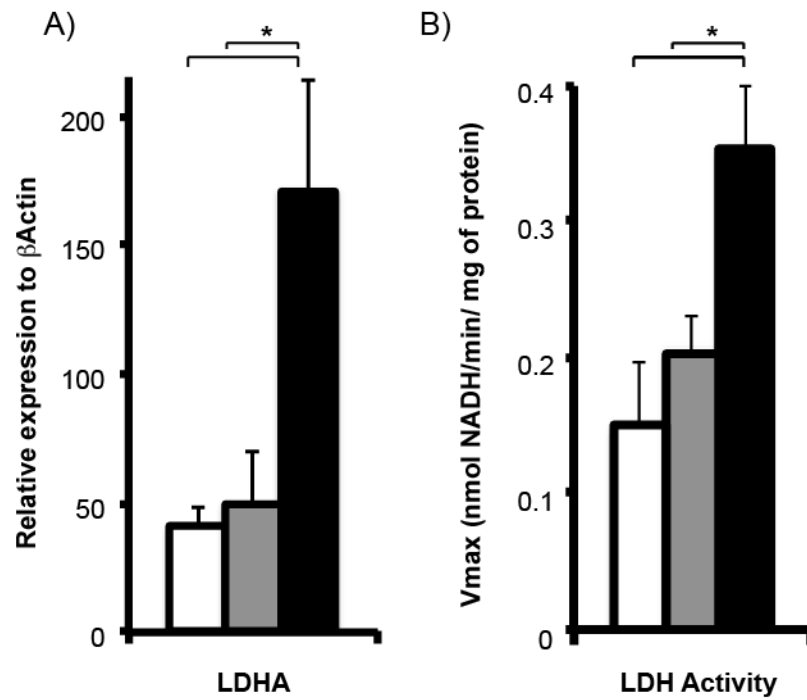


**Figure 4.** Renal tissue MCT4 expression and lactate efflux. A) Immunohistochemical staining of MCT4 and B) mRNA expression of MCT4 in renal tissue slices. C) Rate of lactate efflux from renal tissue slices. (white bars = normal renal tissue, gray bars=

benign renal tumors and black bars=ccRCC)

